



universität
wien

DISSERTATION

Titel der Dissertation

Development of methods for isobar suppression in AMS and
measurements of ^{36}Cl with the VERA 3-MV-tandem accelerator

Verfasser

Mag. rer. nat. Martin Martschini

angestrebter akademischer Grad

Doktor der Naturwissenschaften (Dr. rer. nat.)

Wien, 2012

Studienkennzahl lt. Studienblatt:

A-091-411

Dissertationsgebiet lt. Studienblatt:

Physik

Betreuer:

Univ.-Prof. Dipl. Ing. Dr. Robin Golser

Abstract

Accelerator mass spectrometry (AMS) of ^{36}Cl ($t_{1/2} = 0.30 \text{ Ma}$) at natural isotopic concentrations requires high particle energies for the separation from the stable isobar ^{36}S and up to now was considered the exclusive domain of tandem-accelerators with at least 5 MV terminal voltage. With this work we demonstrated that the separation of ^{36}Cl and ^{36}S is feasible at particle energies of 24 MeV, which are also accessible for medium-sized facilities with 3 MV terminal voltage like VERA (Vienna Environmental Research Accelerator).

Progress in the technology of ionization chambers and detailed understanding of the relevant ion-atom collision processes made this achievement possible. Within the framework of this thesis, the limitations of isobar suppression in an ionization chamber were closely studied. Comparison of experimental energy loss data with simulations and published data revealed how physics favors isobar separation even at energies below the maximum of the Bragg curve. The strong energy focusing effect at high energy losses significantly reduces energy straggling, hence isobar separation steadily increases up to almost full energy loss. To further optimize the ^{36}S suppression, energy loss, energy straggling and angular scattering in various counter gases were investigated theoretically and experimentally. With $\text{C}_4\text{H}_{10} + \text{Ar}$ in an optimized detection setup consisting of a split-anode ionization chamber and a silicon strip detector, ^{36}S suppression factors $> 2 \times 10^4$ have been achieved.

The sulfur content of the ion beam was significantly reduced by assessing the influence of sample size, cathode design, backing material and ion source operating conditions. Due to advances in measurement procedure and data evaluation, the reproducibility for high ratio samples ($^{36}\text{Cl}/\text{Cl} > 10^{-12}$) is better than 2 %. The injector to detector efficiency of 8 % for ^{36}Cl also compares favorable to other facilities. Following an in-depth investigation of the cross contamination and the memory effect of our ion source, the blank value is $^{36}\text{Cl}/\text{Cl} < 10^{-15}$, which is in good agreement with the lowest so far published isotope ratios. The first successful AMS measurement of ^{36}Cl exposure dating samples at 3 MV terminal voltage further demonstrates that ^{36}Cl measurements at VERA are now competitive to other labs.

During investigations of additional techniques for isobar separation in a cesium sputter ion source, we discovered that continuous wave laser light induces a significant change in negative ion production from a silver chloride target. Approximately 100 mW of laser light reduced the sulfur to chlorine ratio by one order of magnitude. Experiments were first performed at the ion beam facility GUNILLA (University of Gothenburg) with macroscopic amounts of sulfur and later reproduced at VERA with chemically cleaned AgCl targets. While the physical explanation behind the effect is still unclear, the technique was successfully applied during a regular AMS measurement of ^{36}Cl and further enhances the abundance sensitivity.

Zusammenfassung

Der Nachweis von ^{36}Cl in natürlichen Häufigkeiten mittels Beschleunigermassenspektrometrie (AMS) erfordert hohe Teilchenenergien für die Unterdrückung des stabilen Isobars ^{36}S und konnte bisher nur an Beschleunigeranlagen mit mindestens 5 MV Terminalspeisung durchgeführt werden. Im Rahmen dieser Arbeit konnten wir zeigen, dass ^{36}Cl und ^{36}S bereits bei Energien von 24 MeV, welche auch an mittelgroßen Beschleunigern mit 3 MV Terminalspeisung wie VERA (Vienna Environmental Research Accelerator) zur Verfügung stehen, getrennt werden können.

Diese Entwicklung wurde erst durch technische Fortschritte bei Ionisationskammern und einem genauen Verständnis der relevanten Ionen-Atom-Stoßprozesse möglich. Der Vergleich experimenteller Daten über den Energieverlust in Ionisationskammern mit Simulation und publizierten Werten lieferte wichtige Erkenntnisse über die Physik der Isobarentrennung, insbesondere bei Energien unterhalb des Bragg-Maximums. Der Effekt der Energiefokussierung bei großen Energieverlusten führt zu einer starken Abnahme der Energie-Unschärfe und somit zu einem Anstieg der Isobarentrennung bis zu beinahe vollem Energieverlust. Die experimentelle Bestimmung der relevanten Eigenschaften von mehreren Detektorgasen brachte eine deutliche Verbesserung des Trennvermögens. Mit $\text{C}_4\text{H}_{10} + \text{Ar}$ als Zählgas und einem optimierten Detektoraufbau bestehend aus einer Ionisationskammer mit geteilter Anode und einem Silizium-Streifendetektor wurden schließlich ^{36}S Unterdrückungsfaktoren $> 2 \times 10^4$ gemessen.

Detaillierte Untersuchungen des Einflusses von Probengröße, Kathoden-Design, Träger-Material sowie der Ionenquellen-Betriebsparameter führten zu einer signifikanten Reduktion des Schwefelanteils im Ionenstrahl. Aufgrund zahlreicher Verbesserungen im Messablauf und der folgenden Datenauswertung ist die Reproduzierbarkeit für Proben mit einem $^{36}\text{Cl}/\text{Cl}$ Verhältnis $> 10^{-12}$ besser als 2 %. Die Injektor-Detektor Effizienz ist mit 8 % ebenfalls konkurrenzfähig zu größeren Anlagen. Dank einer systematischen Bestimmung des zeitlichen Übersprechens der Ionenquelle und der Cross-Kontamination ist der Messuntergrund $^{36}\text{Cl}/\text{Cl} < 10^{-15}$ und somit in guter Übereinstimmung mit den niedrigsten bisher publizierten Isotopenverhältnissen. Die Resultate der ersten AMS Messung von natürlich ^{36}Cl Expositionsdatierungs-Proben bei 24 MeV untermauern die Wettbewerbsfähigkeit der ^{36}Cl Messungen bei VERA im Vergleich zu anderen Labors.

Experimente mit neuen Techniken für zusätzliche Isobarenunterdrückung führten zur Entdeckung des starken Einflusses von kontinuierlichem Laserlicht auf die Produktion negativer Ionen von einer AgCl-Probe in einer Cäsium Sputterionenquelle. Ungefähr 100 mW Laserlicht reduzierten das Schwefel-zu-Chlor-Verhältnis um bis zu eine Größenordnung. Dieser neuartige Effekt, dessen physikalische Erklärung noch immer offen ist, wurde in Experimenten an GUNILLA (Universität Göteborg) und an VERA untersucht und schließlich erfolgreich in einer AMS-Messung angewandt.

Contents

| | | |
|----------|--|-----------|
| 1 | Outline of this work | 1 |
| 2 | Introduction | 3 |
| 2.1 | AMS and the radionuclide ^{36}Cl | 3 |
| 2.2 | Techniques for isobar separation in AMS | 5 |
| 2.2.1 | Isobar suppression in the ion source and the accelerator | 5 |
| 2.2.2 | Atomic isobar suppression in the analyzer and the detector | 6 |
| 2.2.3 | New techniques for atomic isobar suppression | 9 |
| 2.3 | The VERA facility | 10 |
| 2.4 | Previous results from AMS of ^{36}Cl at VERA | 12 |
| 3 | Sulfur suppression with the $\Delta E/E$ detection setup | 15 |
| 3.1 | The ΔE -E detection setup | 15 |
| 3.1.1 | The ionization chamber | 16 |
| 3.1.2 | The silicon strip detector | 16 |
| 3.2 | Introduction to energy loss of ions in matter | 18 |
| 3.2.1 | Energy loss and stopping power | 18 |
| 3.2.2 | Energy loss straggling | 21 |
| 3.3 | Isobar separation with the ΔE -E detection setup | 22 |
| 3.3.1 | The energy loss signal from an ionization chamber | 23 |
| 3.3.2 | Detector resolution | 26 |
| 3.3.3 | Isobar separation below the Bragg maximum | 30 |
| 3.3.4 | Sulfur suppression | 32 |
| 3.3.5 | Enhanced suppression with the silicon strip detector | 35 |
| 3.3.6 | Comparison with simulations | 37 |
| 3.4 | Comparison of detector gases | 40 |
| 3.4.1 | Energy calibration | 40 |
| 3.4.2 | Measurement of peak widths in various detector gases | 43 |
| 3.4.3 | Energy loss spectra and sulfur suppression factors | 45 |
| 3.5 | Additional signals from the detection setup | 49 |
| 3.5.1 | Pulse-width measurement for pile-up rejection | 49 |
| 3.5.2 | The residual energy signal from the silicon strip detector | 52 |
| 3.5.3 | The position information from the silicon strip detector | 54 |

| | | |
|----------|--|-----------|
| 4 | The ion source and sulfur output from the sample | 57 |
| 4.1 | Reduction of sulfur output from the sample | 57 |
| 4.1.1 | Sample preparation and handling | 57 |
| 4.1.2 | Target wheel, cathode design and backing material | 59 |
| 4.1.3 | Sample size and sulfur contamination | 62 |
| 4.2 | The SNICS ion source and sulfur output | 63 |
| 4.2.1 | The ion source regulation | 64 |
| 4.2.2 | Operation parameters and sulfur output | 65 |
| 5 | Measurement procedure | 69 |
| 5.1 | Tuning the machine | 69 |
| 5.2 | Measurement and data acquisition | 71 |
| 5.3 | Reference materials | 73 |
| 5.4 | Data evaluation | 74 |
| 5.4.1 | Defining the ^{36}Cl region of interest | 75 |
| 5.4.2 | The peak drift correction | 77 |
| 5.4.3 | Turnwise evaluation and applied corrections | 77 |
| 6 | Performance and results | 81 |
| 6.1 | Efficiency | 81 |
| 6.2 | Precision and accuracy | 82 |
| 6.2.1 | Precision and reproducibility | 82 |
| 6.2.2 | The ^{36}Cl round robin | 84 |
| 6.2.3 | Cross calibration via the $^{35}\text{Cl}(n,\gamma)^{36}\text{Cl}$ cross section | 86 |
| 6.3 | Background | 86 |
| 6.3.1 | Cross contamination and memory effect of the ion source | 87 |
| 6.4 | Comparison with other labs | 90 |
| 6.5 | Measurement of exposure dating samples | 91 |
| 6.5.1 | The Lonar crater samples | 91 |
| 6.5.2 | Samples from the Anatolian Plateau | 92 |
| 7 | A novel technique for sulfur suppression | 95 |
| 7.1 | Motivation and first experiments | 95 |
| 7.2 | Experimental setup | 96 |
| 7.3 | Results with macroscopic amounts of sulfur at GUNILLA | 98 |
| 7.3.1 | Response of the ion current to laser light | 98 |
| 7.3.2 | Power and wavelength dependence of the effect | 100 |
| 7.4 | Results with microscopic amounts of sulfur at VERA | 101 |
| 7.4.1 | General features of the effect | 101 |
| 7.4.2 | Systematic studies | 103 |
| 7.4.3 | Application of the laser in an AMS measurement | 105 |
| 7.5 | Discussion of results and the physics behind the effect | 106 |

| | |
|---------------------------------|------------|
| 8 Discussion and outlook | 109 |
| Bibliography | 111 |
| Acknowledgments | 123 |
| Curriculum vitae | 125 |

List of Tables

| | | |
|-----|---|----|
| 3.1 | Energy straggling in SiN according to SRIM | 26 |
| 3.2 | Sulfur suppression factors for different particle energies | 34 |
| 3.3 | Sulfur suppression factors for different ^{36}Cl detector efficiencies | 35 |
| 3.4 | SRIM energy losses in the detector windows | 41 |
| 3.5 | Energy calibration of the detection setup | 42 |
| 3.6 | Detector transmission and energy loss at optimal gas pressure | 48 |
| 3.7 | Contribution of detector signals to the sulfur suppression | 53 |
| 4.1 | Sulfur output from various backing materials | 60 |
| 4.2 | Sulfur output as a function of sample size | 62 |
| 5.1 | Measurement cycle for ^{36}Cl at VERA | 71 |
| 5.2 | Inhouse standards from a dilution series | 74 |
| 6.1 | Detection efficiency for ^{36}Cl | 81 |
| 6.2 | Cross calibration of reference materials | 86 |
| 6.3 | Cross contamination and memory effect of the ion source | 87 |
| 6.4 | Performance data at VERA and various other AMS facilities | 90 |
| 6.5 | AMS results for the Lonar crater exposure dating samples | 92 |
| 6.6 | AMS results for the Anatolian Plateau exposure dating samples . . . | 93 |

List of Figures

| | | |
|------|--|----|
| 2.1 | Energies of ^{36}Cl available with different terminal voltages | 8 |
| 2.2 | The VERA AMS facility | 11 |
| 3.1 | The detection setup | 15 |
| 3.2 | The ionization chamber | 17 |
| 3.3 | The silicon strip detector | 18 |
| 3.4 | Stopping power of sulfur in isobutane | 19 |
| 3.5 | Working principle of an ionization chamber | 23 |
| 3.6 | Isobar separation in an ionization chamber | 25 |
| 3.7 | Energy straggling of S and Cl in SiN | 27 |
| 3.8 | Energy loss and isobar separation in isobutane | 31 |
| 3.9 | Total energy loss spectra and sulfur suppression | 33 |
| 3.10 | Suppression of tails in the energy loss spectra | 36 |
| 3.11 | Sulfur suppression factors with the upgraded detection setup | 37 |
| 3.12 | Energy loss and straggling - experimental and theoretical values | 38 |
| 3.13 | SRIM simulation of the suppression of scattering tails | 39 |
| 3.14 | Energy loss peak positions for energy calibration | 42 |
| 3.15 | Peak widths in various detector gases | 44 |
| 3.16 | Study on energy straggling in argon-methane | 45 |
| 3.17 | Distance and separation of ^{36}Cl and ^{36}S peaks in various gases | 46 |
| 3.18 | Energy loss spectra in argon-methane and isobutane | 47 |
| 3.19 | Sulfur suppression factors with different detector gases | 48 |
| 3.20 | Illustration of ^{36}S pile-up mimicking a ^{36}Cl event | 50 |
| 3.21 | Spectrum showing pulse width vs. total energy loss | 50 |
| 3.22 | Contribution of the pulse width signal to the suppression of tails | 51 |
| 3.23 | Residual energy spectra from the silicon strip detector | 53 |
| 3.24 | Plot of the position information from the strip detector | 54 |
| 3.25 | Correlation of y-positions of ions in both detectors | 55 |
| 4.1 | Punch heads used for sample pressing | 59 |
| 4.2 | Photos of the new sample wheel | 60 |
| 4.3 | Sample holders and scan of the sulfur output over the wheel | 61 |
| 4.4 | Stability of source output with the regulation | 65 |
| 4.5 | Evolution of sulfur output over time | 66 |
| 4.6 | Variation of sulfur output with ionizer power | 68 |

| | | |
|-----|---|-----|
| 5.1 | Components of VERA used for tuning and measurement of ^{36}Cl . . . | 69 |
| 5.2 | Data acquisition electronics | 72 |
| 5.3 | Sample spectra and the ^{36}Cl region of interest | 76 |
| 5.4 | Effect of the peak drift correction | 78 |
| 6.1 | Reproducibility of ^{36}Cl results for various $^{36}\text{Cl}/\text{Cl}$ ratios | 83 |
| 6.2 | Longterm stability of ^{36}Cl results | 84 |
| 6.3 | Results from a laboratory intercomparison | 85 |
| 6.4 | Study of the source memory effect with the $^{35}\text{Cl}/^{37}\text{Cl}$ ratio | 88 |
| 7.1 | Schematic of the optical setup at GUNILLA and VERA. | 97 |
| 7.2 | Mass spectra with and without laser light | 98 |
| 7.3 | Mass spectra of Cl and S with and without laser light | 99 |
| 7.4 | Laser power dependence of the effect | 100 |
| 7.5 | Response of the ion currents to IR-laser light | 101 |
| 7.6 | Effect of the laser on a small AgCl target at VERA | 102 |
| 7.7 | Longterm behavior of the $^{36}\text{S}/^{35}\text{Cl}$ ratio and the Cl-current | 103 |
| 7.8 | Systematic study of the response to laser light | 104 |
| 7.9 | AMS results with light-induced sulfur suppression | 105 |

1 Outline of this work

Before starting with the detailed description of the advances that now allow AMS measurements of ^{36}Cl at 3 MV terminal voltage, I want to give a short outline of this work:

Chapter 2: Introduction shall give an introduction to this work and explain the principal tasks and challenges involved in AMS of ^{36}Cl and in the suppression of isobars. It also includes a summary of previous work on measurement of ^{36}Cl at the Vienna Environmental Research Accelerator (VERA) and a brief description of the facility.

Chapter 3: Sulfur suppression with the $\Delta E/E$ detection setup deals with the central issue of ^{36}S suppression in the dedicated detection setup. After a summary of the physical processes, which limit isobar separation in ionization chambers, the results from our theoretical and experimental investigations of the detection setup are presented. They include a study of the relevant properties of various counter gases and a detailed analysis of the contribution of different detector signals to the total sulfur suppression.

Chapter 4: The ion source and sulfur output from the sample describes our efforts to reduce the sulfur output from the ion source and to produce a stable chlorine beam. This task required optimization of every step from sample preparation to ion source regulation, including a new sample holder design and a survey of the sulfur content of various backing materials. Also limitations in the reduction of sample size were investigated.

Chapter 5: Measurement procedure contains a detailed account of the tuning procedure, the machine setup and the data acquisition. All relevant facts for the actual AMS measurement and data evaluation are listed.

Chapter 6: Results and performance gives an overview about the precision and accuracy of ^{36}Cl measurements at VERA. Background levels and the memory effect of the ion source are discussed and compared to results from other labs. Additionally, the results from the first measurements of ^{36}Cl exposure dating samples at 3 MV terminal voltage are presented.

Chapter 7: A novel technique for sulfur suppression presents our experimental results on the newly discovered suppression of sulfur, induced by cw laser light in a cesium sputter ion source. This novel technique can be implemented with moderate

effort and provides additional sulfur suppression of up to one order of magnitude. It was successfully applied at two facilities and proved useful in an AMS measurement. The general features of the effect are described, the physical explanation however still remains unclear.

Chapter 8: Discussion and outlook summarizes the achievements and gives a short outlook on future plans based on the results of this work.

Parts of this thesis are already published in three peer-reviewed articles. The work described in these articles was performed in a collaborative way, where M. Martschini had the leading role and did large parts of the work as expressed by first authorship:

- M. Martschini, O. Forstner, R. Golser, W. Kutschera, S. Pavetich, A. Priller, P. Steier, M. Suter, A. Wallner, Recent advances in AMS of ^{36}Cl with a 3-MV-tandem, Nuclear Instruments and Methods in Physics Research B 269 (2011) 3188–3191.
- M. Martschini, P. Andersson, O. Forstner, R. Golser, D. Hanstorp, A.O. Lindahl, W. Kutschera, S. Pavetich, A. Priller, J. Rohlén, P. Steier, M. Suter, A. Wallner, AMS of ^{36}Cl with the VERA 3 MV tandem accelerator, Nuclear Instruments and Methods in Physics Research B (2012), doi:10.1016/j.nimb.2012.01.055.
- M. Martschini, J. Rohlén, P. Andersson, R. Golser, D. Hanstorp, A.O. Lindahl, A. Priller, P. Steier, O. Forstner, Light-induced suppression of sulfur in a cesium sputter ion source, International Journal of Mass Spectrometry (2012), doi:10.1016/j.ijms.2012.02.023.

Vienna, 30.03.2012

Univ.-Prof. Dipl. Ing. Dr. Robin Golser

2 Introduction

2.1 AMS and the radionuclide ^{36}Cl

Accelerator mass spectrometry (AMS) is used since more than 30 years for the detection of long-lived radioisotopes in numerous applications ranging from astrophysics and archeology to earth sciences and medicine [1–4]. With typically low natural abundances around $10^{-12} - 10^{-18}$ g/g and half lives of $10^4 - 10^8$ a, many of the isotopes of interest are inaccessible with other techniques, e.g. decay counting or conventional mass spectrometric methods. While decay counting would require exorbitantly large amounts of sample material due to the low decay rate, mass spectrometric methods like inductively coupled plasma MS, thermal ionization MS or secondary ionization MS suffer from low efficiency and the interference of other species, which are usually several orders of magnitude more abundant.

In principle, the sensitivity of accelerator mass spectrometry for a rare nuclide is also limited by the ability to distinguish it from abundant neighboring isotopes and from isobaric interferences, but at much higher level. The use of a series of filters allows identification of rare isotopes in the presence of $10^{12} - 10^{16}$ times more abundant species of neighboring masses. In typical AMS facilities, the following components act as filters: the negative ion source, the low energy mass spectrometer, the accelerator, the high energy mass spectrometer and the final detection setup. Different from conventional mass spectrometry, molecular isobars, i.e. molecules with almost the same mass as the ion of interest, can be effectively removed in AMS by their break-up in the stripping process of a tandem accelerator. Consequently, only atomic neighboring masses with a ΔM of at least 1 amu have to be separated in the magnetic spectrometers and a mass resolution of $M/\Delta M \approx 500$ is sufficient even for heavier isotopes. This permits a high beam transmission, which is a general feature of AMS systems and required for successful detection of a very limited number of rare atoms per sample.

Separation of atomic isobars, i.e. atoms with almost the same mass but from a nearby element, is more difficult because they pass magnetic filters together with the isotope of interest. Additional techniques, which are discussed in section 2.2, have to be applied for their separation. Since established techniques so far require particle energies around 1 MeV/amu, only facilities with 5 MV terminal voltage or beyond could perform measurements of ^{36}Cl and heavier isotopes with isobaric interferences. In fortunate cases like ^{14}C , ^{26}Al or ^{129}I , the stable atomic isobars do not form negative

ions and are already suppressed in the negative ion source. The lack of atomic isobars in these ion beams has allowed a lowering of the terminal voltage into the 200 kV range instead of several MV. Recently, this facilitated a reduction in the size of dedicated ^{14}C AMS systems to table-top dimensions [5]. While AMS has evolved at nuclear physics facilities with large accelerators and many measurements were first performed at high particle energies, medium-sized tandem-accelerators like VERA (see section 2.3) are capable of measuring all AMS isotopes where no atomic isobars interfere [6]. In many cases, their performance regarding efficiency, precision, usability and costs is even superior. For this reason, significant effort is put into extending the measurement capabilities of small and medium-sized AMS facilities to isotopes, which could previously only be detected at facilities with large accelerators. A good overview of the physical challenges involved in the development of universal low-energy AMS systems is given in [7].

One isotope of utter interest, which has been exclusively the domain of large accelerators with at least 5 MV terminal voltage, is the radioisotope ^{36}Cl with a half life of $(3.01 \pm 0.03) \times 10^5$ a [8]. Being a cosmogenic radionuclide, ^{36}Cl is mainly used in hydrology and exposure age dating of rocks [3]. In the atmosphere, ^{36}Cl is produced via spallation of ^{40}Ar by cosmic ray particles, a detailed account is given in [9]. Its hydrophilic behavior makes it a perfect tracer for groundwater studies and atmospheric transport investigations. In recent years, the demand from environmental and geosciences for measurements of in situ produced ^{36}Cl in rock samples has increased significantly and several new AMS facilities have been explicitly designed to allow measurements of ^{36}Cl [10–13].

Theory and applications of terrestrial in situ cosmogenic nuclides have been extensively discussed by Gosse and Phillips [14]. Advantages of ^{36}Cl over other cosmogenic nuclides like ^{10}Be and ^{26}Al are its high production rates in several rock materials like K-feldspar, plagioclase or calcite and easy removability of atmospheric background. The main production pathway for ^{36}Cl in these rock materials is spallation of calcium and potassium, generally minor contributions come from thermal neutron activation of ^{35}Cl and negative muon capture of ^{40}Ca and ^{39}K . Important for applications is the fact that ^{36}Cl background from meteoric components can be easily separated by first crushing and leaching the sample, which allows whole rock chemistry and no prior separation of minerals is required. In the case of carbonate rocks, chemical separation of atmospheric background from ^{10}Be is at least very delicate or even impossible [15]. Of course, also dating with ^{36}Cl is not straightforward and many influences have to be considered. Uncertainties in the contribution of various production pathways complicate the calculation of the total production rate. Additionally, possible changes in shielding of the target material or variations in the cosmic ray flux have to be assessed. A small background of ^{36}Cl stems from other sources such as activation of ^{35}Cl by nucleogenic neutrons. Loss of in situ produced nuclides by erosion and weathering processes also needs to be accounted for. In order to disentangle all these effects and correct for their contributions in the calculation of exposure ages,

a multielemental approach involving several nuclides is desirable (see e.g. [16]), not only in ^{36}Cl -dating but also for other exposure dating isotopes.

Mass spectrometric identification of ^{36}Cl is hindered by the existence of two stable atomic isobars. While ^{36}Ar being a noble gas is completely suppressed in a negative ion source, ^{36}S , which has a natural isotopic abundance of 0.013–0.019% [17], does form negative ions. Chemical reduction of sulfur is only possible down to a level of ~ 0.1 –1 ppm, then further cleaning steps introduce as much contamination as they remove. For chlorine samples, this corresponds to an isotopic ratio $^{36}\text{S}/^{35}\text{Cl}$ of around 10^{-11} – 10^{-10} . In contrast, $^{36}\text{Cl}/^{35}\text{Cl}$ ratios of natural samples range from 10^{-11} to 10^{-15} , thus up to five orders of magnitude lower. While initial $^{36}\text{Cl}/^{35}\text{Cl}$ ratios in rocks may be quite high, the production of an AMS target requires a certain amount of chlorine and thus generally ~ 1 mg of stable chlorine have to be added as carrier during sample preparation. With typically 10^6 – 10^8 atoms ^{36}Cl extracted from the samples, this minimum amount of carrier results in the above $^{36}\text{Cl}/^{35}\text{Cl}$ ratios for the final AMS sample. Since ^{36}S passes all magnetic and electrostatic filters of an AMS facility together with ^{36}Cl , determination of ^{36}Cl requires additional techniques, which provide a suppression of ^{36}S against ^{36}Cl by at least a factor of 10 000. An overview of possible isobar separation techniques applied in AMS is given in the next section.

2.2 Techniques for isobar separation in AMS

Up to mass 209, there exists at least one stable isotope at each mass with the exception of masses 5 and 8. Additionally, there are several abundant isotopes like ^{238}U at even higher masses. Therefore, mass spectrometric measurements of rare radionuclides at natural abundances in most cases require suppression of at least one atomic isobar in addition to the high molecular background. Exceptions are ^{236}U or the plutonium isotopes, where no abundant atomic isobars exists. The intention of this section is to give an overview over current techniques and their potential for AMS of ^{36}Cl .

2.2.1 Isobar suppression in the ion source and the accelerator

The first filter for isobar separation in AMS systems is the negative ion source, where all elements, which do not form negative ions, are already suppressed. Examples are nitrogen, magnesium and several noble gases like argon, krypton and xenon. Unfortunately, this is only sufficient for the measurement of a small number of isotopes including ^{14}C , ^{26}Al and ^{129}I . In some cases, the choice of a suitable molecule for the extraction of the wanted species from the source allows a substantial reduction of the interfering isobar. The use of BeF^- for measurements of ^{10}Be reduces the interference from the isobar ^{10}B by 5 orders of magnitude compared to BeO^- [18].

Another prominent example is the almost complete suppression of ^{41}K against ^{41}Ca when extracting CaH_3^- [19], good results have also been achieved with CaF_3^- [20]. Fluorides are generally good candidates for such endeavors, an extensive study is presented in [21]. In the case of ^{36}Cl , no similar possibilities for the suppression of ^{36}S have been discovered so far.

After mass selection in the low energy mass spectrometer, the stripper in the accelerator terminal constitutes the dominant filter for the removal of background from molecular isobars. This background is eventually up to 10 orders of magnitude more abundant than the isotope of interest. Following acceleration to the terminal, the molecules are broken up into their atomic constituents. Traditionally this is achieved by stripping to charge states where the respective molecules are no longer stable (usually $\geq 3+$). In small AMS machines, which use lower charge states, molecules are effectively destroyed by collisional break-up reactions with the stripper gas [22]. Generally, the fragments from molecular background can then easily be separated from the isotopes of interest in the high energy mass spectrometer. An important exception are fragments, which have the same m/q after stripping as the ions of interest, because they will follow the beam through the high energy spectrometer [23, 24]. While a discrimination from ions of the wanted mass can in principle be achieved by any energy sensitive detector, the high count rate of fragments generally makes a measurement unfeasible. The choice of the charge state after stripping is therefore restricted to values avoiding m/q ambiguities with lighter masses. For example, measurement of ^{36}Cl in the $6+$ charge state is impossible due to the strong interference of $^{12}\text{C}^{2+}$ injected as C_3 . Selection of the $5+$ or $7+$ charge state of ^{36}Cl after the stripper eliminates this problem.

2.2.2 Atomic isobar suppression in the analyzer and the detector

Since atomic isobars have the same mass, charge and energy as the rare isotope, they can not be identified with magnetic and electrostatic filters, time-of-flight systems or a total energy measurement. Consequently, special techniques have to be applied for the separation of atomic isobars in the ion beam. It is this final filter step where kinetic energy is the key parameter that determines the degree of isobar suppression and currently limits the sensitivity of small accelerator systems for the respective isotopes. Two new approaches, which try to get around this problem, are discussed in the next section.

All of the techniques presented in this section make use of the difference in atomic charge between the isobars. The most direct approach is full stripping of the ions, which can be applied if the interfering isobars have a lower atomic number than the ions of interest. After acceleration and passage through a stripping foil, the fully stripped ions of the radionuclide (charge state $Z+$) are selected. Thereby, isobars with lower atomic number are completely suppressed because they can not adopt this charge state. This method works for the separation of ^{36}Cl and ^{36}S , but energies

around 150 MeV are required to efficiently populate the charge state 17+ [25]. Separation of heavier isobars like ^{81}Kr and ^{81}Br only works at energies of ~ 1 GeV [26], which are not accessible even with the largest tandem accelerators.

Hence, most techniques for isobar suppression are based on the Z-dependent energy loss in matter, which is in principle accessible at much lower energies. First techniques of this kind have been established already in the early days of AMS (see e.g. [27]). The most common method is to record the difference in energy loss characteristics when the ions pass through matter, e.g., by ΔE measurements in a segmented ionization chamber (see chapter 3). The achievable degree of isobar suppression with this technique strongly increases with the available particle energy and the relative difference in atomic number, as discussed later, but is typically limited to 3–5 orders of magnitude. For ^{36}Cl measurements this is just sufficient if the ^{36}S content of the sample is low.

In case the interfering isobar is much more abundant and subsequently its count rate too high for the detector, a separation prior to the final detection setup is needed and there are different methods to facilitate this. If the isobar has a higher atomic number and subsequently a higher stopping power than the rare isotope, a passive absorber can be placed in front of the detector [28]. While ions from elements with higher Z are stopped within the absorber, ions of the wanted species still have some residual energy left to enter the detector. This method works fine for the suppression of ^{10}B ($Z=5$) against ^{10}Be ($Z=4$), but can not be applied for ^{36}Cl ($Z=17$) and ^{36}S ($Z=16$) since chlorine has a higher Z.

A more universal approach is the use of a degrader foil in combination with an energy sensitive bending element [29, 30]. Passage of the beam through the foil results in a Z-dependent energy loss and isobars are subsequently separated by different deflection in the following bending elements. This degrader foil method is successfully applied for ^{36}Cl measurements at several facilities (e.g. [11]) and reduces the interference from ^{36}S typically by two orders of magnitude. On the other hand, it has the disadvantage of a significantly lower ^{36}Cl detection efficiency due to the restriction to only one out of several charge states after the degrader foil. An alternative technique is the use of a gas-filled magnet [31], where the ions are deflected according to their mean charge state \bar{q} , which is a function of atomic number Z. Recent results for the separation of ^{36}Cl and ^{36}S at 37 MeV with a gas-filled magnet can be found in [32]. It provides suppression factors of ~ 300 but suffers from substantial transmissional losses, resulting in detection efficiencies similar to those of the degrader foil technique.

Unfortunately, usability of all the above methods is strongly dependent on the available particle energy and on the relative difference in atomic number. The growing influence of disturbing effects like angular scattering and energy loss or range straggling deteriorates the resolution towards lower energies and the achievable degree of isobar suppression decreases steeply with energy (cf. table 3.2). Therefore these methods typically require minimum particle energies around 1 MeV/amu, which can not be provided by small accelerators except for the lightest isotopes. After stripping

to the charge state q in the accelerator, the ions of interest and their atomic isobars have the energy

$$E_{HE} = (U_S + U_T) \cdot e \cdot \frac{m_{HE}}{m_{LE}} + U_T \cdot q \cdot e \quad (2.1)$$

where U_S is the total source acceleration voltage, U_T the terminal voltage, m_{HE} and m_{LE} the mass of the ion (atom or molecule) after and prior to stripping and e the elemental charge. Looking at equation 2.1, the final energy can in principle be raised using a higher charge state q . However, the choice of charge state is practically limited to ones with sufficient yield. Since the charge state distribution is itself a function of terminal voltage U_T and higher charge states are populated with increasing U_T , the available energy E_{HE} grows stronger than linear with U_T [6], as illustrated in figure 2.1 for ^{36}Cl and carbon foil stripping.

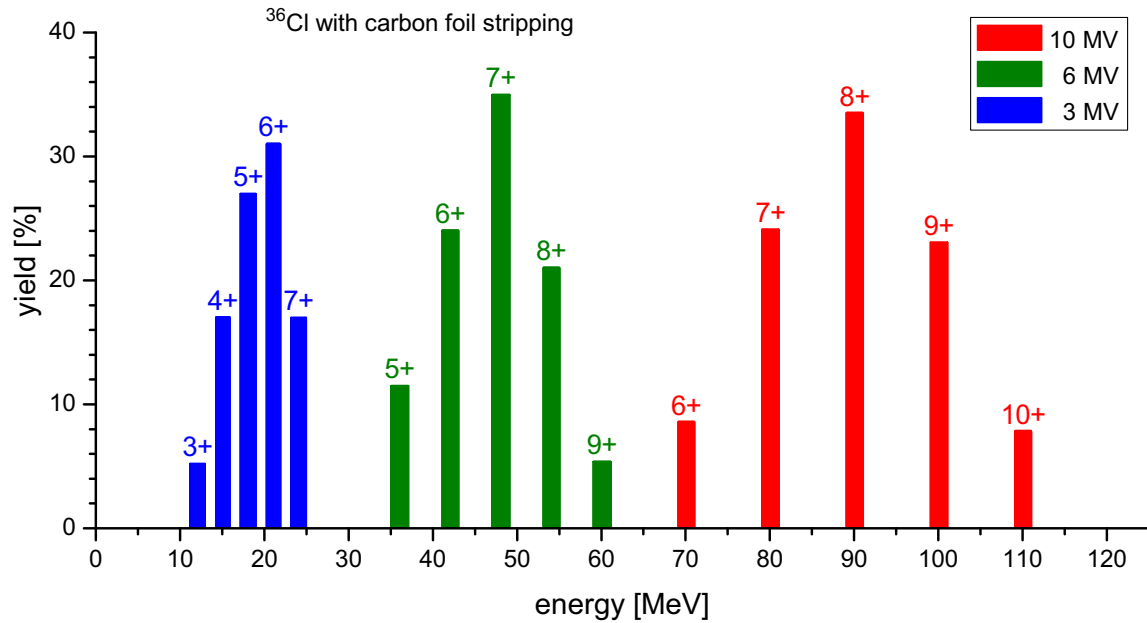


Figure 2.1: Charge state yields with carbon foil stripping and corresponding kinetic energies of ^{36}Cl after acceleration at different terminal voltages. Only charge states with yields $> 5\%$ are plotted. With increasing terminal voltage, higher charge states are populated and the available energy grows stronger than linear with terminal voltage. For AMS of ^{36}Cl , some charge states can not be used for further analysis due to m/q ambiguities with molecular fragments. The charge state distributions were taken from Hofmann et al. [33] and Betz [34].

While ^{10}Be can be well separated from ^{10}B already at 0.75 MeV [35], heavier isobars like ^{53}Mn and ^{53}Cr ($\Delta Z/Z = 1/24$) can be separated only at two of the largest facilities worldwide, which operate at terminal voltages of 14 MV [36, 37]. Technical progress in instrumentation of course pushes this limit towards higher masses and recently

some encouraging results have been achieved for the separation of ^{93}Zr and ^{93}Nb with a passive absorber [38]. Nevertheless, sufficient suppression of isobars down to natural isotopic abundances of rare nuclides still seems out of reach at masses > 120 , especially when the interfering isobar has a lower atomic number.

Of course, technical progress also extends the capabilities of small and medium-sized AMS facilities towards higher masses and new isotopes become available for them. At the beginning of AMS, ^{36}Cl was exclusively accessible at energies of 80 MeV or more [29, 39], but progress in instrumentation has steadily pushed the limit towards lower energies, from 48 MeV to 30 MeV in the last 20 years [40, 41]. Still, these energies are only available at facilities with 4 MV terminal voltage or beyond. The main aim of this work was to continue this trend and establish measurements of ^{36}Cl at energies available with 3 MV accelerators.

2.2.3 New techniques for atomic isobar suppression

In order to overcome the current limitations in isobar suppression, new isobar separation techniques independent of available kinetic energy have been investigated. Such techniques based on physical or chemical properties of the ions can extend measurement capabilities of small as well as large AMS systems to many new isotopes. One of the most promising methods so far, optical filtering via selective photodetachment of negative ions, is based on the differences in electron affinities in the elements under investigation. Proof of principle of optical filtering was demonstrated already 20 years ago by Berkovits et al. [42] for the case $^{36}\text{Cl} - ^{36}\text{S}$. The cross section for photodetachment of $^{36}\text{S}^-$ was measured to be of the order of 10^{-17} cm^2 at a wavelength of 532 nm. The interaction time and the laser intensity required to obtain a substantial depletion can therefore not be obtained with a commercially available laser and an accelerator using keV-ion-beams for injection. Recently, a sulfur suppression factor of at least 10^3 was achieved using photodetachment in an ion cooler [43]. The ion cooler, which is based on a gas-filled radio frequency quadrupole, increased the interaction time of the ion beam and the laser beam. New experiments on Ni and Co with the same technique but an improved detection system show that isobar suppression factors of more than 10^4 can be expected [44].

Another approach using resonant charge transfer in a NO_2 -filled gas reaction cell yielded even isobar suppression factors of 10^6 [45]. While the aforementioned optical filtering is limited to cases where the interfering isobar (or a molecule of it) has a lower electron affinity than the species of interest, suitable charge transfer resonances are expected for almost all elements [46]. Apart from $^{36}\text{Cl} - ^{36}\text{S}$, high isobar suppression with this technique has recently been demonstrated for $^{90}\text{Sr} - ^{90}\text{Zr}$ and $\text{Cs} - \text{Ba}$ isotopes using fluorides [47]. Both of these promising techniques, however, require substantial changes to the injection system of existing accelerators to adapt for an ion cooler or a gas cell. Furthermore, total current throughput of both devices is limited to a few nA, which is less than 1 % of typical ion beam currents in AMS

measurements. Besides, beam losses of $\sim 50\%$ for the wanted ions have to be expected. For these reasons, they have not been applied in routine AMS measurements so far and at this stage probably involve more effort than justified for AMS of ^{36}Cl at 3 MV accelerators.

2.3 The VERA facility

The Vienna Environmental Research Accelerator (VERA) was built by National Electrostatics Corporation (NEC), Wisconsin, USA [48] and began its operation in 1996 [49]. Since then, it has undergone several modifications and upgrades with new elements added to extend its measurement capabilities [50, 51]. Most recently, the injector was modified to accommodate a second negative ion source [52]. The list of radioisotopes measured at VERA includes ^{10}Be , ^{14}C , ^{26}Al , ^{36}Cl , ^{41}Ca , ^{55}Fe , ^{129}I , ^{182}Hf , ^{210}Bi , ^{236}U and ^{244}Pu , most of them at natural abundance levels [6, 53].

VERA is based on a 3 MV Pelletron tandem accelerator and is designed to allow transport of all isotopes up to the heaviest elements, provided that they form negative ions or molecules. The layout of VERA and many of its components are shown in figure 2.2. Each of the two almost identical MC-SNICS ion sources allows to load a wheel of 40 samples, details can be found in [54]. From the ion source, the negative ions are accelerated to typically 70 keV. The electrostatic analyzer switch with one or two 45° deflections (depending on the ion source used) and the 90° injection magnet form the low energy mass spectrometer. The insulated magnet chamber can be set to a potential of 0–13 kV for fast sequential injection of various isotopes into the accelerator with switching times of 20 μs between different masses. After the injection magnet, offset Faraday cups allow to measure stable isotope currents and to monitor the accelerator transmission via comparison with currents on the high energy side. Several ion optical lenses and steerers ensure optimum beam transport to the accelerator. Movable slits at the beam waist positions allow to balance high mass resolution and high transmission for every isotope. The beam current can also be monitored with insertable Faraday cups at various positions. The mass separated beam is then injected into the accelerator, where gas stripping with O_2 is used for most isotopes. Additionally, the terminal is also equipped with a foil stripper but this option is currently only employed for ^{36}Cl measurements. Stability of the terminal voltage is ensured via a controlled corona probe discharge.

After the accelerator, a double-focussing 90° analyzing magnet with a bending radius of 1.27 m and a large 90° electrostatic analyzer with a radius of 2 m form the high energy mass spectrometer. The analyzing magnet has a bending power of $mE/q^2 = 176 \text{ MeV amu}$, the ESA of $E/q = 4.4 \text{ MeV}$, both of which are no limitation for the measurement of ^{36}Cl . Currents of stable reference isotopes are measured by offset Faraday cups behind the analyzing magnet. Light ions without isobars in the beam are counted with a surface barrier detector in the beamline following the ESA.

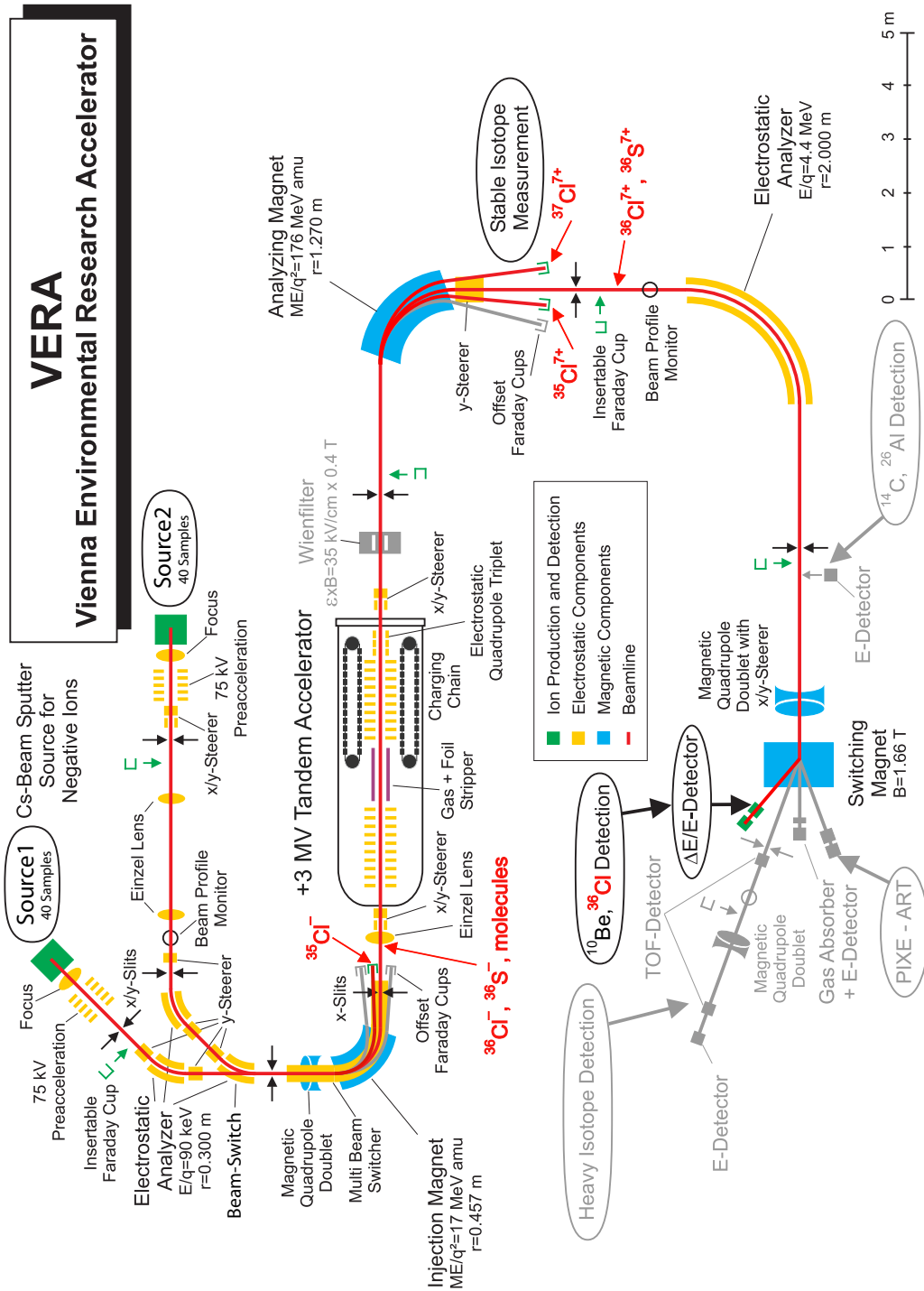


Figure 2.2: Layout of the Vienna Environmental Research Accelerator (VERA) and components used for measurement of ^{36}Cl . Elements plotted in gray are only used for other isotopes.

If further analysis for mass separation or atomic isobar suppression is required, a switcher magnet guides the beam to one of the four dedicated detection beamlines.

Computer control of essentially all components and several automated scripts including the optimization software *automax* [24] allow operation of the accelerator around the clock. Measurement and data evaluation are fully automated and can be remote controlled via a web-interface. Automated initial tuning of the machine has already been successfully implemented for a number of isotopes. The status for ^{36}Cl in this respect is discussed in more detail in chapter 5.

2.4 Previous results from AMS of ^{36}Cl at VERA

Prior to this thesis, considerable progress in AMS of ^{36}Cl was achieved at VERA and much of the work described in the following is based on those results. For this reason, a short summary of the status at the beginning of this work is given below.

First, the potential of a detection method called ΔTOF for the separation of ^{36}Cl and ^{36}S was explored [55]. After mass analysis on the high energy side, the ion beam passes through a degrader foil, where the ions lose part of their energy according to their Z -dependent stopping power. The resulting difference in velocity between ^{36}S and ^{36}Cl is then measured with a time of flight detector. The velocity resolution can be made arbitrarily high (at the cost of lower efficiency) by extending the flight path and isobar separation is only limited by energy loss straggling in the degrader and timing foils. Since chlorine has a higher atomic number than sulfur and thus a lower energy after passage through the degrader foil, low energy tails of sulfur deteriorate the separation. Highly homogeneous silicon nitride foils from Silson, UK [56] reduced this problem but provided only poor secondary charge collection at the timing detectors. Coating the foils with a thin layer of carbon increased the detector efficiency but again introduced significant low energy tails. While this technique was pushed to a suppression of sulfur to a background level of $^{36}\text{Cl}/\text{Cl} \approx 10^{-13}$, it still suffered from a low detector efficiency of less than 10 %. Both values are insufficient for measurements of ^{36}Cl at natural abundances.

Almost at the same time it was discovered that energies of 28.8 MeV for ^{36}Cl are accessible with VERA [6]. Despite that the VERA Pelletron tandem accelerator nominally has a maximum terminal voltage of 3 MV, thorough conditioning of the accelerator allows operation at 3.6 MV. After stripping, the 7+ charge state is selected for the benefit of high energy. While yields with gas stripping for $^{36}\text{Cl}^{7+}$ at 3.6 MeV are less than 1 %, the use of diamond like carbon foils with an areal density of $\sim 0.6 \mu\text{g}/\text{cm}^2$ for foil stripping increased the yield for $^{36}\text{Cl}^{7+}$ to around 9 %.

Simultaneous technical progress in the design and performance of compact ionization chambers [57] recently allowed first measurement of ^{36}Cl exposure dating samples at 3.5 MV [58]. This was the first ^{36}Cl AMS measurement of exposure dating samples at a 3 MV facility. A new split anode ionization chamber [59] provided

an excellent suppression of ^{36}S against ^{36}Cl of 30 000 at 50 % detector efficiency for ^{36}Cl . Nevertheless, the comparable high sulfur content of the ion beam and some cross contamination in the ion source caused a background of $^{36}\text{Cl}/\text{Cl} \approx 3 \times 10^{-14}$. Additionally, results deviated from measurements at other facilities by 25 %. Another important outcome was that a charge state yield of 19 % for the 7+ charge state in terminal stripping was achieved at 3.5 MeV with carbon foils produced by laser ablation [60].

Unfortunately, operation of the accelerator at terminal voltages of ~ 3.5 MV is only feasible in a certain period after maintenance and additionally requires conditioning times of several days. On the other hand it was found that the separation of ^{36}Cl and ^{36}S in the ionization chamber decreases very strongly towards lower energy. In order to explore the possibility of lowering the terminal voltage to the nominal value of 3 MV, the performance of various detection systems for the separation of ^{36}Cl and ^{36}S at 24 MeV was investigated [61]. While the ionization chamber alone provides insufficient sulfur suppression at this energy, the addition of a time of flight or a silicon strip detector yielded quite satisfying experimental results. In test measurements, a ^{36}S suppression factor of slightly over 10 000 was achieved. The physics behind this increase in sulfur suppression however required further investigations.

A reduction of ^{36}S in the ion beam with a degrader foil and an additional bending element prior to the detector was considered as well, but simulations showed that high beam losses have to be expected and this approach was not further pursued. Finally, tests with different foil thicknesses for terminal foil stripping proved that the highest yield for $^{36}\text{Cl}^{7+}$ at 3 MeV of 15 – 17 % is obtained with the above mentioned $2.6 \mu\text{g}/\text{cm}^2$ carbon foils and neither thicker nor thinner foils gave better results. Summarizing, the main outstanding tasks for establishing competitive AMS measurements of ^{36}Cl at VERA were:

- a thorough investigation of the parameters determining the isobar suppression in the detection setup in order to explore the potential for further optimization
- a reduction of sulfur output from the ion source and the development of a proper source regulation including the determination of cross contamination
- the development of a measurement procedure for chlorine and the determination of background, precision and accuracy

Furthermore, new techniques for additional suppression of the isobar ^{36}S were investigated.

3 Sulfur suppression with the $\Delta E/E$ detection setup

3.1 The ΔE -E detection setup

A schematic of the detection setup for ^{36}Cl and ^{36}S is shown in figure 3.1. It consists of an ionization chamber with segmented anodes and a silicon strip detector sitting 30 cm behind the exit window of the ionization chamber. For particle identification, it provides two differential energy loss measurements (ΔE_1 , ΔE_2) and a residual energy measurement (E_R). Additionally, the silicon strip detector allows for measurement of the projectile's final position (P_X , P_Y). These two detectors are discussed in more detail in the following sections.

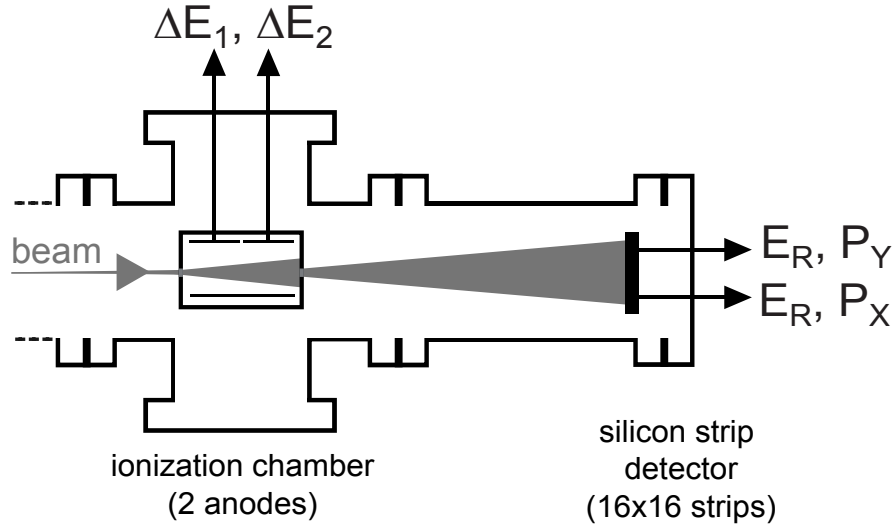


Figure 3.1: Schematic of our detection setup for ^{36}Cl and ^{36}S . It provides two differential energy loss measurements and a residual energy measurement as well as xy-position information from the silicon strip detector.

3.1.1 The ionization chamber

The compact ionization chamber with a split anode is based on a design developed at the ETH Zurich by Stocker et al. [57]. For the measurement of ^{36}Cl it was slightly modified and equipped with an exit window of the same design as the entrance window. The windows are silicon nitride foils from Silson Ltd. [56] with a nominal thickness of 100 nm and a size of $5 \times 5 \text{ mm}^2$. Due to their homogeneity, these foils introduce a very low energy straggling [62] and were tested to withstand more than 150 mbar pressure.

Figure 3.2 shows a true-to-scale representation of the ionization chamber. The detector is mounted into a DN-100-CF-cross piece and can be vertically moved into and out of the beam. The anode is split into two sections of equal size, each 32 mm long and 47.5 mm wide. Since the distance between the windows is only 56.4 mm, the anodes stretch ~ 4 mm over the window holders. This ensures efficient charge collection in the window region. The Frisch grid is made of gold coated tungsten wires with 20 μm diameter. The distance between the wires is 0.5 mm. The grid sits 5 mm below the anodes, the distance between the grid and the cathode is 25 mm. The working principle of an ionization chamber and the detector resolution are discussed in detail in sections 3.3.1 and 3.3.2. The cathode and the detector housing are grounded while the anode is set to +200 V. The Frisch grid is set via a resistive voltage divider to 60 % of the full voltage. The ionization chamber can be either filled with counting gas and closed off or operated with a constant gas through-flow. In front of the detector, a shield with two different apertures (3 and 6 mm diameter) can be inserted. Further details about the ionization chamber can be found in [64].

3.1.2 The silicon strip detector

The residual energy detector is a double-sided silicon strip detector Design W1(DS)-300-PCB from Micron Semiconductors [65] with an active area of $50 \times 50 \text{ mm}^2$ and a thickness of 300 μm . Each side consist of 16 strips with a widths of 3.0 mm and 0.5 mm gap in between. The two sets of strips are rotated by 90° against each other resulting in 256 pixels. The detector is mounted on an isolated end flange and a bias voltage of -50 V is applied to the front junction side (p-side). Both sides of the detector are covered by 100 nm deposited aluminum as windows. A photo of the detector is shown in figure 3.3.

The readout electronics consists of two MUX-16 modules from Mesytec [66]. They provide 16 channels of charge sensitive preamplifiers with subsequent shapers, timing filter amplifiers and leading edge discriminators. Responding channels are switched to an output bus line and the position information is sent as an amplitude-coded signal to a separate output line. The amplitude of the position signal lies between 100 and 300 mV. In case a projectile hits between the strips and leaves a signal on two of them simultaneously, the second signal is put on a spare output line with according

position information. Thus, 8 signals (2 energy signals and 2 position signals from each set of strips) have to be recorded for full information. A NIM trigger output is also provided.

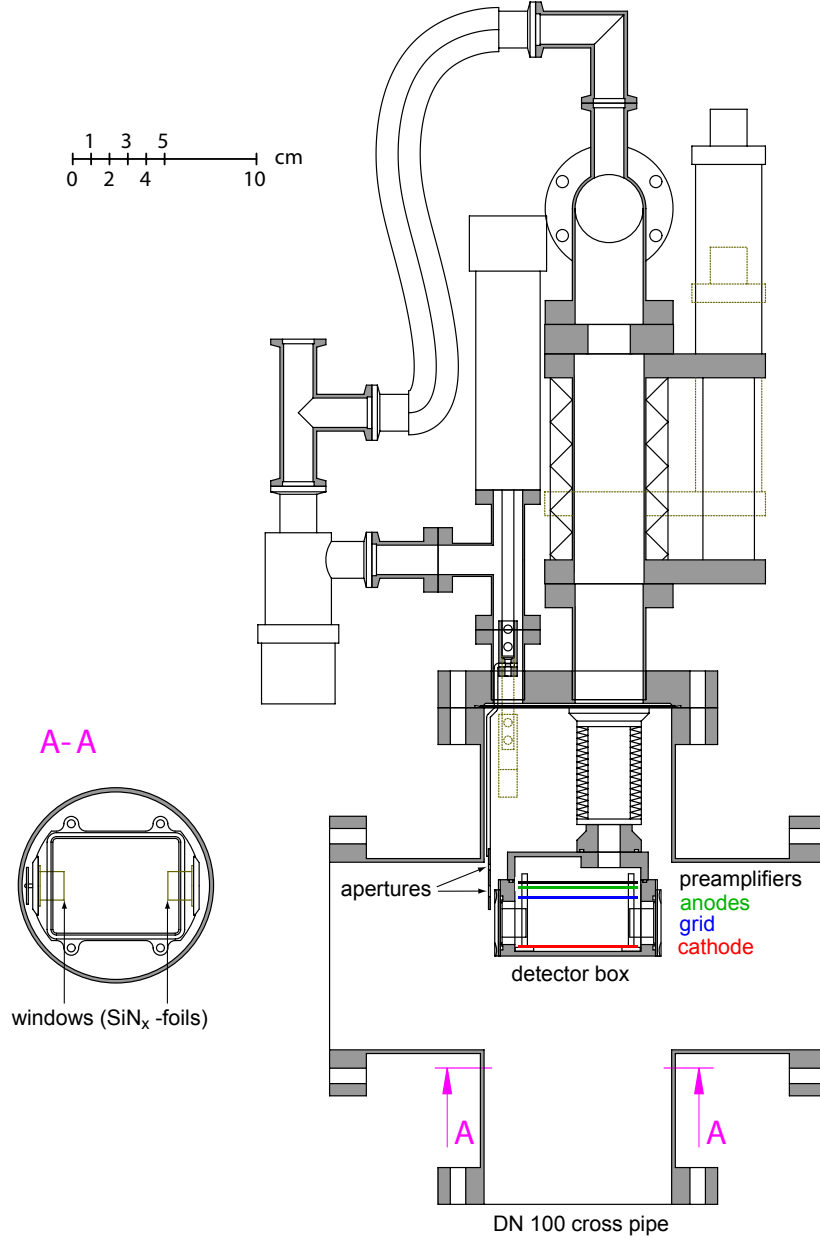


Figure 3.2: True-to-scale drawing of the ionization chamber used for ^{36}Cl measurements. The drawing is based on a figure by Forstner et al. [63]. Part of the gas handling system is also shown.

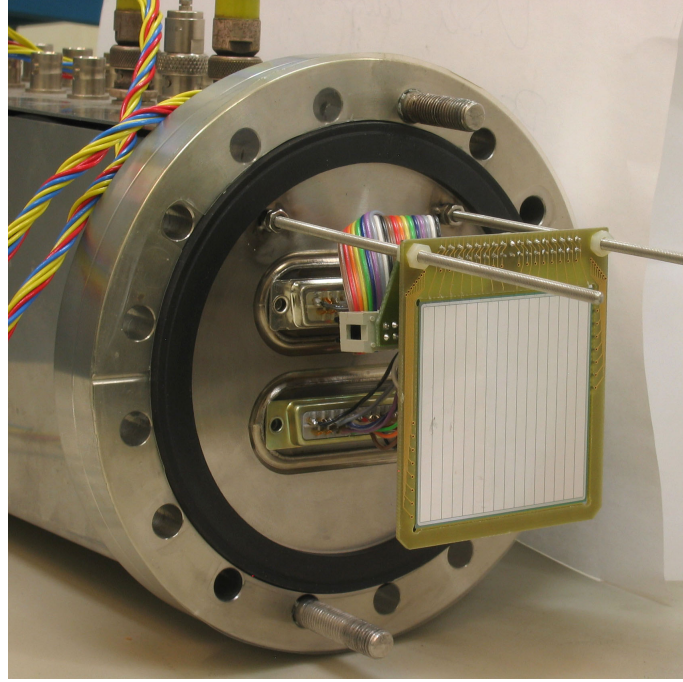


Figure 3.3: Photo of the silicon strip detector mounted on an endflange. The 16 strips providing x-position information are clearly visible. Strips at the backside are rotated by 90° angle to provide y-position information.

3.2 Introduction to energy loss of ions in matter

This section comprises a short introduction to the energy loss of ions in matter, since this is the physical basis to optimize isobar separation in the detection setup. I will concentrate on a few important models and formulas and focus on the energy range around and below 1 MeV/amu, which is most relevant in AMS. A more detailed collection of the numerous publications on this topic is given by Ziegler et al. [67].

3.2.1 Energy loss and stopping power

When passing through matter, ions lose their energy by Coulomb-interactions of their atomic charge both with the target electrons (electronic stopping) and the screened nuclear charge of target atoms (nuclear stopping). Although this is in principle a discrete process of energy transfer, the energy loss can be macroscopically described as a continuous function due to the sheer number of interactions. The stopping power $S(E)$ is defined as

$$S(E) = - \lim_{N\Delta x \rightarrow 0} \frac{\Delta E}{N\Delta x}(E) \quad (3.1)$$

where ΔE is the average energy loss of an ion and $N\Delta x$ the areal density of the target. It is commonly given in units of $\text{eV}/(\text{atom}/\text{cm}^2)$ or $\text{MeV}/(\text{mg}/\text{cm}^2)$. According to Bragg's rule, the stopping power for a composite material can be estimated as the linear combination of the individual stopping powers of the constituents [68].

$$S(A_mB_n) = m \cdot S(A) + n \cdot S(B) \quad (3.2)$$

The validity of Bragg's rule is limited to materials which have an electronic excitation behavior similar to their individual components, in other cases significant deviations have been observed. Bragg's rule therefore gives a good estimate of the stopping power of a mixture of gases where the stopping powers of the individual gases are well known (e.g. argon-methane). Figure 3.4 shows the electronic and nuclear stopping power of ^{36}S in isobutane as a function of kinetic energy. Over a large energy range, electronic stopping (blue curve) is the dominant process. Only at energies below 1 MeV, where electronic stopping is very low, nuclear stopping (red curve) contributes significantly to the total stopping power (gray dotted curve).

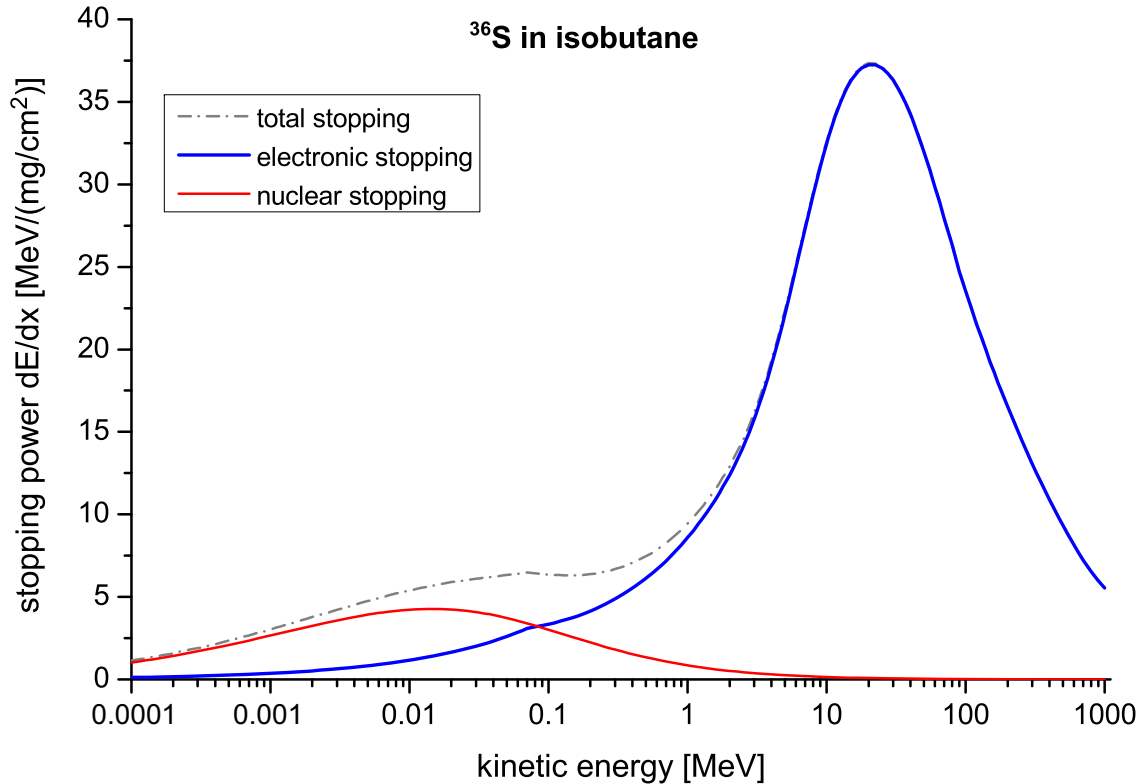


Figure 3.4: Electronic and nuclear stopping power of ^{36}S in isobutane as a function of kinetic energy according to SRIM [69]. Nuclear stopping only plays an important role for energies below 1 MeV. Above, electronic stopping is the dominant process.

A uniform description of the non-relativistic part of the electronic stopping power curve is difficult. Since several effects occur only in specific energy ranges, these have to be considered separately. The key parameter is the projectile's velocity. For fully stripped particles, the model of Bethe [70] and Bloch [71] very well describes the electronic stopping, which is proportional to $1/E$ for higher energies.

$$S_{\text{electronic}} = \frac{4\pi Z_P^2 e^4}{m_e v_P^2 (4\pi\epsilon_0)^2} Z_T \left\{ \ln \left(\frac{2m_e v_P^2}{I(1 - \beta^2)} \right) - \beta^2 \right\} \quad (3.3)$$

(Z_P is the atomic number of the projectile, Z_T the atomic number of the target, v_P the projectile's velocity, m_e the electron mass, I the mean excitation potential and β is v_P/c .) As can be seen, the stopping power is proportional to Z_P^2 , so the stopping power is higher for elements with higher atomic number.

With decreasing projectile velocity, the probability for electron capture increases and the interaction can no longer be described as purely elastic. As a rule of thumb, an ion stays fully stripped as long as the projectile's velocity is higher than the classical velocity of the innermost electron $v_e = Z_P \cdot v_0$, with $v_0 = 2.2 \times 10^6$ m/s. Therefore, all but the lightest ions have projectile charges smaller than the atomic number at energies of a few MeV/amu typical for AMS. At these energies, the projectile's charge state is determined by electron loss and electron capture processes in numerous collisions. The actual charge state of an ion fluctuates around a mean charge state, which depends on the projectile's velocity and atomic number, but also on target properties such as the mean free path. The probability that the ion adopts a certain charge state is described by the equilibrium charge state distribution $\Phi(q, v_P, Z_P)$. Calculation of Φ based on all electron capture and electron loss cross sections is difficult, therefore semi-empirical formulas for Φ have been developed [72]. To account for bound electrons, equation 3.3 has to be modified by substituting Z_P with the lower mean effective charge q_{eff} .

$$S_{\text{electronic}} = \frac{4\pi q_{\text{eff}}^2 e^4}{m_e v_P^2 (4\pi\epsilon_0)^2} Z_T \left\{ \ln \frac{2m_e v_P^2}{I} \right\} \text{ with } q_{\text{eff}} = \sqrt{\sum_{q=0}^{Z_P} q^2 \cdot \Phi(q, v_P, Z_P)} \quad (3.4)$$

The stopping power still depends on the atomic number of the projectile as the mean effective charge q_{eff} is a function of the atomic number Z_P . This allows for identification of projectiles of the same mass and energy but different atomic number via their energy loss characteristics.

Towards lower particle energies, the closest distance of interaction between the projectile and a target atom increases. Therefore the shielding of the projectile's atomic charge by the outer shell electrons has to be taken into account, which reduces the stopping power. The maximum of the stopping power curve (Bragg maximum) lies around the Thomas-Fermi velocity $Z_P^{2/3} v_0$, for lower velocities $S_{\text{electronic}}$ becomes proportional to v_P [73].

At very low velocities, nuclear stopping becomes the dominant process (the red curve in figure 3.4). The energy transfer now happens via the Coulomb interaction between the target's and projectile's shielded nuclear charges and can be described as elastic scattering. Many models with different screening functions to describe the interatomic potentials exist, an overview and comparison is given in [67]. Generally, the nuclear stopping power rises to a maximum and then monotonically goes to zero with decreasing velocity (see e.g. [73]).

3.2.2 Energy loss straggling

The energy loss of ions in matter is a statistical process where both the number of projectile-target interactions as well as the amount of energy transferred to the target vary. Therefore, the energy losses of identical projectiles will fluctuate around a mean value. This statistical uncertainty is called energy loss straggling. It determines the achievable resolution in applications where information is deduced from the energy loss of ions in matter. A widely used approach to describe energy straggling in electronic stopping is the Bohr formula [74], where the straggling δE is proportional to the square root of the target thickness Δx and the square root of the target's atomic number Z_T , but independent from the incident energy.

$$\delta E_{Bohr} \propto Z_P \cdot \sqrt{Z_T \Delta x} \quad (3.5)$$

However, this equation is only valid for high particle energies, where the projectile is fully stripped. At energies of several MeV/amu, all but the lightest ions have equilibrium charge states lower than the atomic number (see the previous section). In this energy range, a significant contribution to energy straggling comes from fluctuations of the projectile's charge state and energy straggling is largely underestimated by equation 3.5. For thin targets, semi-empirical formulas are given by Yang et al. [75], which also describe the significant drop in energy straggling below the Bohr straggling observed at very low ion energies. For chlorine and sulfur, the maximum of $\delta E / \delta E_{Bohr}$ lies around 100 MeV, but even at 24 MeV the energy straggling is about 20 % higher than predicted by Bohr straggling.

For thick targets and higher energy losses, the variation of the stopping power S with decreasing kinetic energy along the ion's flightpath also has to be taken into account [76]. Since the stopping power changes with energy, the energy loss in one section is no longer independent from losses in other sections. For large energy losses, the straggling for a projectile with constant charge q is therefore modulated with the factor (see [77])

$$\delta E \propto \frac{S(E_0 - \Delta E)}{S(E_0)} \quad (3.6)$$

In flat regions of the stopping power curve this correction term is almost one while above the Bragg maximum the effect leads to a slight increase in energy straggling.

Below the Bragg maximum however, the stopping power is steadily decreasing with decreasing energy. In this energy range, the correlation of energy losses therefore results in a focusing effect. Ions with lower energy loss than average in the past intervals of the target experience a higher stopping power in the coming section and vice versa. Schmidt-Böcking and Hornung [77] verified this effect experimentally and gave a semi-empiric formula for the energy straggling δE (FWHM of the energy loss distribution) in thick gas targets

$$\delta E = \Delta E^{0.53} \cdot \frac{S(E_0 - \Delta E)}{S(E_0)} \cdot c(v_P, Z_P, Z_T) \quad \text{with } c \approx 14 \cdot \sqrt{\frac{Z_P \cdot Z_T}{Z_P^{1/3} + Z_T^{1/3}}} \quad (3.7)$$

where S is the stopping power at the given energy, E_0 the initial kinetic energy and ΔE the mean energy loss in the respective section. The scaling function $c(v_P, Z_P, Z_T)$, with v_P being the projectile's velocity and Z_P and Z_T the projectile's and target's atomic number, was fitted to experimental data for isobutane and argon-methane. Equation 3.7 gives the energy loss straggling in keV if ΔE is entered in MeV. A discussion of the validity of the above equations based on our experimental data is presented in the next sections.

Nuclear stopping, where kinetic energy is transferred to a target atom in collisions, also affects the energy loss distribution since it introduces a tail of high energy loss. Additionally the projectile is scattered at small angles during this process. Subsequently, it deposits more energy per unit length along the initial longitudinal direction due to a longer flight path. These tails in the energy loss spectra limit the resolution in applications where the species of interest has a higher atomic number and thus a higher energy loss than the interfering species, which is the case for the separation of ^{36}Cl from ^{36}S .

3.3 Isobar separation with the ΔE -E detection setup

To first order, the capability of distinguishing particles of interest from interfering background by their difference in energy loss when passing through matter is determined by the separation, which, at least for a one-dimensional spectrum, is given by

$$Sep = \frac{\Delta E_{12}}{\sqrt{\delta E_1^2 + \delta E_2^2}} \quad (3.8)$$

where ΔE_{12} is the total difference in energy loss of the two species (the distance between the peaks in the spectrum) and δE_i are the widths of the individual peaks (determined by energy loss straggling and the energy resolution of the detection setup). For isobar suppression with the ΔE -E method, ΔE_{12} is theoretically given

by the difference in energy loss due to different stopping powers.

$$\Delta E_{12} = \int_{E_0}^{E_0 - \Delta E} \frac{dE}{dx}(Z_1) - \frac{dE}{dx}(Z_2) dx \quad (3.9)$$

With a specific initial particle energy E_0 , ΔE_{12} can only be optimized by changing either the gas pressure or the lengths of the anodes, which both also affects the widths δE_i of the measured energy loss distributions. In order to find an optimum configuration, ΔE_{12} and the widths δE_i have to be studied more closely, which is done in the following two sections.

3.3.1 The energy loss signal from an ionization chamber

A schematic of the working principle of an ionization chamber is shown in figure 3.5. The projectiles enter the gas volume through a thin entrance window and are consequently slowed in the gas. In order to translate this energy loss of ions into a detectable signal, the ionization charges created during the stopping process have to be collected by applying an appropriate electric field. The electric field prevents the free electrons created in the stopping process from recombining with the positive target ions and the charges move according to the electric field. Thereby, they induce mirror charges on the electrodes which can be integrated and shaped to a signal, whose size is a function of the primary ionization and thus the energy loss. In most

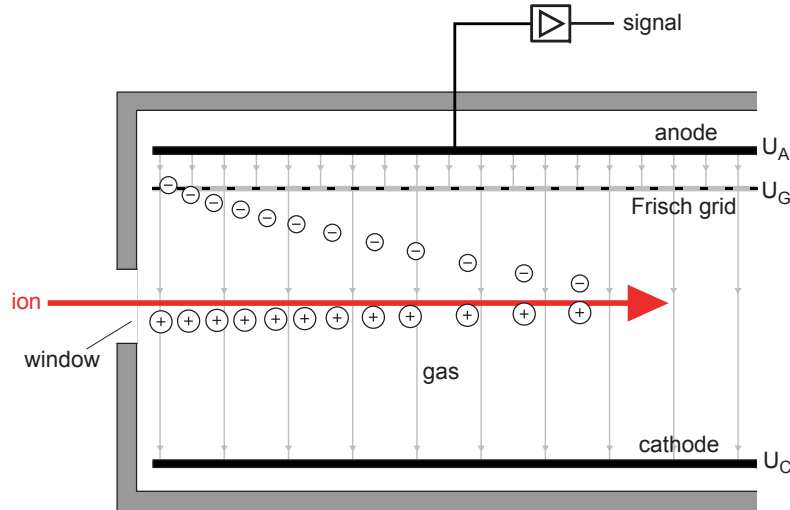


Figure 3.5: Schematic of the working principle of an ionization chamber. The charges created during the stopping process of ions move according to the electric field and induce a signal in the electrodes.

ionization chambers, the electrodes are plates or grids parallel to the direction of the projectile's propagation. Since the drift velocity of electrons is ~ 1000 times higher than that of target ions, they quickly move towards the anode while the positive ions stay comparable long in the gas volume until they reach the cathode. Drift velocities for electrons in isobutane are around $50 \text{ mm}/\mu\text{s}$ at typical gas pressures and electric field strengths [78]. This means that electrons are quickly removed from the gas volume and the signal generated by them is quite short, which allows high particle count rates. In most ionization chambers, a Frisch grid is used in front of the anode to reduce the dependence of the induced signal on the distance between ion trajectory and the anode and to minimize the reduction of the induced signal by the positive charge cloud (see section 3.3.2). A more detailed overview of ionization chambers is given in [79].

Measurement of the specific energy loss in certain sections of the ionization chamber can be achieved by segmenting the anodes and allows for particle identification. Diagonal segmentation of one or more anodes even allows to obtain information about the particle's movement perpendicular to the initial direction (e.g. [41, 80]). The principle of isobar separation is illustrated in figure 3.6 for ^{36}Cl and ^{36}S with an initial energy of 23.4 MeV in 55 mbar isobutane. Due to its higher stopping power, the energy loss of ^{36}Cl under Anode1 (ΔE_1) is larger than that of ^{36}S . After a certain distance, the difference in residual energy is so high that ^{36}S experiences a higher stopping power than ^{36}Cl and subsequently deposits more energy in the latter sections. At this crossing point of the stopping power curves, the difference in energy loss ΔE_{12} is highest.

However, the energy loss of the projectile does not translate straightforward into an amplitude of the signal collected at the anodes. First, the efficiency of charge collection depends on the homogeneity of the electric field and possible electric field deformations play an important role, especially at the border between segmented anodes and the window area [81]. The electric field and the gas pressure have to be chosen such that the drift velocity is high enough to prevent recombination of ionization charges. Furthermore, not all of the primary energy goes into the production of charge. While the ionization energy of isobutane is 10.68 eV [82], the creation of an electron-ion-pair requires on average 23.4 eV [83]. The remainder goes into excitation of target electrons or molecules, kinetic energy of the ionization electrons, charge fluctuations of the projectile or kinetic energy of target atoms in nuclear stopping. Only part of this energy contributes to the total charge via secondary ionization or the Auger process, the rest is dissipated via radiation and other non-ionizing processes. Since the fraction of non-ionizing energy loss is a function of the projectile's atomic number and mass, the response of the ionization chamber is not the same for all projectile species. This effect is called pulse height deficit [84]. Projectiles with a low Z produce a higher signal per unit energy than heavy projectiles and also an isotopic effect is observed. The pulse height deficit is not solely accounted for by the amount of energy transferred into non-ionizing processes but also by multiple ioniza-

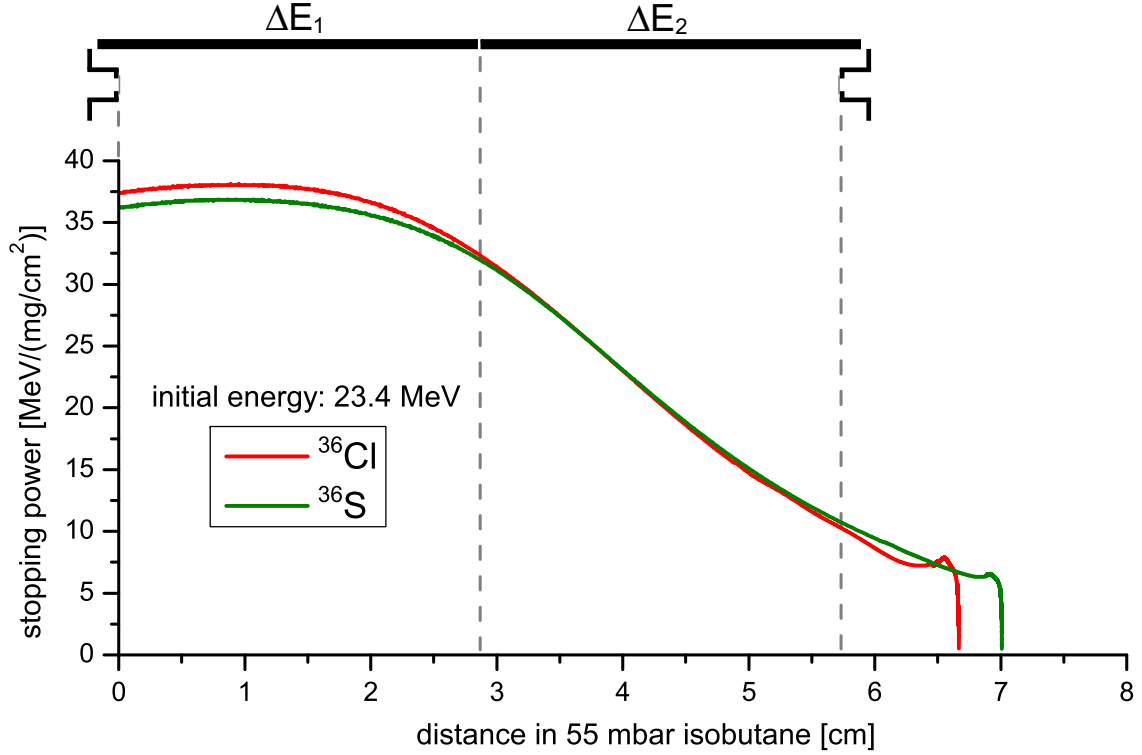


Figure 3.6: Isobar separation of ^{36}Cl (red) and ^{36}S (green) in an ionization chamber based on the characteristic energy loss of the respective ions in 55 mbar isobutane. The stopping power plotted here is the total stopping power according to SRIM [69]. Each anode collects the ionization charges created in a 28.2 mm long section of the gas volume. In our setup, the residual energy after passage through the exit window is collected by the silicon strip detector.

tion of individual target atoms due to high ionization densities along the projectile's track [85].

As a consequence of this pulse height deficit, the difference in measured energy loss signals from two isobars is slightly smaller than expected from their stopping powers. Experimental data from Weijers et al. [84] for 50 MeV ions with propane as detector gas suggest that the pulse height deficit for ^{36}S and ^{36}Cl is around 7-8 %. While the deficit for chlorine is slightly higher, the overall difference is almost negligible concerning isobar separation. For isobars with a low relative difference in atomic number, the measured distance of the peaks in the energy loss spectrum ΔE_{12} can be very well inferred from the integrated difference in stopping power. Looking at the pulse height deficits for elements with very different atomic number, however, it's apparent that the energy calibration of an ionization chamber has to be made with the species of interest and can not be scaled straightforward to other projectiles. Details about the energy calibration of the detection setup are given in section 3.4.1.

3.3.2 Detector resolution

Several processes contribute to the total resolution δE_{tot} of the ionization chamber. They are discussed individually in the following concerning their relevance for the separation of ^{36}Cl and ^{36}S at 24 MeV. Since they are independent from each other, δE_{tot} (the FWHM of the measured ΔE -distribution) can be calculated by quadratic summation of all contributions.

$$\delta E_{\text{tot}}^2 = \delta E_{\text{beam}}^2 + \delta E_{\text{window}}^2 + \delta E_{\text{elec}}^2 + \delta E_{\text{det}}^2 + \delta E_{\text{gas}}^2 \quad (3.10)$$

δE_{beam} : The ion beam delivered by the accelerator is not strictly mono-energetic but has a small energy spread δE_{beam} caused by fluctuation of the terminal voltage and by energy straggling in the carbon stripping foil. The FWHM of the energy distribution of a 24 MeV $^{35}\text{Cl}^{7+}$ beam was measured to be 0.5 ‰, which corresponds to 12 keV. The same values were obtained with $^{34}\text{S}^{7+}$. The contribution of the ion beam is in our case of little significance for the total resolution.

δE_{window} : The use of very homogeneous, thin silicon nitride foils as detector windows has considerably extended the measurement capabilities of ionization chambers at energies around 1 MeV/amu [62]. These foils introduce only little energy straggling compared to the previously employed Mylar windows, where δE_{window} was the main limitation for the detector resolution. Table 3.1 shows energy loss and energy straggling of ^{36}Cl and ^{36}S in a 100 nm thick silicon nitride window calculated by SRIM [69]. The calculations with an initial energy of 24 MeV simulate the influence of the entrance window, which contributes to the detector resolution, the 3 MeV values correspond to the exit window. The exit window however does not affect the resolution of the ionization chamber but only the residual energy measurement in the silicon strip detector. The calculations were performed based on a stoichiometry of $\text{Si}_3\text{N}_{3.1}\text{H}_{0.06}$ [62] and a density of 3.1 g/cm³ [86] for silicon nitride. The calculated values, especially for δE_{window} have to be treated with care since significant discrepancies between measured energy straggling values for silicon nitride and the results from

| isotope | E_0 [MeV] | ΔE [keV] | δE_{window} (FWHM) [keV] |
|------------------|----------------|---------------------|--|
| ^{36}Cl | 24.0 | 595 | 63 |
| ^{36}S | 24.0 | 573 | 59 |
| ^{36}Cl | 3.0 | 271 | 64 |
| ^{36}S | 3.0 | 255 | 61 |

Table 3.1: Energy loss and energy straggling of ^{36}Cl and ^{36}S in a 100 nm silicon nitride foil according to SRIM.

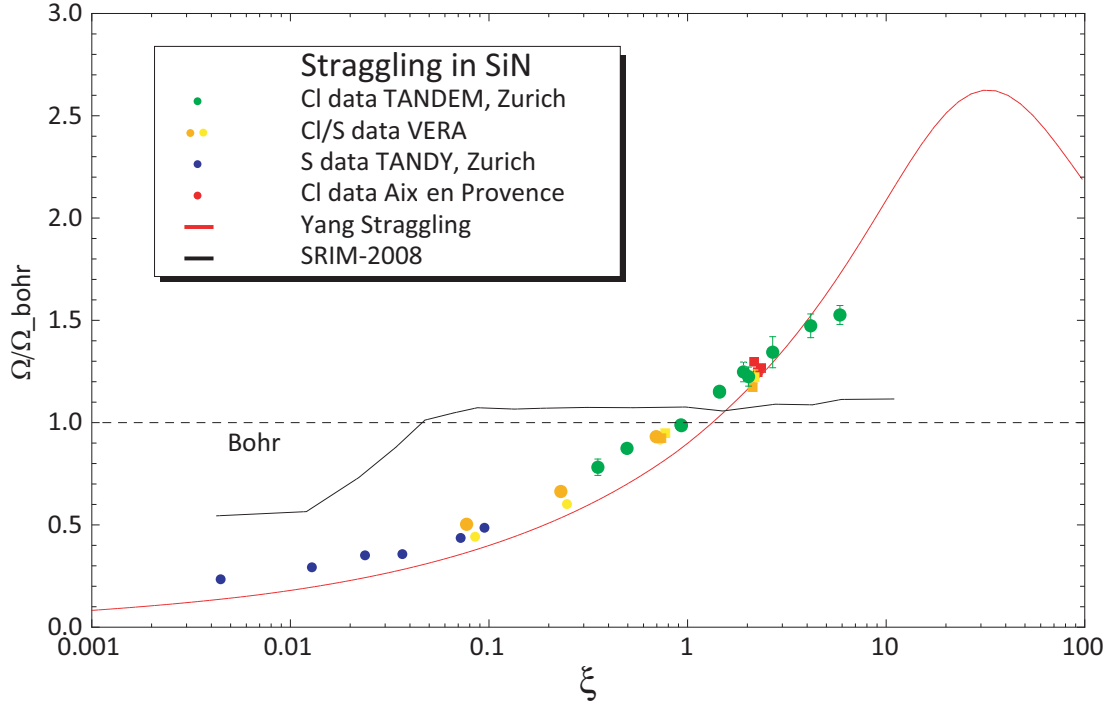


Figure 3.7: Measurements of energy straggling of sulfur and chlorine in silicon nitride foils relative to Bohr straggling as a function of energy. The figure has been taken from [88]. There are significant discrepancies between the experimental values and the results obtained with SRIM. In contrast, the Yang model [75] gives a good estimate of the energy straggling.

SRIM have been observed [87]. Figure 3.7 shows experimental values for the energy straggling of sulfur and chlorine in silicon nitride measured by Vockenhuber et al. [88]. They deviate significantly from the results of simulations with SRIM or the Bohr straggling model, whereas the semi-empirical formulas by Yang et al. [75] predict the energy straggling quite well (see section 3.2.2 for details on the straggling models). The plotted dimensionless velocity parameter ξ is defined as (see [86])

$$\xi = 6.93 \cdot 10^3 \cdot \frac{\left(\frac{E}{A}\right)^{3/2}}{Z_P \cdot I} \quad (3.11)$$

where E is the projectile energy in MeV, A and Z_P the mass and atomic number and I the mean excitation energy for $\text{Si}_3\text{N}_{3.1}$ of 117.2 eV. For ^{36}Cl and ^{36}S at 24 MeV, ξ is 1.89 and 2.01, respectively. It can therefore be expected that the values in table 3.1 for 24 MeV obtained with SRIM are 10 – 15 % too low. Thus, 70 keV is a good estimate for δE_{window} . In contrast, the straggling values for the exit window in table 3.1, where the ions have ~ 3.0 MeV kinetic energy left ($\xi \approx 0.085$), are overestimated by SRIM.

δE_{elec} : Electronic noise influences the measurement of the charge collected at the anodes and thereby contributes to the detector resolution. The limiting factor is usually the input capacitance and the intrinsic noise of the preamplifiers. The input capacitance can be kept low by reducing cable lengths, therefore the CR-110 charge sensitive preamplifiers from CREMAT Inc [89] are mounted directly above the anodes [64]. An optimized anode configuration and the use of Peltier-cooled FETs can further reduce the electronic noise, which brings significant improvements for applications with light ions at energies of several hundred keV [86]. In our case, electronic noise is no limitation for the detector resolution. Since also the amplifier and the ADC have an influence, it is best to measure the electronic contribution in the final setup using a pulser. In the measurement setup, the FWHM of the recorded pulser signal is equivalent to 46 keV, which is a bit higher than the resolution expected from experimental values for ^{10}Be in [90] also using CREMAT preamplifiers. Part of the reason is the lower ionization yield for heavier ions (our value is based on a ^{36}S energy calibration). Furthermore, no emphasis was put on special shielding of the electronics since the above value for δE_{elec} is reasonably small compared to δE_{window} and especially δE_{gas} .

δE_{det} : Several effects lead to fluctuations of the charge collected at the anodes as well as variations in the shape of the induced signal at the anodes. First, recombination of produced charges is a statistical effect and leads to fluctuations of the charge arriving at the Frisch grid. Scattering of electrons during the drift also causes a widening of the charge cloud and the electrons do not follow the field lines exactly. As a result, these electrons may induce a signal in a different anode around the border region between anodes. An influence of the position of charge production on the collection efficiency can also not be excluded, especially in the window areas. These effects are hard to disentangle from the contribution of the detector gas itself.

Another dependency of the final pulse height on the position of charge production arises from the inefficiency of shielding by the Frisch grid. Due to this inefficiency of shielding, a small signal is already induced in the anode while the charges drift towards the grid. Since the drift time to the grid and thus also the induced signal depends on the y-position of charge production, this effect has an influence on the height of the final signal from the main amplifier. The size of the effect can be estimated by calculating the inefficiency of shielding based on the detector geometry and the formula by Bunemann et al. [91] for an infinitely-large detector

$$\sigma = \frac{d}{2\pi a} \cdot \ln \left(\frac{d}{2\pi r} \right) \quad (3.12)$$

(where d is the distance between the grid wires, r the radius of the wires and a the distance between grid and anode). In our ionization chamber (see section 3.1.1) the inefficiency of shielding according to the above formula is 3.3 %. The influence of the

small induced signal on the shaped main amplifier signal is only $\sim 1.5\%$ because the electric field and hence also the drift velocity in the region below the Frisch grid are smaller than in the area between grid and anode. The vertical distribution of the initial beam has a width (FWHM) of around 2 mm. At the end of the ionization chamber the beam has a width of 3 mm according to the losses at the exit window aperture. The mean drift length to the grid is 12.5 mm. Based on these data, the expected widths in the energy loss spectra due to the inefficiency of shielding are $\sim 0.27\%$ for the ΔE_1 signal and $\sim 0.33\%$ for the ΔE_2 signal. Assuming 20 MeV energy loss in the ionization chamber, this corresponds to a δE_{det} of at least 60 keV for the total energy loss signal ($\Delta E_1 + \Delta E_2$).

δE_{gas} : With particle energies of ~ 24 MeV for ^{36}Cl and ^{36}S , the dominant process for energy loss in the gas is the interaction of the projectile's screened nuclear charge with the target electrons (electronic stopping). Using equation 3.7, the energy straggling for the respective isotopes in isobutane is around 300–400 keV for energy losses of a few MeV. This is in reasonable agreement with measured values (compare figure 3.8) corrected according to equation 3.10 and already suggests that δE_{gas} is the dominating factor for the resolution in a ΔE measurement. But also for constant energy deposition of the projectile, like in the case of full energy loss, the energy signal from an ionization chamber will vary due to fluctuations in the number of produced electron-ion-pairs. As described above, not all of the projectile's kinetic energy goes into ionization of the target and a noticeable fraction is transferred via non-ionizing processes. The relative variation of the number of produced charge-pairs δ_I (FWHM) is generally described by the Fano formula [92]

$$\delta_I = 2.35 \cdot \sqrt{\frac{F \cdot I}{\Delta E}} \quad (3.13)$$

where I is the average energy to create an electron-ion pair and F the target-dependent Fano-factor. According to measurements with electrons and X-rays, the Fano-factor for isobutane is close to 0.26 [93, 94]. Assuming an energy loss of 10 MeV, δ_I is therefore less than 2‰. This is negligibly small compared to the actual variation of energy loss in the ionization chamber due to energy straggling. However, recent observations have shown that the contribution of the gas to the detector resolution for heavier ions is much larger and has a significant dependence on the atomic number of the projectile [86, 95]. The Fano theory in the above form is no longer applicable, especially at low ion energies [96]. This behavior is mostly attributed to nuclear stopping [95, 97], where a comparably large amount of energy is transferred in only very few interactions. Since this process occurs mainly at low residual energy, its effect on δE_{gas} has to be taken into account for almost full energy loss. During most of the stopping process of 24 MeV ^{36}Cl or ^{36}S , where electronic stopping is the dominant interaction, this contribution of the gas may actually be quite low. But also other

processes such as multiple-ionization or charge-changing of the projectile will have an effect. With isobutane, the measured width of the peak from full energy loss of 23.4 MeV ^{36}S is $\delta E_{\text{tot}} \approx 200$ keV. After correction of all other contributions including the inefficiency of shielding according to equation 3.10, the width δE_{gas} is around 170 keV. Hence, δE_{gas} is by far the largest contribution for δE_{tot} , even without energy straggling. For ΔE measurements, a clear distinction between energy straggling and the contribution of the gas itself is very difficult and can only be done to a certain extent.

Summarizing, for all but the lightest ions, electronic noise and straggling in the entrance window are small compared to the contribution of the detector gas even down to initial particle energies below 1 MeV [96]. The limiting factor for the resolution of the ionization chamber and the peak widths δE_i is therefore δE_{gas} . A detailed discussion of the properties of various detector gases is given in section 3.4.

3.3.3 Isobar separation below the Bragg maximum

In principle, high particle energies are essential for isobar separation with an ionization chamber because all major contributions to the detector resolution decrease with increasing energy. Angular scattering is roughly proportional to $1/E$ and the relative energy straggling also becomes smaller at higher initial energies. However, the maximum energy is usually limited by the available terminal voltage and the small yield for high charge states in the stripping process. Subsequently it is important to ensure optimum use of the ionization chamber with the given particle energy in order to achieve maximum isobar separation according to equation 3.8. It's important to consider that the ideal mode of operation does not only depend on the isotopes of interest but changes also significantly depending on the available initial energy and the shape of the respective stopping power curves.

Above the maximum of the Bragg curve in the energy range of $\sim 25 - 50$ MeV, the stopping power is almost constant and the energy straggling correction factor described in equation 3.6 is slightly above 1. Since in this energy range the energy straggling always increases along the flightpath ($\delta E \propto \sqrt{\Delta E}$), it would be best for maximum isobar separation to measure up to the crossing point of the respective energy loss curves (maximum distance of peaks ΔE_{12}). After the crossing point, the distance of peaks starts to decrease and the ever increasing straggling deteriorates the separation even more.

Below the maximum of the Bragg curve, however, the situation is very different. Since the stopping power is steadily decreasing with decreasing kinetic energy, the straggling correction factor (equation 3.6) is significantly smaller than 1. This results in the so-called energy focussing effect. The peak widths δE_i , which are mainly determined by the straggling in the detector gas, decrease towards high energy losses. The reason for the focussing effect is that ions with a deviation from the mean energy

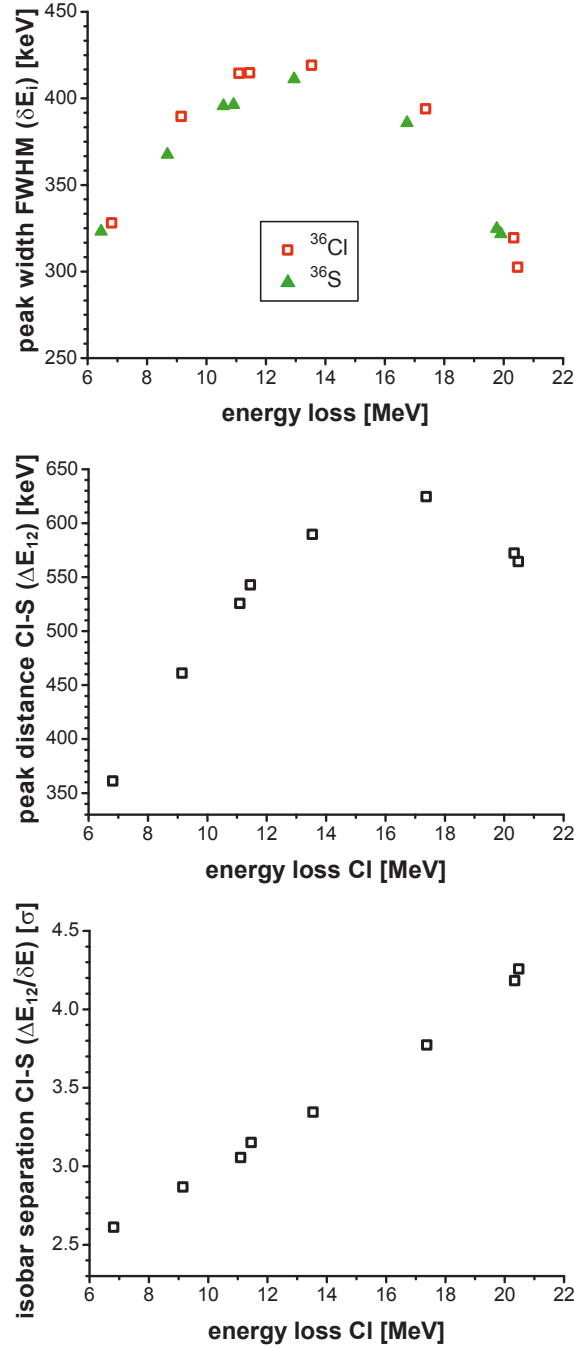


Figure 3.8: Isobar separation of ^{36}Cl and ^{36}S at 23.4 MeV initial energy in isobutane. The peak widths (δE_i), the distance between the two peaks (ΔE_{12}) and the isobar separation $\Delta E_{12}/\delta E$ (with $\delta E = \sqrt{\delta E_1^2 + \delta E_2^2}$) are plotted as functions of energy loss. Below the maximum of the Bragg curve, the energy focussing effect at high energy losses leads to an increase in isobar separation even after the crossing point of the energy loss curves at ~ 16 MeV energy loss. The best separation is achieved at almost full energy loss.

loss in the past sections experience a different stopping power in the coming section that partly compensates for the deviation, i.e. ions with more residual energy have a higher stopping power. Therefore it becomes advantageous for isobar separation to measure up to almost the full energy loss, despite that the distance of the peaks in the total energy loss spectrum ΔE_{12} will thereby decrease significantly. This is more than compensated for by the strong decrease in peak widths δE_i . At very high energy losses, nuclear stopping starts to contribute significantly to the energy straggling and prevents further energy focussing. Additionally, the contribution of the detector gas sets a lower limit for the peak widths. In the case of ^{36}Cl and ^{36}S the best separation is achieved at an energy loss in the ionization chamber of $\sim 5/6$ of the initial energy. Since the ion of interest has an atomic number higher than its isobar, energy tails in the spectrum, that arise at almost full energy loss, can deteriorate the separation. Their influence and how to suppress them is discussed in the next sections. The information from the individual anodes of course gives additional information, but the isobars are best separated in the total energy loss signal from the ionization chamber ($\Delta E_1 + \Delta E_2$), as shown also later in table 3.7.

Figure 3.8 shows our experimental results for δE_i and ΔE_{12} of ^{36}S and ^{36}Cl at an initial energy of 23.4 MeV (3 MV terminal voltage) as a function of energy loss obtained with isobutane as detector gas. Below the Bragg maximum, the strong decrease in energy straggling at high energy losses more than compensates for the decrease in distance of peaks after the crossing point of the energy loss curves and the isobar separation still increases. The highest isobar separation is achieved at almost full energy loss. This allows reasonable isobar suppression factors already at relatively low initial energies.

3.3.4 Sulfur suppression

The definition of isobar separation according to equation 3.8 is based on the ideal case of Gaussian-shaped peaks. Tails in the energy loss spectra from scattered particles of the interfering isobar usually reduce the actual separation and the achievable sulfur suppression is overestimated by equation 3.8. Figure 3.9 shows spectra of the total energy loss in the ionization chamber ($\Delta E_1 + \Delta E_2$) recorded on a reference material with a $^{36}\text{Cl}/\text{Cl}$ ratio of 10^{-11} and a blank sample without ^{36}Cl . It is obvious that the high energy tail of ^{36}S reaching into the ^{36}Cl region of interest limits the sulfur suppression and thus determines the sensitivity for ^{36}Cl for samples with a low $^{36}\text{Cl}/\text{Cl}$ ratio. Therefore, the sulfur suppression factor, which is a crucial parameter of the detection setup, has to be determined experimentally with a ^{36}S beam according to:

$$^{36}\text{S suppression} = \frac{N_{^{36}\text{S total}}}{N_{^{36}\text{S bin}}} \cdot \text{eff}(^{36}\text{Cl}) \quad (3.14)$$

$N_{^{36}\text{S total}}$ is the total number of ^{36}S events and $N_{^{36}\text{S bin}}$ the number of ^{36}S events ending up in the ^{36}Cl region of interest. These events are usually misinterpreted as

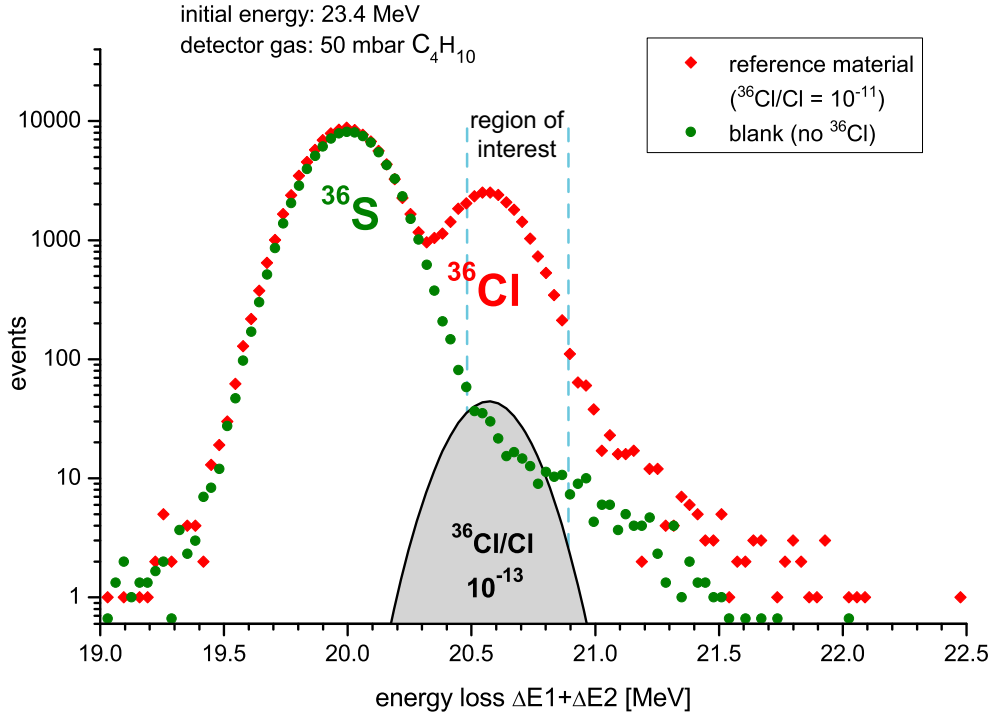


Figure 3.9: Total energy loss spectra from a reference material ($^{36}\text{Cl}/\text{Cl} \approx 10^{-11}$, red) and a stainless steel target (^{36}Cl blank, green) recorded with the ionization chamber filled with 50 mbar isobutane. The black curve shows the calculated ^{36}Cl signal from a sample with a $^{36}\text{Cl}/\text{Cl}$ ratio of 10^{-13} . The high energy tail from the ^{36}S peak reaches far into the ^{36}Cl region of interest and almost covers the ^{36}Cl signal expected from the low sample. This tail is the main limitation for sulfur suppression.

^{36}Cl and are the major contribution to background in ^{36}Cl measurements. $\text{eff}(^{36}\text{Cl})$ is the efficiency of the detection setup for ^{36}Cl including losses due to a tight ^{36}Cl region of interest. Details on how the ^{36}Cl region of interest is determined are given in section 5.4.1. Using the total energy loss spectrum shown in figure 3.9, the theoretical sulfur suppression based on the separation of peaks determined according to equation 3.8 is 20 000. The experimental sulfur suppression, however, is only 2 400, despite additional conditions set on the individual energy loss signals from the anodes. This underlines the large interference of scattering tails and the need for an experimental determination of sulfur suppression factors.

Measurement of the sulfur suppression requires a ^{36}Cl -free ^{36}S beam, so possible cross contamination in the ion source has to be avoided. This is either achieved with sulfur rich samples like stainless steel and the use of a beam attenuator or with special AgCl samples enriched with sulfur at the ppm-level (see section 5.1 for details on those samples). Unfortunately, both methods have their drawbacks. The beam attenuator is a perforated steel shield, which, from our experience, significantly

cuts the phase space of the beam. While this might result in an overestimation of sulfur suppression, the method is very robust against cross contamination in the source. On the other hand, the spiked AgCl samples have the same phase space as true samples but are prone to contamination. Any contamination will result in an underestimation of sulfur suppression due to real ^{36}Cl events in the spectra. These samples are therefore measured before any material with high $^{36}\text{Cl}/\text{Cl}$ ratio is sputtered. In most measurements, the sulfur suppression was determined by both methods. Special care is taken to adjust the ^{36}S count rate to typical values for AgCl from natural samples (~ 1 kHz) in order to have similar conditions in the ionization chamber. Significantly higher ^{36}S count rates could disturb the determination of the suppression factor due to changes in detector resolution and the number of pile-up events. A precise determination of a sulfur suppression factor of $\sim 10^4$ requires recording of several million ^{36}S events and thus quite long acquisition time.

| facility | terminal voltage [MV] | particle energy [MeV] | eff(^{36}Cl) [%] | ^{36}S suppr. | Ref. |
|----------|--------------------------|--------------------------|--------------------------------|------------------------|------|
| VERA | 3.0 | 24.0 | 50 | 2 400 | |
| VERA | 3.3 | 26.4 | 50 | 9 000 | |
| VERA | 3.5 | 28.0 | 50 | 30 000 | [58] |
| ETH | 0.5 | 3.0 | | 5 – 10 | [96] |
| SUERC | 5.0 | 30.0 | 45 | 100 000 | [98] |
| ETH | 6.0 | 48.0 | 75 | 170 000 | [80] |
| ANU | 14.0 | 112.0 | 100 | 3 000 000 | [99] |

Table 3.2: Sulfur suppression factors for different particle energies. The values for VERA were determined with the ionization chamber alone and isobutane as detector gas. The other values were obtained with optimized ionization chambers and are just given for comparison. The corresponding ^{36}Cl detector efficiencies are also stated where known.

The strong dependence of the sulfur suppression on the available particle energy is summarized in table 3.2. The values for VERA were determined with the ionization chamber alone. Operation of VERA above the nominal value of 3 MV is not suitable for routine measurements since it requires extensive conditioning time and is only possible in a certain period after maintenance. Suppression values from other facilities at various energies are just given for comparison. It's obvious that high particle energies favor isobar separation, hence decent sulfur suppression is almost impossible at particle energies of ~ 3 MeV. Due to the remaining sulfur content of chemically cleaned AgCl samples, a sulfur suppression of at least 10 000 is required to achieve a background level of $^{36}\text{Cl}/\text{Cl}$ in the low 10^{-15} range. Our technique to boost the sulfur suppression by identifying and rejecting events, which create the high energy tails in the energy loss spectra, is discussed in the next section.

| ^{36}Cl detector efficiency | ^{36}S suppression |
|--------------------------------------|-----------------------------|
| 60 % | 2 000 |
| 50 % | 11 000 |
| 40 % | 30 000 |
| 30 % | 55 000 |

Table 3.3: Sulfur suppression factors of the entire detection setup for different ^{36}Cl detector efficiencies obtained with isobutane as detector gas and 24 MeV initial particle energy.

An easy method to increase the sulfur suppression is of course the choice of a tighter ^{36}Cl region of interest. Table 3.3 lists experimental sulfur suppression values of our detection setup (including the enhancement by the silicon strip detector) for different ^{36}Cl detector efficiencies with isobutane as detector gas and 24 MeV initial particle energy. A tight ^{36}Cl region of interest significantly reduces the interference from ^{36}S . On the other hand, a high ^{36}Cl efficiency is desirable to reduce uncertainties from statistics for samples with low amounts of ^{36}Cl . For reasons of better comparison, all further sulfur suppression values in this work are given for 50 % ^{36}Cl detector efficiency unless explicitly stated otherwise.

3.3.5 Enhanced suppression with the silicon strip detector

At 24 MeV initial particle energy, the sulfur suppression factor of $\sim 2\,400$ with the ionization chamber alone is too low for the measurement of natural ^{36}Cl samples. Evaluation of the performance of various detection systems [61] revealed that the addition of a silicon strip detector behind the exit window of the ionization chamber improves the sulfur suppression by a factor of 5 at constant ^{36}Cl detector efficiency.

The strong enhancement in sulfur suppression is not, as initially suspected, mainly because of isobar separation in the residual energy signal, which in fact is rather poor due to the exit window of the ionization chamber and the 100 nm Al window of the strip detector (see section 3.5.2). The large improvement comes from the fact that the exit window efficiently blocks scattered ions, which cause the high energy tails in the spectra of the ionization chamber. As scattered ions have a longer flight path through the gas volume and subsequently deposit more of their kinetic energy and also the recoil particles lead to additional ionization, some scattered ^{36}S ions end up in the ^{36}Cl region of interest. However, ions with inclined flight paths usually do not pass the exit window aperture of the ionization chamber and are rejected by accepting only events that produce a signal in the silicon strip detector.

A comparison of the total energy loss spectra from the ionization chamber with and without the condition of a coincident signal from the silicon strip detector is shown in figure 3.10. Rejection of ions, which do not reach the strip detector, completely suppresses the tail of sulfur reaching into the area of the ^{36}Cl peak. Thereby, the

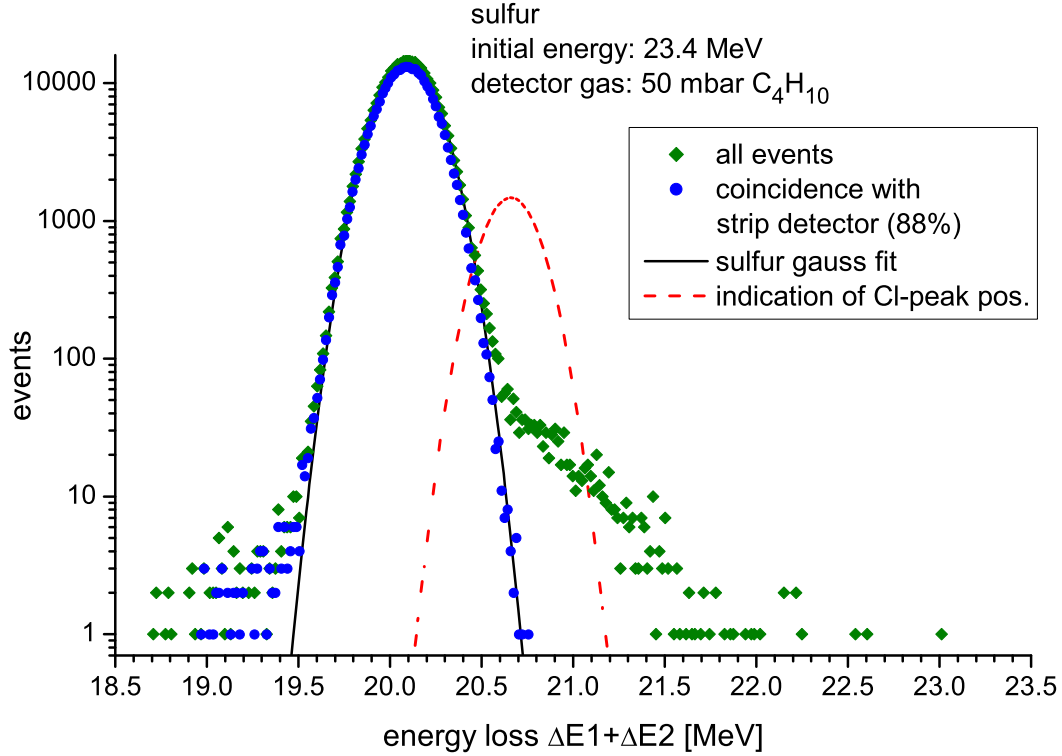


Figure 3.10: Energy loss spectra of ^{36}S from the ionization chamber with isobutane. The high energy tail present when all events are recorded (green) is completely suppressed by accepting only events that produce a signal in the silicon strip detector (blue). The black curve is a Gaussian fit of the sulfur peak, the dotted red curve indicates the position of the ^{36}Cl peak. Rejection of particles that do not pass the exit window results in Gaussian shaped peaks over several orders of magnitude without any high energy tails. It's obvious that the number of ^{36}S ions in the ^{36}Cl region of interest is substantially reduced by this method at only 12 % loss of ^{36}Cl .

number of ^{36}S events misinterpreted as ^{36}Cl is reduced by at least a factor of 4. The resulting peaks in the spectra are Gaussian-shaped over 4 orders of magnitude. In the case of isobutane, 88 % of all ions pass through to the strip detector at the optimal pressure of 50 mbar. The rather small transmissional loss of 12 % is compensated for by a less tight ^{36}Cl region of interest to achieve 50 % ^{36}Cl detector efficiency. This loss is comparable to the losses introduced by gating with a 2D-sensitive ionization chamber to achieve similar suppression of scattering tails [80].

New results obtained with the upgraded detection system compared to the ionization chamber alone are plotted in figure 3.11. With a sulfur suppression factor above 10 000, our detection setup provides sufficient isobar separation for measurements of environmental ^{36}Cl samples at 3 MV terminal voltage. Also at 3.3 MV terminal voltage a significant increase in sulfur suppression is observed.

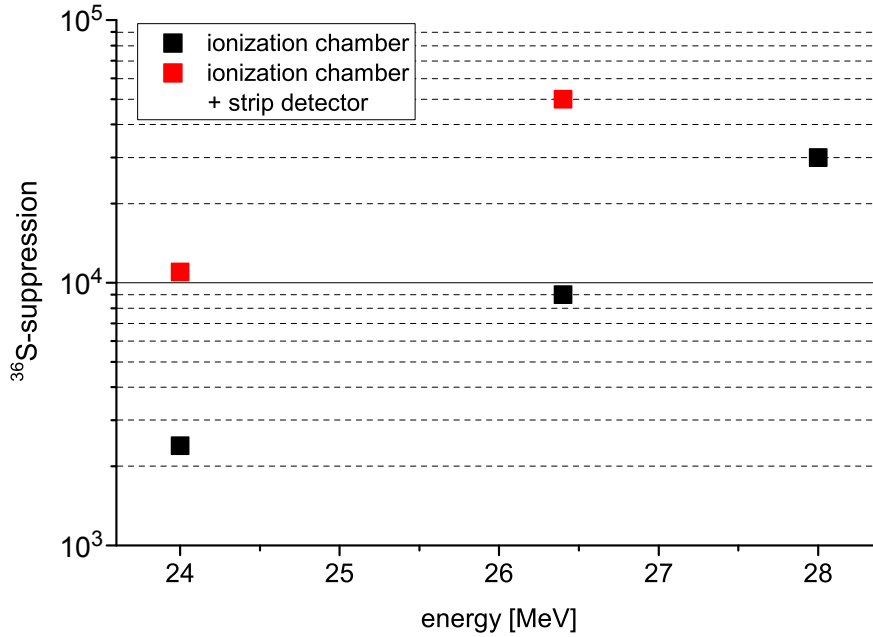


Figure 3.11: Sulfur suppression factors of the upgraded detection system (red) and the ionization chamber alone (black) as a function of energy. The detector gas was isobutane and the ^{36}Cl detector efficiency was 50 % for both detection setups, including transmissional losses within the setup. The silicon strip detector improves the sulfur suppression at 24 MeV by at least a factor of 4.

3.3.6 Comparison with simulations

A suitable computer program for the optimization of the detection setup is very desirable and there exist several codes to simulate energy loss and energy straggling of ions in matter. However, calculation of isobar separation based on the results of those simulation codes turns out to be difficult and in most cases inaccurate. Assuming Gaussian shaped peaks in the energy loss spectra, a 10% deviation of either the energy straggling or the difference in energy loss from the true values results in a change in theoretical sulfur suppression by a factor of 4–6. Therefore it is essential to verify these theoretical results in experiments. In fact, some effects are astonishingly well reproduced, but also significant discrepancies are observed.

A widely used computer code is the program SRIM [69]. Its shortcomings in prediction of energy straggling have already been discussed in section 3.3.2 for the case of silicon nitride. The situation for straggling values based on electronic stopping in gases is much the same. But also the calculation of a mean energy loss is problematic. While the total energy loss of a specific nuclide is satisfyingly accurate, the calculated difference in energy loss between two isobars deviates surprisingly much from measured values.

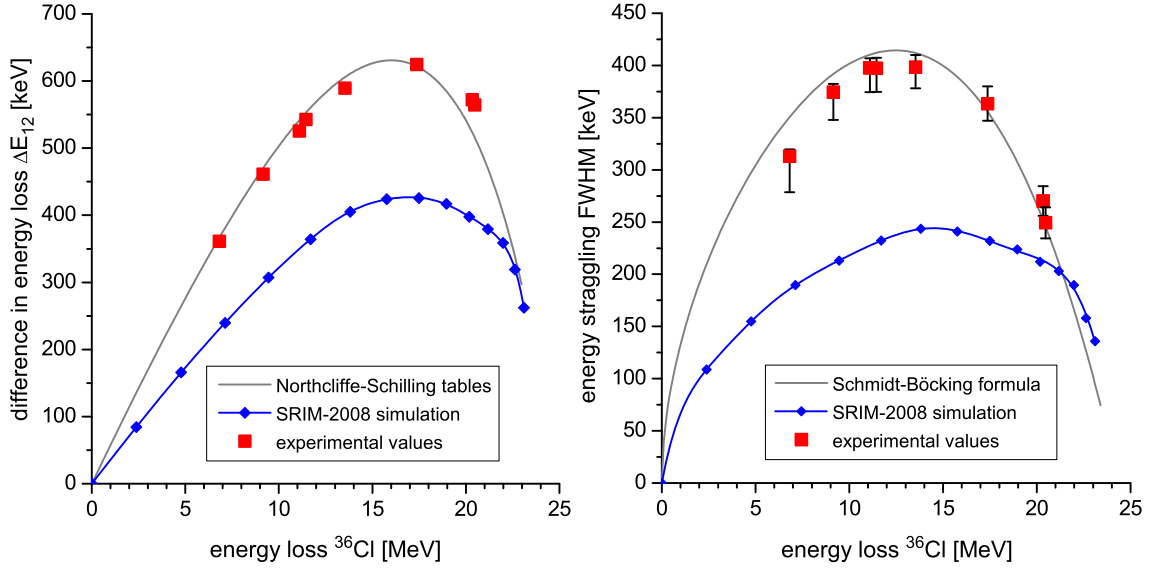


Figure 3.12: Comparison of experimental and theoretical energy loss and energy straggling values for ^{36}Cl in isobutane with an initial energy of 24 MeV. The left graph shows the difference in energy loss between ^{36}Cl and ^{36}S , the right the energy straggling of ^{36}Cl . Values obtained from a simulation with SRIM-2008 [69] (blue) are almost a factor of 2 away from experimental results (red) in both cases. Calculations based on the stopping power tables by Northcliffe and Schilling [100] and the straggling formula from Schmidt-Böcking and Hornung [77] (see equation 3.7) yield more accurate results (gray). The uncertainties of the measured data due to the energy calibration are smaller than the plotted symbols. The uncertainties of the straggling values stem mainly from the correction of the detector gas contribution.

Experimental values and results from SRIM and other calculations are shown in figure 3.12. They were obtained with isobutane as detector gas and ^{36}Cl with an initial energy of 24 MeV before the entrance window. The straggling values were derived from the measured peak widths by correction of all other factors contributing to the detector resolution according to equation 3.10. For this purpose, the contribution of the detector gas itself was assumed to be a constant fraction of 0.7 % of the signal for energy losses of 5–22 MeV (compare section 3.3.2). This estimation bears significant uncertainties, which are reflected in the final experimental straggling values.

The large discrepancy of up to 50 % between measured values and the SRIM simulation makes a reliable estimation of theoretical sulfur suppression values almost impossible. A calculation of the difference in energy loss between ^{36}Cl and ^{36}S based on the stopping power data tables of Northcliffe and Schilling [100] gives a far better estimate. Concerning energy straggling, significantly more accurate results than with SRIM are obtained with the semi-empirical formula for Cl in isobutane (equation 3.7) by Schmidt-Böcking and Hornung [77] using again the stopping power data from

Northcliffe and Schilling. Despite the fact that the formula is valid for electronic stopping only, a good agreement is observed for high energy losses indicating little influence of nuclear stopping. Interestingly, there is a small discrepancy to the experimental values at lower energy losses. An explanation could be that the shape of the stopping power curves of Northcliffe and Schilling, which is used in the calculation of straggling, possibly is slightly inaccurate. A small correction based on their experimental results was already suggested by Schmidt-Böcking and Hornung [77]. The accuracy of the energy calibration for the experimental ^{36}Cl data is estimated to be 1,5 % for small energy losses and a maximum of ~ 200 keV for energy losses around 20 MeV (see section 3.4.1 for details). The resulting uncertainty can not account for the deviation and is smaller than the plotted symbols.

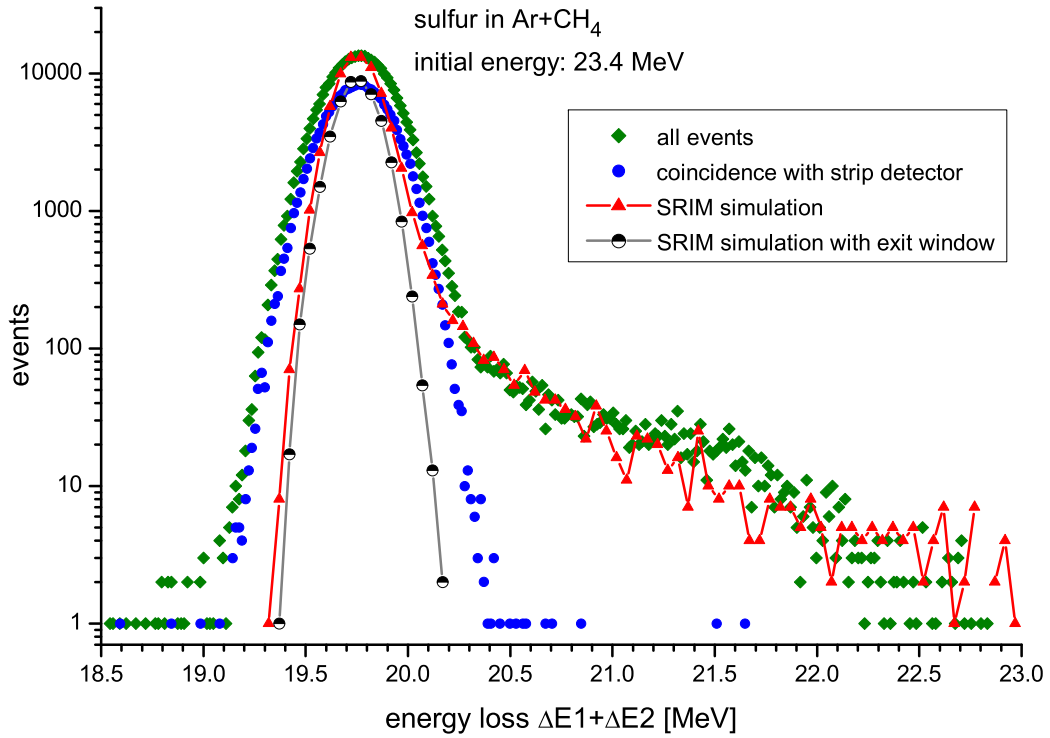


Figure 3.13: Comparison of experimental total energy loss spectra from the ionization chamber (green and blue symbols) with a SRIM simulation (red and black line). The detector gas was 150 mbar argon+10% methane, which has a higher nuclear stopping than isobutane. Note that the energy tails, which are caused by scattering events (nuclear stopping), are well reproduced in the SRIM simulation. The central part of the peak, which can be well described with a normal distribution, is predominantly caused by straggling of the electronic stopping process, which is underestimated in the simulation like for isobutane. The initial energy of 23.4 MeV instead of 24 MeV already compensates for the energy loss in the entrance window. Rejection of events, which do not pass an aperture of the same size as the exit window, also completely suppresses the high energy tails in the simulation.

In contrast, angular scattering in the ionization chamber and the resulting tails in the energy loss spectra can be very well simulated by SRIM. Figure 3.13 shows a comparison of a SRIM simulation and experimental values with argon+10% methane as detector gas, which has a higher nuclear stopping than isobutane. Both the onset as well as the width of the high energy tail caused by angular scattering are in good agreement with the experimental data. Furthermore, also the suppression of scattering tails by the detection setup can be reproduced using the TRANSMIT-files generated by SRIM and rejecting events, which do not fulfill the conditions set by the exit window. A variation of the size of the exit window aperture in the simulation proved that already a window with a sidelength of 7 mm instead of 5 mm would deteriorate the separation significantly. This approach was therefore no longer pursued.

Summarizing, a complete simulation of isobar suppression in the detection setup is very difficult and a lot of experimental data is needed to check or scale the theoretical results. Additionally, there are several effects such as the pulse height deficit, losses in charge collection or pile-up tails that are not considered in the simulations.

3.4 Comparison of detector gases

Due to the strong dependence of sulfur suppression on the energy straggling in gases and the shape of the respective stopping power curves, a study of the properties of various counter gases was performed. This was initially motivated by the finding that argon-methane as detector gas has $\sim 10\%$ lower energy straggling than isobutane [77]. Since simulations proved unreliable as shown before, experimental data was necessary and three detector gases were studied: isobutane (C_4H_{10}), argon+10% methane ($Ar+CH_4$) and isobutane+30% argon ($C_4H_{10}+Ar$). While the first two were commercially available, the latter was mixed at our lab with the percentage of argon being accurate to $\pm 5\%$. The results for energy straggling and the sulfur suppression factors are presented in the following sections.

3.4.1 Energy calibration

For a comparison of straggling results, the energy loss signals from the detection setup had to be calibrated for each of the three counter gases. First, the electronics was adjusted such that both energy loss signals of the ionization chamber (ΔE_1 and ΔE_2) have the same calibration. For this purpose, a pulse generator was connected to the test input line of the preamplifiers. The gain of the main amplifiers was then fine-tuned for the same pulse height in the recorded spectra. Significant differences in charge collection efficiency or in the response of the preamplifiers between the two anodes were ruled out by rotating the ionization chamber by 180° during test measurements.

The setup was then calibrated by recording the energy loss spectra of ^{36}S and ^{36}Cl with initial energies of 24.0 MeV and 26.4 MeV at different gas pressures. At lower gas pressures, only part of the energy is deposited within the gas volume and the residual energy is measured with the silicon strip detector. The silicon strip detector was calibrated by retracting the ionization chamber and directing an attenuated ^{36}S beam directly into the detector. A precise determination of the energy deposited within the gas volume also requires knowledge of the influence of any dead layers, i.e. detector windows. The energy loss in the entrance and exit window of the ionization chamber and in the Al-window of the silicon strip detector was therefore calculated with SRIM [69] for various energies. The results for ^{36}Cl and ^{36}S are given in table 3.4. Regarding the energy loss in thin SiN-foils, good agreement between the results from SRIM and experimental values has been shown by Sun et al. [87]. Nevertheless an uncertainty of 25 % for the energy loss was assumed since discrepancies between the actual thickness of the foil and the nominal value have been observed [86].

| E_0 [MeV] | 100 nm SiN window | | 100 nm Al window | |
|----------------|--------------------------------------|-------------------------------------|--------------------------------------|-------------------------------------|
| | ΔE ^{36}Cl [keV] | ΔE ^{36}S [keV] | ΔE ^{36}Cl [keV] | ΔE ^{36}S [keV] |
| 26.4 | 602 | 580 | 455 | 438 |
| 24.0 | 595 | 573 | 449 | 433 |
| 10.0 | 491 | 476 | 371 | 359 |
| 5.0 | 357 | 341 | 289 | 275 |
| 4.0 | 317 | 302 | 262 | 248 |
| 3.0 | 271 | 255 | 230 | 217 |
| 2.0 | 218 | 203 | 189 | 174 |
| 1.0 | 146 | 138 | 127 | 119 |

Table 3.4: Energy losses in the detector windows for ^{36}Cl and ^{36}S at various energies calculated by SRIM [69].

In a second approach, the calibration was determined by ensuring full stopping in the gas. For this purpose, the gas pressure was increased until the sum of the energy loss signals ($\Delta E_1 + \Delta E_2$) reached a plateau indicating full energy loss within the ionization chamber. An example is shown in figure 3.14. This plateau continues until the high gas pressure reduces the drift velocity to an extent that recombination of ionization charges starts to play a role. For isobutane and isobutane+30% argon, the standard window could withstand the gas pressure required for full stopping of the ions, which was 85 mbar and 135 mbar respectively. Due to the low stopping power of argon+10% methane, full stopping of the ions only sets in around a pressure of 250 mbar, which requires the use of a special $1 \times 1 \text{ mm}^2$ window. Unfortunately, charge collection already seems to be hampered at this pressure. The measured

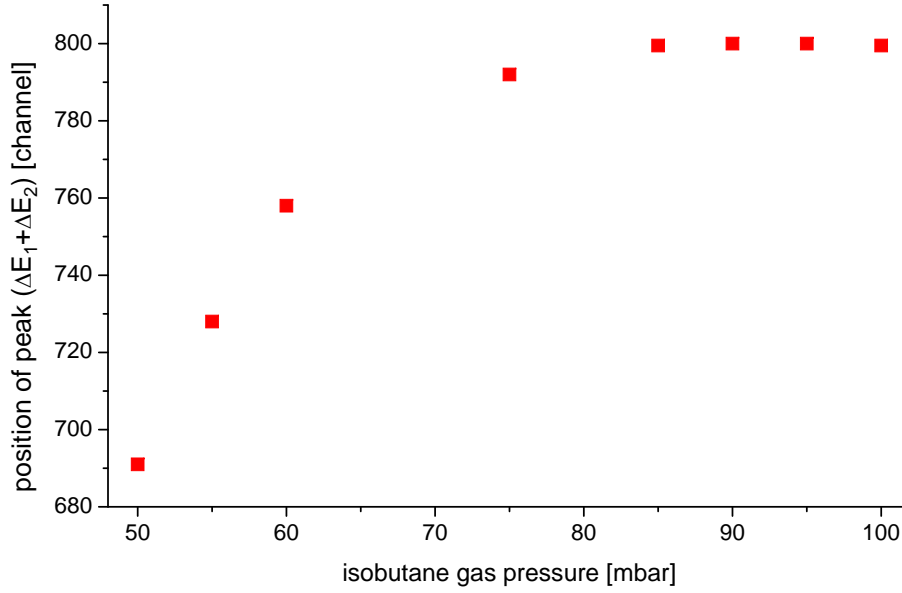


Figure 3.14: Position of the peak in the total energy loss spectra from the ionization chamber as a function of detector gas pressure recorded with 26.4 MeV ^{36}S and isobutane. Above a pressure of 85 mbar, the energy loss no longer increases with gas pressure indicating full stopping of the ions within the gas volume. At very high pressure, the collected charge will decrease again due to recombination.

energy loss decreases immediately by any further increase in pressure and no plateau is formed. For this reason, the calibration for argon+10% methane is based only on the differential energy loss measurements at lower pressures.

The final calibration values for ^{36}S from energy losses of 15–26 MeV are summarized in table 3.5. Isobutane as detector gas gives a slightly smaller signal compared to the other two gases. The overall uncertainties of the calibrations are 1.4–1.7 %.

| detector | gas | calibration [keV/channel] |
|--------------------|---------------------------------------|------------------------------|
| ionization chamber | C_4H_{10} | 32.21 ± 0.47 |
| ionization chamber | $\text{Ar} + \text{CH}_4$ | 30.95 ± 0.53 |
| ionization chamber | $\text{C}_4\text{H}_{10} + \text{Ar}$ | 31.05 ± 0.45 |
| silicon strip | — | 15.20 ± 0.10 |

Table 3.5: Energy calibration of the detection setup with ^{36}S for various detector gases based on energy losses of 15–26 MeV. The stated uncertainties are the total uncertainties of the calibration, the relative uncertainties between different calibrations are significantly smaller ($\sim 3\%$).

Since the sources of the uncertainties like the actual energy loss in the windows are the same for all gases, the relative uncertainty between various calibrations is only around 3 ‰. Scaling factors between different gases are accurately obtained by adjusting the pressure for the same residual energy signal from the silicon strip detector. Calibration values for ^{36}Cl are 5 ‰ higher than for ^{36}S due to a slightly larger pulse height deficit. This deviation is still within the total uncertainties of the calibration, therefore the calculation of the peak distance for isobar separation is based only on the ^{36}S -calibration.

3.4.2 Measurement of peak widths in various detector gases

The peak widths of ^{36}S and ^{36}Cl were measured by recording the energy loss spectra from the ionization chamber at various gas pressures. The experimental peak widths in the spectra were corrected according to equation 3.10 to obtain the energy straggling and the influence of the respective detector gas. The contributions to the detector resolution from the beam, the entrance window and the electronics quadratically add up to $\sim 85\text{ keV}$, the inefficiency of shielding causes an additional broadening by 0.3 % of the energy loss signal (cf. section 3.3.2). With measured peak widths around 350 keV, the resulting correction is only 4.5 %. Consequently, the uncertainties in the determination of the correction like the true thickness of the windows are almost negligible. The main uncertainty of the absolute values for the gas contribution comes from the energy calibration. In order to minimize the influence of angular scattering tails, only events, which produced a signal in the silicon strip detector and thus passed the exit window, were accepted. The corrected peak widths of 23.4 MeV ^{36}S in the three detector gases as a function of energy loss are shown in figure 3.15. Experiments at 25.8 MeV yielded similar results.

Up to energy losses of $\sim 15\text{ MeV}$, argon+10% methane as detector gas gives $\sim 10\text{--}15\%$ lower peak widths and better peak separation compared to isobutane. Simulations of energy straggling based on the straggling formula given in [77] (equation 3.7) using the energy loss data from Northcliffe and Schilling [100] reproduce this trend. For large energy losses ($E > 15\text{ MeV}$), however, the experimental data with argon-methane deviate from simulations (see figure 3.16) and, above 20 MeV, lead to a higher peak width than with isobutane. Experimental values for the detector resolution at total energy loss suggest that the contributions of the respective gases themselves are roughly the same ($\sim 170\text{ keV}$) and no higher values for argon+10% methane were observed. A reason for the discrepancy between theoretical and experimental straggling results with argon+10% methane might be that argon has a higher nuclear stopping, which increases the energy straggling at lower residual energies (this effect is not considered in the simulations). Unfortunately, this is difficult to verify since a correction of the influence of the gas itself in order to obtain the energy straggling is difficult and bears a lot of uncertainties (see discussion in section 3.3.6). As a consequence of increased peak widths with argon-methane, the measured energy focussing

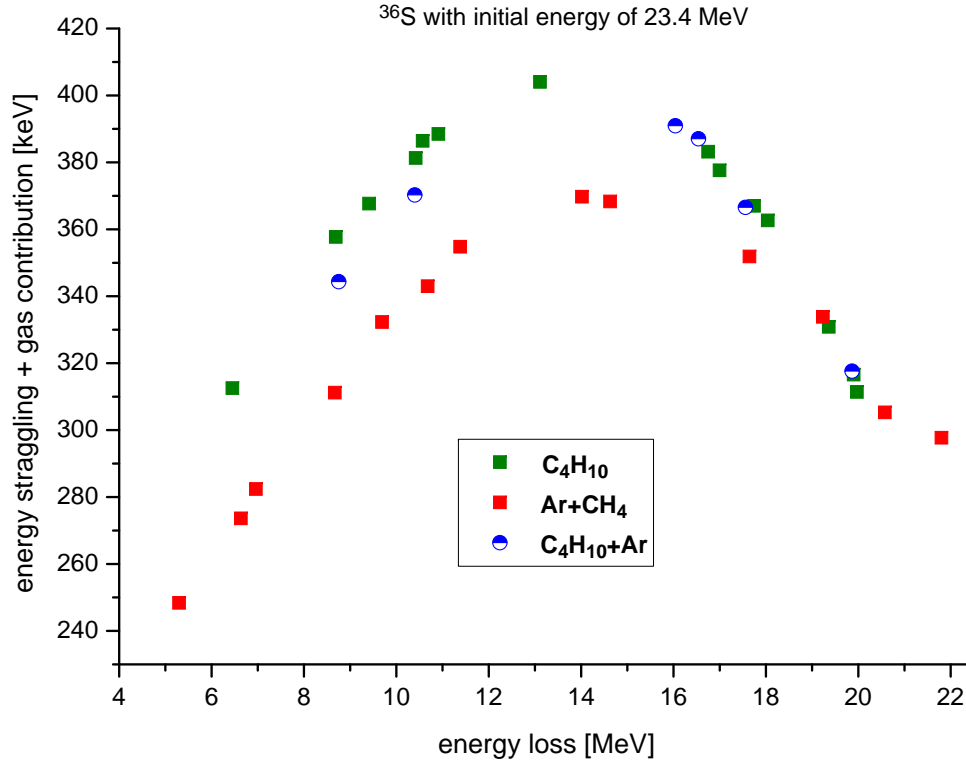


Figure 3.15: Corrected peak widths from the energy loss spectra of ^{36}S in isobutane (green), argon+10% methane (red) and isobutane+30% argon (blue) as a function of energy loss. These widths comprise the energy straggling and the contribution from the detector gas. The initial energy of 23.4 MeV already compensates for the energy loss in the entrance window. The absolute uncertainties due to the calibrations are not plotted here, the relative uncertainties between different gases are smaller than the plotted symbols.

effect is stronger in isobutane. Results with isobutane+30% argon lie between the other two gases. At smaller energy losses, the peak width is $\sim 4\%$ lower than with isobutane and almost identical to isobutane above 16 MeV energy loss.

The peak widths with argon+10% methane were further investigated using a small detector window of $1 \times 1 \text{ mm}^2$ size instead of the standard window with 5 mm side length. With a tighter exit window aperture, the influence of angular scattering in the gas volume caused by nuclear stopping should be further reduced. Results in figure 3.16 show that only at the highest energy loss of almost 22 MeV a reduction in energy straggling is observed. Particles scattered to larger angles in the gas can therefore not account for the increased straggling above energy losses of 12 MeV. Also the uncertainty of the energy calibration and the contribution of the detector gas is smaller than the deviation from theoretical straggling results. It is more likely that small angle scattering and the secondary ionization charges produced by the recoils in nuclear stopping are the causes for the increased energy straggling.

Summarizing, at around 20 MeV energy loss (5/6 of the initial energy), where the highest sulfur suppression factors are usually achieved with the detection setup, all three gases have about the same contribution to the energy resolution of ~ 310 keV. Assuming almost equal distance of ^{36}S and ^{36}Cl peaks in various detector gases, one should expect higher sulfur suppression factors with argon+10% methane and also isobutane+30% argon due to smaller peak widths in the ΔE_1 signal, where the energy loss is around 12 MeV.

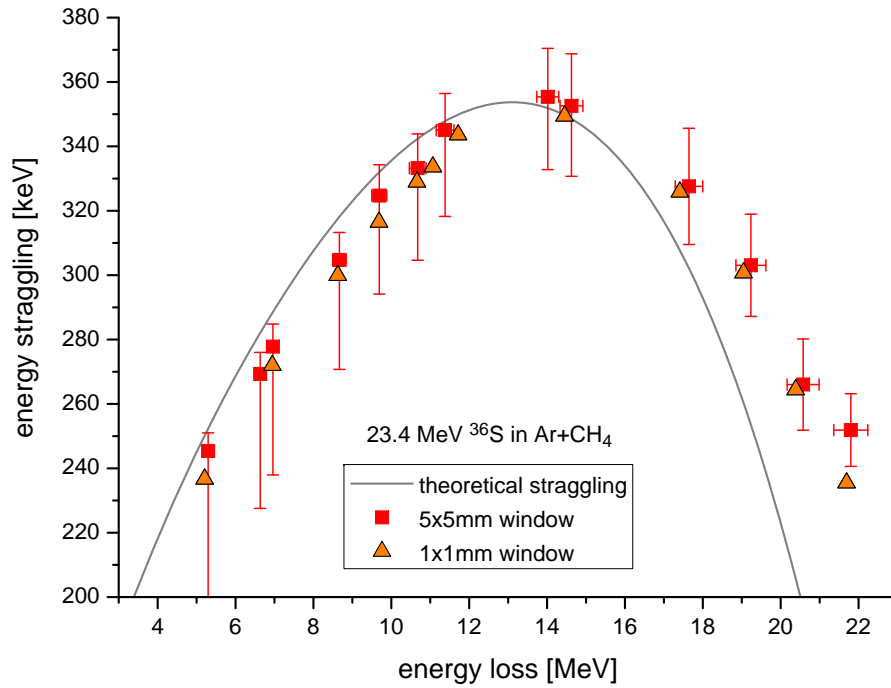


Figure 3.16: Energy straggling of 23.4 MeV ^{36}S in argon+10% methane as a function of energy loss measured with different detector window sizes. Experimental results with a small window of $1 \times 1 \text{ mm}^2$ size (orange) are similar to those obtained with the standard window ($5 \times 5 \text{ mm}^2$, red). At large energy losses, both are significantly higher than theoretical results based on the semi-empirical formula by Schmidt-Böcking and Hornung [77] and the stopping power data from Northcliffe and Schilling [100], which is probably due to nuclear stopping. This deviation can not be reduced by a tighter exit window aperture. A small contribution to straggling from scattered particles is only observed at the highest energy loss. The error bars of the standard window data indicate the absolute uncertainty of the experimental data due to the correction of the gas contribution and the absolute energy calibration. The relative uncertainty between the two data sets is smaller than the plotted symbols.

3.4.3 Energy loss spectra and sulfur suppression factors

Besides energy straggling and the gas contribution to the detector resolution, also the other properties of the detector gases, which are relevant for isobar separation, were investigated. For each gas, energy loss spectra were recorded both on ^{36}Cl -blank materials containing only ^{36}S and reference materials with a high $^{36}\text{Cl}/\text{Cl}$ ratio of 10^{-11} to obtain a distinct ^{36}Cl peak. Results for the distance of ^{36}Cl and ^{36}S peaks as well as the theoretical separation are plotted in figure 3.17. Surprisingly, the distance of peaks in the energy loss spectra (ΔE_{12}) is highest for argon+10% methane. This can not be deduced from the stopping power curves by Northcliffe and Schilling [100], which predict a slightly higher distance for isobutane. Since all gases have roughly the same contribution to the peak widths at 20 MeV, argon+10% methane provides the best theoretical sulfur suppression assuming Gaussian shaped peaks (compare equation 3.8). Values for isobutane+30% argon are slightly better than for pure isobutane. For all three gases, the energy focussing effect discussed in section 3.3.3 leads to an increase in isobar separation after the maximum distance of peaks.

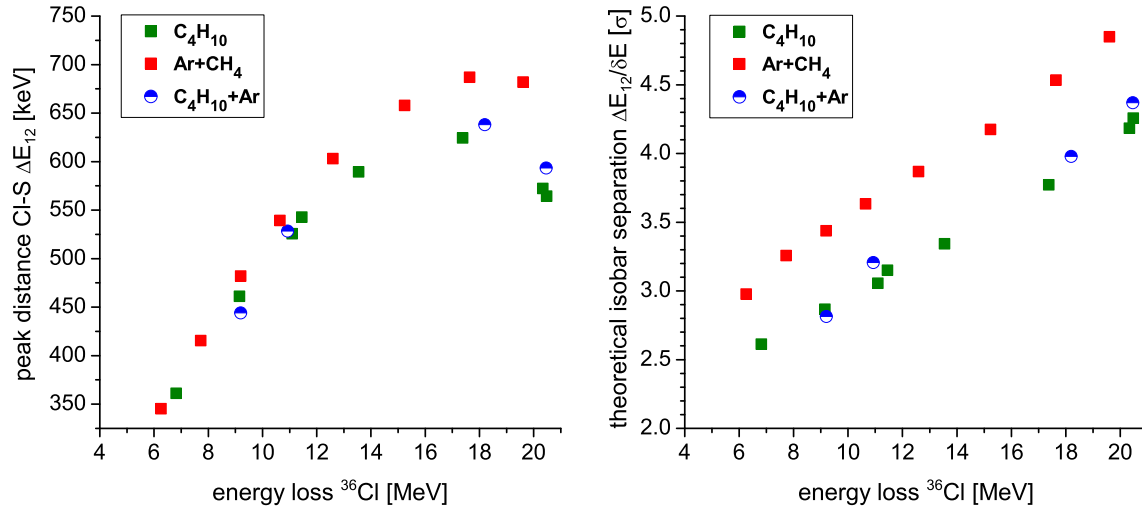


Figure 3.17: Distance and separation of ^{36}Cl and ^{36}S peaks with isobutane (green), argon+10% methane (red) and isobutane+30% argon (blue) as a function of energy loss. Based on these data, argon+10% methane should yield the highest sulfur suppression. The total uncertainty due to the calibration is not plotted, the relative uncertainty between different gases is smaller than the plotted symbols.

As shown before, the experimental sulfur suppression factors may differ significantly from the theoretical peak separation and are strongly influenced by the high energy tails in the spectrum due to angular scattering. Furthermore, transmissional losses in the detection setup have to be compensated for by setting a bigger region of interest on the individual signals in order to achieve similar ^{36}Cl detector efficiency. These effects partly reverse the above results.

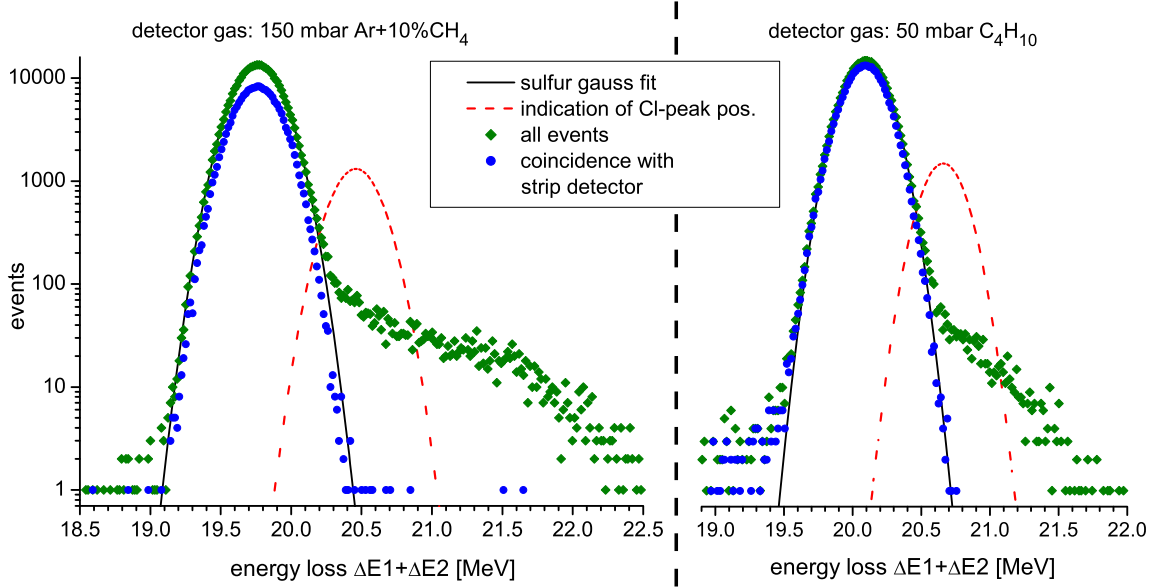


Figure 3.18: Comparison of total energy loss spectra from the ionization chamber obtained with argon+10% methane (left graph) and isobutane (right graph) as detector gas and 23.4 MeV ^{36}S . Due to the high pressure and the higher nuclear stopping of argon, the scattering tail in argon+10% methane is much more pronounced and more ions are blocked by the exit window at an energy loss of ~ 20 MeV. Suppression of the angular scattering tails by coincidence with the silicon strip detector works for both gases and the resulting peaks (blue dots) have a Gaussian shape (black line). The peak widths are almost identical and the distance to the ^{36}Cl -peak, indicated in red, is slightly higher for argon+10% methane. The position of the ^{36}Cl -peak was determined in separate measurements.

Figure 3.18 shows a comparison of total energy loss spectra from ^{36}S in the ionization chamber with argon+10% methane and isobutane as detector gas. Spectra from isobutane+30% argon are almost identical to isobutane. Due to the low stopping power of argon+10% methane, a pressure of 150 mbar is necessary for the same energy loss as in 50 mbar isobutane. Together with the relatively high atomic number of argon, angular scattering is much more pronounced than with isobutane and the scattering tail stretches over the whole ^{36}Cl region of interest. As for all gases, the tail is efficiently suppressed by the signal from the silicon strip detector, but the transmission through the exit window is only 59 % with argon-methane compared to 89 % with isobutane and 79 % with isobutane+30% argon. This allows to set significantly tighter ^{36}Cl regions of interest for isobutane and isobutane-argon than for argon-methane for the same ^{36}Cl detector efficiency. As a consequence, it is favorable for sulfur suppression with argon+10% methane to measure at a lower pressure of 130 mbar corresponding to 17 MeV energy loss. At this pressure, the peak separation $\Delta E_{12}/\delta E$ is slightly smaller but the transmission is 71 %.

| detector gas | optimal pressure [mbar] | energy loss ^{36}S ($\Delta E_1 + \Delta E_2$) [MeV] | transmission to strip detector [%] |
|---------------------------------------|-------------------------|---|------------------------------------|
| C_4H_{10} | 48 | 19.7 | 89 |
| $\text{Ar} + \text{CH}_4$ | 130 | 17.3 | 71 |
| $\text{C}_4\text{H}_{10} + \text{Ar}$ | 75 | 19.8 | 79 |

Table 3.6: Detector transmission and energy loss of ^{36}S for various detector gases at the pressure, which yielded the highest experimental sulfur suppression factors.

For all three gases, the experimental sulfur suppression factors were determined at different gas pressures. With increasing energy loss, both the separation of peaks but also angular scattering and transmissional losses increase. The optimum values for the respective gases are summarized in table 3.6. The corresponding experimental suppression factors with the three counter gases as functions of ^{36}Cl detector efficiency are shown in figure 3.19. Over a large efficiency range, the best results are obtained with 75 mbar isobutane+30%argon as detector gas. This gas has transmission values and scattering tails similar to isobutane but slightly better peak separation, not only in the total energy loss signal ($\Delta E_1 + \Delta E_2$) but also in the differential energy loss signal from the first anode (ΔE_1) due to lower straggling for energy losses of

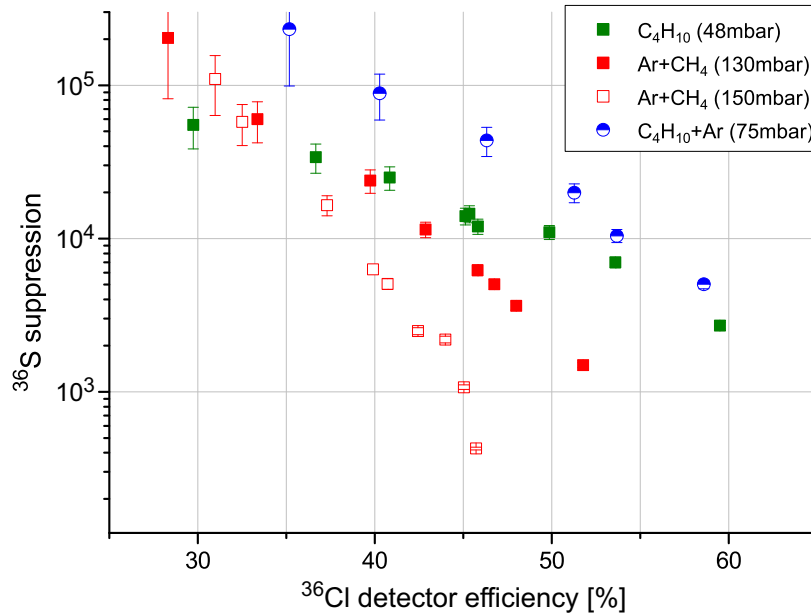


Figure 3.19: Sulfur suppression factors with isobutane, argon+10% methane and isobutane+30%argon as functions of the ^{36}Cl detector efficiency. The uncertainties stem from the statistical uncertainty of the number of ^{36}S ions in the ^{36}Cl region of interest.

~ 12 MeV. It yields a sulfur suppression of 20 000 at 50 % ^{36}Cl detector efficiency, which is roughly a factor of 2 higher than with isobutane. Argon-methane, for comparison, has a relatively low sulfur suppression factor of 3 000 at 50 % efficiency due to the high transmissional losses. The better peak separation (compare figure 3.17) results in a steeper increase of suppression towards lower efficiencies and below 40 % efficiency, argon+10% methane gives better suppression than isobutane.

Summarizing, isobutane+30% argon as detector gas is the best compromise between good energy loss properties and a high transmission through the detection system. It may very well be that a large study of other detection gases reveals even better gas mixtures, for our purpose, the sulfur suppression factors achieved with isobutane-argon were sufficiently high to allow measurements of ^{36}Cl at the nominal 3 MV terminal voltage.

3.5 Additional signals from the detection setup

Up to now, only the differential energy loss signals from the detection setup have been discussed but the setup also provides other information, such as the residual energy measurement and the position information from the silicon strip detector. Some of this additional information, like the pulse width measurement, are essential for the satisfying performance in ^{36}Cl measurements.

3.5.1 Pulse-width measurement for pile-up rejection

Apart from the two energy loss signals from the ionization chamber (ΔE_1 , ΔE_2) and the residual energy in the silicon strip detector (E_R), we also measure the pulse width of the ΔE_1 signal at 10 % of the signal height to reject disturbing pile-up events. For this purpose, the signal from the main amplifier is fed into a single channel analyzer (ORTEC model 550A) with the lower level voltage set to around 10 % of the signal height. The timing between the rising edge signal (LL out) and the falling edge signal (SCA out) is measured with a time-to-amplitude converter (cf. figure 5.2 for details on the electronics).

In order to mimic the pulse height of a ^{36}Cl event in Anode1, two sulfur atoms have to enter the detector with a certain time in between them such that the second signal still coincides with the tail of the first signal, as illustrated in figure 3.20. The resulting pulse has the same height as a ^{36}Cl event but a larger width at the 10 % level and is thus easy to identify by a pulse-width measurement.

Since the energy loss of ^{36}Cl and ^{36}S under Anode2 are almost equal, a pile-up of two sulfur ions can, in principle, also be identified by a higher than average signal from Anode2. However, if the two ^{36}S ions are scattered apart, the overlap of the two pulses is reduced due to a larger difference in drift time of charges to the Frisch grid and the signal from Anode2 may thus be compatible with a ^{36}Cl event. Additionally, one of

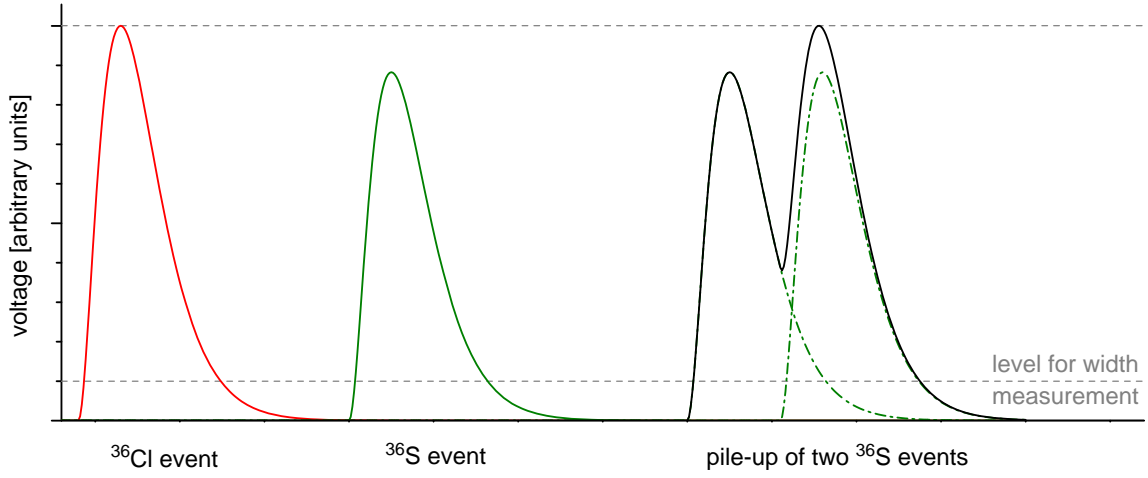


Figure 3.20: Illustration of ^{36}S pile-up mimicking a ^{36}Cl event in the ΔE_1 signal from the ionization chamber. While the signal from a single ^{36}S event (green) is smaller than that from a ^{36}Cl event (red), a pile-up from two ^{36}S ions (black) has the same peak height. However, the pulse width at the 10 % level is significantly different from a true ^{36}Cl event. The model for the signal shapes from the amplifier has been adopted from Michlmayr [101].

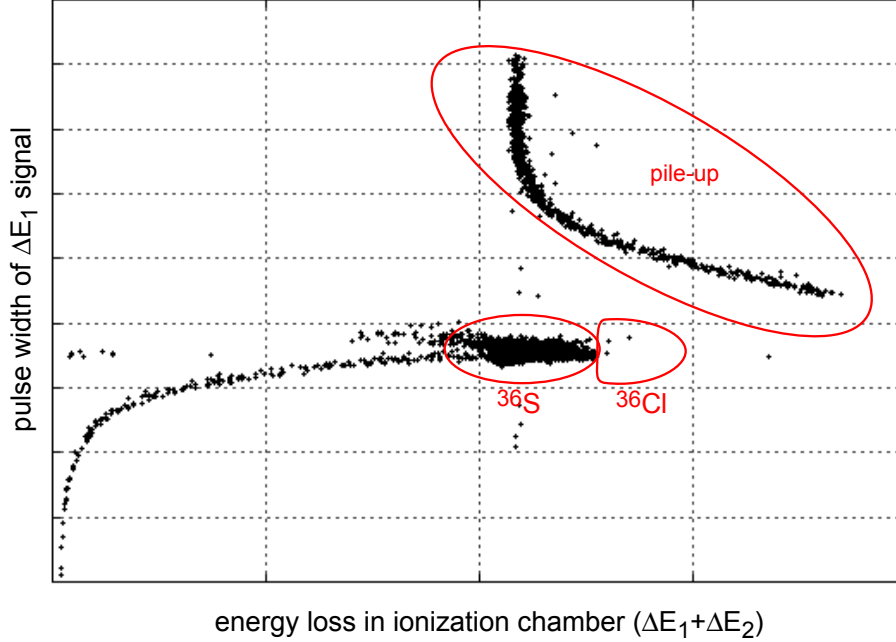


Figure 3.21: Pulse width and total energy loss in the ionization chamber of ^{36}S ions recorded at a count rate of 500 Hz. The tail of pile-up events is clearly separated from the ^{36}Cl region of interest and the regular ^{36}S peak by the pulse width signal.

the scattered ions usually does not exit the ionization chamber. An identification of pile-up based on the higher residual energy of the remaining ^{36}S ion in the silicon strip detector is difficult because of the the silicon nitride exit window and the aluminum entrance window, where a high energy loss in nuclear stopping goes unnoticed. In such a case, the pile-up event would pass all criteria for a ^{36}Cl event and the pulse-width measurement is essential for identification. A plot of the pulse width from 24 MeV ^{36}S ions over their total energy loss in the ionization chamber ($\Delta E_1 + \Delta E_2$) is shown in figure 3.21. The ^{36}S count rate in the detector was 500 Hz. It is obvious that the tail from pile-up stretches over the ^{36}Cl region of interest in the energy loss signal, but that pile-up events can be clearly identified with the pulse width measurement.

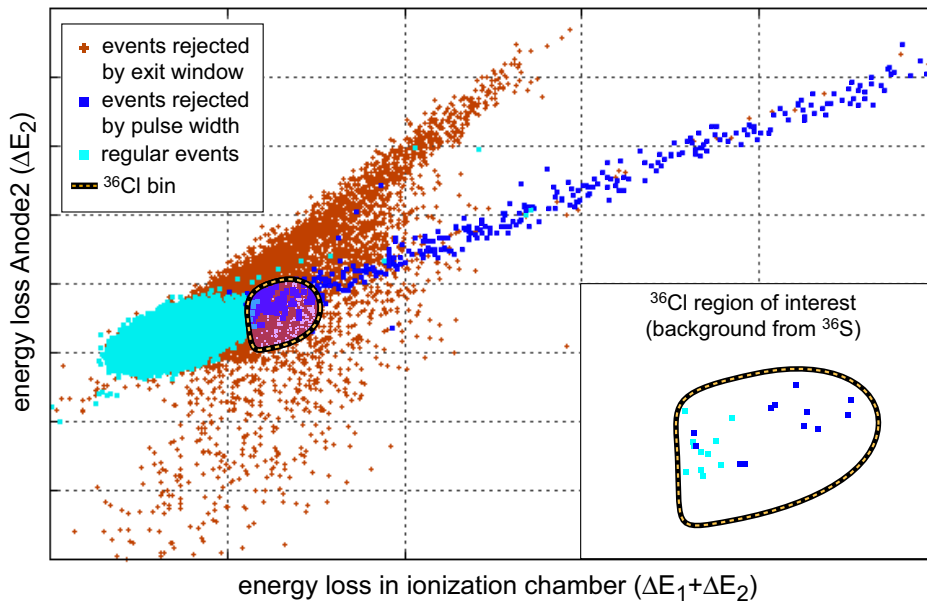


Figure 3.22: Study of the contribution of the exit window and the pulse width measurement to the suppression of tails in the energy loss spectra from the ionization chamber. The data was recorded on ^{36}S at a count rate of 500 Hz. A large number of irregular events are rejected by the exit window (brown), but events in the pile-up tail are only identified by evaluation of the pulse width signal (blue). Only very few of the regular ^{36}S events (cyan), that fulfill both criteria, end up in the ^{36}Cl region of interest. The insert shows the ^{36}Cl region of interest with all events out of the total of 500 000 ^{36}S ions, that fulfill all other ^{36}Cl -criteria. Almost 50 % of them are identified as pile-up by analysis of the pulse width signal (blue) and rejected. Finally, only 11 are misinterpreted as ^{36}Cl events (cyan).

A detailed study of the contributions of various detector signals to the suppression of tails in the energy loss spectra of the ionization chamber is shown in figure 3.22. The pressure in the ionization chamber was optimized for highest sulfur suppression. The way to plot the events used here typically provides the best two-dimensional separation of isobars. Accepting all events, the tails from ^{36}S cover the whole ^{36}Cl

region of interest. A majority of those events originate from scattered ^{36}S ions, which are rejected by the exit window aperture and only the tail from pile-up remains. At the optimum pressure, this tail passes partly through the ^{36}Cl region of interest, but is efficiently suppressed by evaluating the pulse width signal. A very weak ^{36}S tail of unknown origin remains but misses the ^{36}Cl region of interest. As usual, a few events of the regular ^{36}S peak fall within the ^{36}Cl bin. With all other conditions of the ^{36}Cl region of interest set appropriately, the pile-up rejection considerably reduces the number of ^{36}S events, which are misidentified as ^{36}Cl . At count rates above 500 Hz, the pulse width measurement enhances the ^{36}S suppression typically by 50 % and is a major contribution to the good performance of the detection setup.

The maximum count rate, which the detection setup can handle without any noticeable decrease in sulfur suppression, is around 4 kHz. While the pile-up rejection works fine even at higher count rates, the heights of the energy loss signals from the ionization chamber start to decrease because of electric field shielding by residual positive detector gas ions. As a consequence, the distance between ^{36}Cl and ^{36}S peaks in the spectra is also reduced and the amount of decrease is a function of the count rate, which makes reliable data evaluation very difficult. Additionally, dead time issues start to play a role at count rates of several kHz and also the data acquisition system reaches its limits. For this reason, the amount of sulfur in the ion beam has to be kept to a minimum. Chapter 4 gives details about the necessary means to ensure a low count rate by appropriate sample preparation and ion source operation.

3.5.2 The residual energy signal from the silicon strip detector

Up to now, only the use of the signals from the silicon strip detector as a coincidence signal has been discussed. This coincidence signal significantly improves the energy loss spectra from the ionization chamber and thereby enhances separation of ^{36}Cl and ^{36}S . As mentioned before, the silicon strip detector provides two residual energy signals as well as xy-position information. Their contribution to the sulfur suppression will be discussed in the following.

The residual energy is measured both on the front junction side (p-side) as well as on the ohmic rear side (n-side). The two measurements were found to be in good agreement, therefore usually only the p-side values were used. In principle, ^{36}Cl and ^{36}S are well separated in residual energy at the end of the ionization chamber and high energy loss tails are efficiently cut by the exit window. Unfortunately, the dead layer of the silicon nitride and aluminum windows is a blind spot for the energy measurement and especially angular scattering in these layers leads to new low energy tails in the residual energy spectra. Figure 3.23 shows residual energy loss spectra from a ^{36}Cl blank sample and a reference material with a $^{36}\text{Cl}/\text{Cl}$ ratio of 10^{-11} from one of the earlier beamtimes. In later beamtimes, weak shadows of the peaks appeared on the low energy tails in the spectra, probably due to increasing radiation damage of the detector.

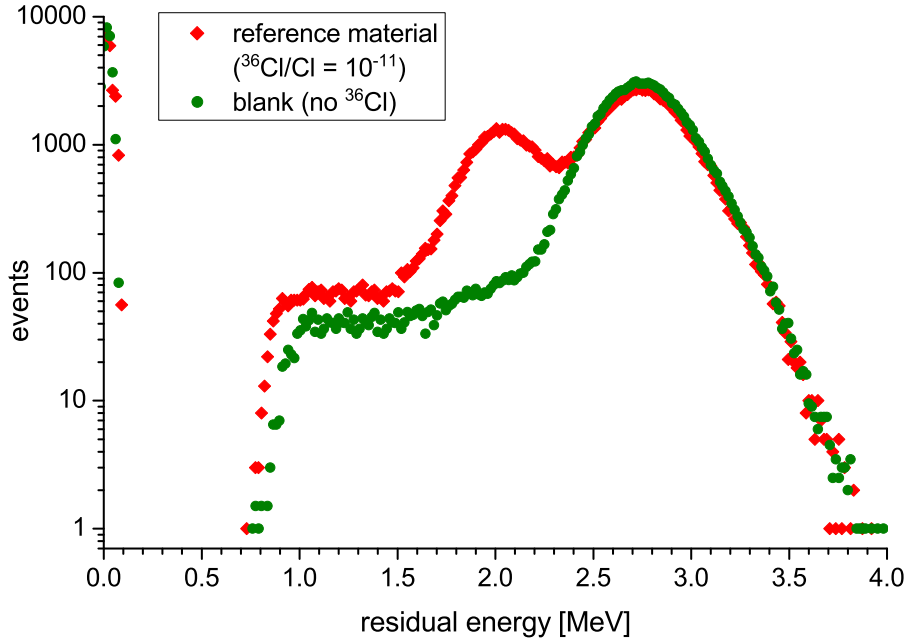


Figure 3.23: Residual energy spectra from the silicon strip detector recorded on a reference material ($^{36}\text{Cl}/\text{Cl} \approx 10^{-11}$, red) and a stainless steel target (^{36}Cl blank, green). The high peak at 0 MeV energy loss stems from ions that did not reach the strip detector.

As a consequence of the tails, the contribution of the residual energy signal to isobar separation is fairly low compared to that of the ΔE_1 signal and especially the $\Delta E_1 + \Delta E_2$ signal. The individual contributions are summarized in table 3.7. The overall gain in sulfur suppression by adding the residual energy signal in a more-dimensional evaluation (see section 5.4.1 for details) is about a factor 3. Previous studies on the performance of various detection systems [61] revealed that a residual

| signal | sulfur suppression |
|--|--------------------|
| ΔE_1 | 240 |
| $\Delta E_1 + \Delta E_2$ | 4 500 |
| E_R | 25 |
| $\Delta E_1, \Delta E_2, \Delta E_1 + \Delta E_2$ | 7 500 |
| $\Delta E_1, \Delta E_2, \Delta E_1 + \Delta E_2, E_R$ | 20 000 |

Table 3.7: Contribution of the individual detector signals to the sulfur suppression. Only events, which passed the exit window and have a correct pulse width, were accepted. The stated sulfur suppression values are based on the evaluation of the one-dimensional histograms of the respective signals without any further conditions set for all other detector signals. The ΔE_2 signal alone provides almost no sulfur suppression.

energy measurement via an additional time-of-flight measurement slightly enhances the suppression. While this idea was not further pursued because of the complexity of the setup, it suggests that a better residual energy measurement with less dead layers in between can raise the sulfur suppression. This will be considered in future detection setups.

3.5.3 The position information from the silicon strip detector

The silicon strip detector provides xy-position information with 16×16 pixels distributed over a $5 \times 5 \text{ cm}^2$ active area (see section 3.1.2 for details). The initial idea was to use this position measurement as an additional source of information about a particle's trajectory through the detection setup and thereby identify ^{36}S events that fall within the ^{36}Cl region of interest. Additionally, the position signal can be used for

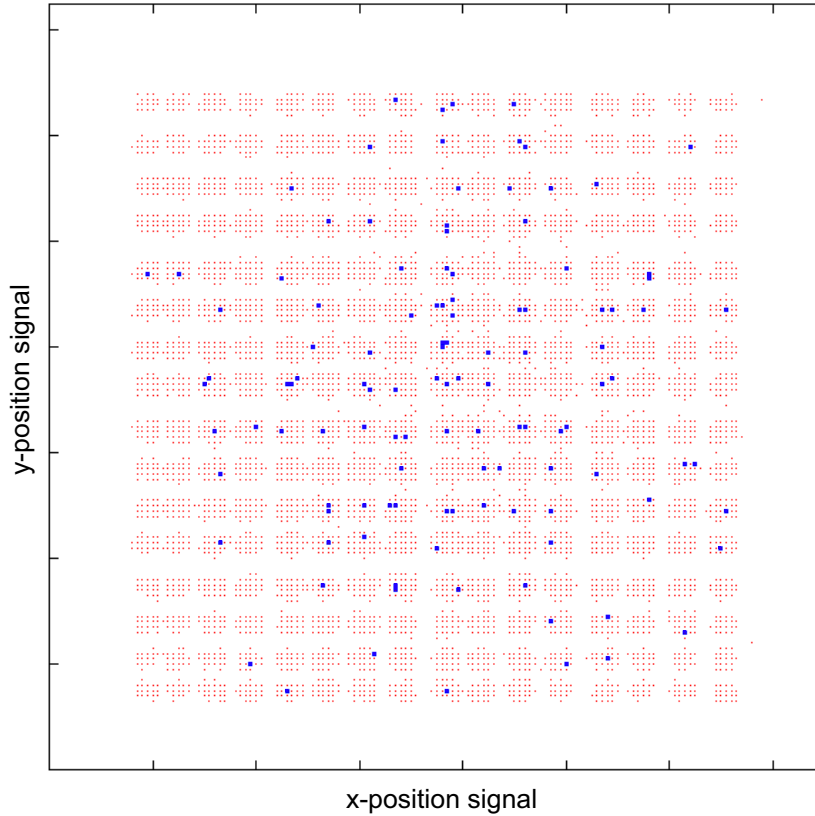


Figure 3.24: Plot of the position information from the silicon strip detector from a run on a ^{36}Cl blank (steel target). The red dots show all ^{36}S events, the dark blue symbols show the final position of those events, that fall within the ^{36}Cl region of interest. They do not end up in a specific area but are distributed over the whole detector just like all other events.

energy calibration of the various strips to obtain a better residual energy signal [61]. A plot of the position information from a run on a steel target (^{36}Cl blank) is shown in figure 3.24. The 256 pixels are clearly distinguished, however the ^{36}S events, which cause background for ^{36}Cl , are randomly distributed over the whole area according to the intensity of the beam. Furthermore, no correlation of the position information with any of the energy loss signals was observed. Therefore, no special information regarding particle identification could be retrieved and the position signal is not used for sulfur suppression.

In earlier measurements, the same result was already obtained with the strip detector mounted at 63 cm distance from the exit window of the ionization chamber. Since ions, that ended up far from the beam axis, did not exhibit a higher probability for causing background, the strip detector was moved closer to 30 cm behind the exit window. While this increased the efficiency of the detection setup because less ions missed the strip detector, no increase in background as a consequence of the higher angular acceptance was observed. It seems that the final position in the silicon strip detector bears almost no information about the trajectory through the

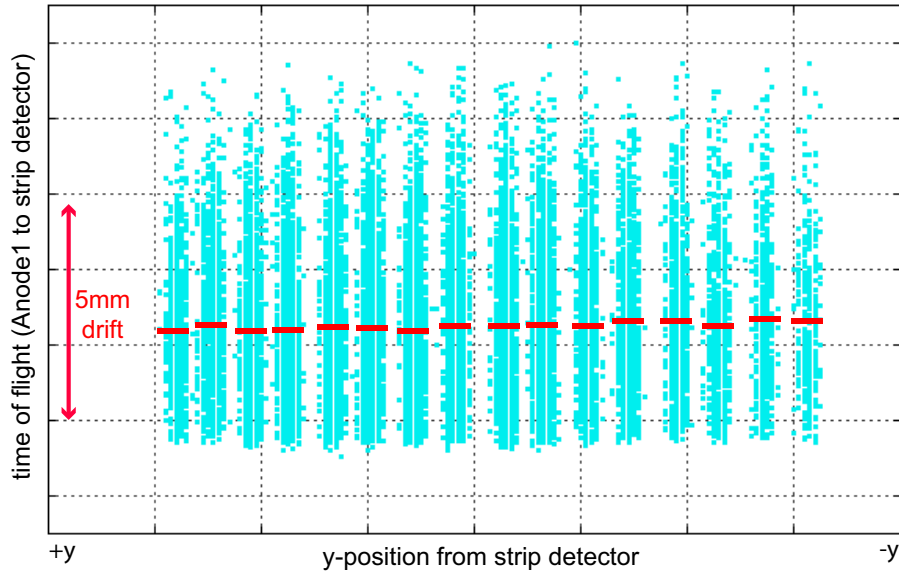


Figure 3.25: Plot of the y-position information from the silicon strip detector and the time between ionization chamber and silicon strip detector signals. The latter information is an indirect measurement of the y-position in the ionization chamber via different drift times of the electrons to the Frisch grid. In this plot, a shorter time-of-flight corresponds to a higher y-position in the ionization chamber. Only events with a certain residual energy were accepted. The red bars show the mean TOF values for each strip, the red arrow indicates the time difference expected due to the drift time of electrons through 5 mm gas. Only a very weak correlation between the two signals is observed, the final y-position information is almost independent from the trajectory through the ionization chamber.

ionization chamber. This was verified in an experiment where the time between the ΔE_1 signal and the strip detector signal was measured with a time-to-amplitude converter. While the silicon strip detector gives a very fast signal, the timing of the ΔE_1 signal depends on the drift time of the electrons to the Frisch grid. Therefore this TOF-measurement gives some information about the distance of the ion trajectory to the Frisch grid (y-position in the ionization chamber). The results are shown in figure 3.25. Only a very weak correlation between the time-of-flight and the final y-position information in the silicon strip detector can be observed, much smaller than expected from the additional drift times of electrons through 5 mm gas. This is a strong hint that the final position almost exclusively depends on angular scattering in the exit window of the ionization chamber, which bears no significant information for isobar separation.

Summarizing, it turned out that the exit window aperture and the residual energy measurement but not the information about final position are the cause for the strong increase in sulfur suppression. This information can in principle be obtained from any energy-sensitive particle detector mounted behind the ionization chamber. The only advantage of the large silicon strip detector is its large size that allows to distribute the beam intensity over a big active area and thus keep radiation damage low. For test purposes, the silicon strip detector was recently replaced with a silicon surface barrier detector from ORTEC (model BU-016-150-100, 150 mm² active area, [102]), which was mounted directly behind the exit window of the ionization chamber. Experiments proved that this setup provides the same sulfur suppression as the silicon strip detector. Because of the still focused beam at this short distance after the exit window, the surface barrier detector most likely will have to be replaced after a few regular beamtimes due to the strong radiation damage. Nevertheless, it is a viable temporal solution in case of complete radiation damage of the silicon strip detector.

Based on all the findings in this chapter, a dedicated ionization chamber with an additional anode for residual energy measurement and the possibility to insert apertures in between the anodes is in preparation. With this detector, one not only gets rid of problems associated with radiation damage but also of the dead layer before the residual energy measurement as no more windows in between are necessary.

4 The ion source and sulfur output from the sample

The ubiquitous presence of sulfur and the volatility of chlorine pose some serious challenges in the preparation of ^{36}Cl samples for AMS and in the operation of the ion source. This chapter describes our strategies to address these problems in order to produce a stable Cl-beam with a low sulfur content.

4.1 Reduction of sulfur output from the sample

A presence of sulfur in the sample material at the level of a few ppm translates into a $^{36}\text{S}/^{35}\text{Cl}$ isotopic ratio of $\sim 5 \times 10^{-10}$, which is several orders of magnitude higher than typical $^{36}\text{Cl}/\text{Cl}$ ratios. Therefore, high efforts are necessary to keep the sulfur content of a ^{36}Cl sample as low as possible. A clean Cl-beam is all the more important if no isobar separation technique prior to the detector like a degrader foil (e.g. [11]) is used to reduce ^{36}S within the ^{36}Cl beam. Guiding the ion beam directly into the detector has the benefit of a high detection efficiency but makes the setup more sensitive to sulfur contamination. Even a low sulfur content in the ion beam of $^{36}\text{S}/^{35}\text{Cl} \approx 5 \times 10^{-11}$ corresponds to a ^{36}S count rate of 500 Hz under typical measurement conditions at our facility. For samples with a higher sulfur content, the maximum count rate for the detection setup of ~ 4 kHz thus sets an upper limit for the beam current during measurement and requires longer data acquisition times. With a ^{36}S suppression of 20 000, the sulfur content is also the main source of background for low-level ^{36}Cl -samples (see section 6.3). Experience has shown that the sulfur output from the ion source does not only depend on the amount of sulfur in the sample material but also on surrounding materials. The assessment of various influences on the sulfur content of the ion beam are discussed in detail in the following sections.

4.1.1 Sample preparation and handling

Natural ^{36}Cl samples require good chemistry for sulfur removal. Precipitation of chlorine as silver chloride after sulfur removal by precipitation of BaSO_4 is an established method [103, 104]. Since the exposure dating samples described in section 6.5 were prepared at dedicated chemistry laboratories by our collaborators, only AgCl samples from NaCl as raw material were prepared at our lab. For this purpose, the

above procedures were slightly modified. The NaCl was suspended in bi-distilled water or 0.5 M nitric acid to a concentration of 12.5–125 g/l depending on the desired amount of AgCl per sample. As raw blank material, we used NaCl from Alfa Aesar (Sodium chloride, Puratronic®, with a purity of 99.999 %, Art# 10862, [105]). Also AgNO₃ from Merck (Silver nitrate pro analysis, Emsure®, Art# 101512, [106]) was suspended in 0.5 M nitridic acid to a concentration of 70–350 g/l. Around 0.5 g/l of Ba(NO₃)₂ and a baked quartz filter were added to each solution followed by at least 24 hours rest time for the precipitation of sulfur in the form of BaSO₄.

During sample preparation, the aliquots of the solutions were filtered by pressing them through quartz filters in pipette tips with 2 bar nitrogen and collected in colorless 1.5 ml Eppendorf Safe-Lock TubesTM [107]. Prior to use, these tubes were first washed with bi-distilled water and further cleaned with isopropanol and 1.4 M HNO₃ in an ultrasonic bath for at least 10 min. When the filtered AgNO₃ was added, the silver chloride formed readily. The samples were centrifuged to form a AgCl tablet. After disposal of the excess liquid, bi-distilled water pretreated with Ba(NO₃)₂ was added and the tablet was dispersed again by putting the tubes in the ultrasonic bath. Following final centrifugation and removal of liquid, the AgCl tablets were dried in the dark oven at 90° for at least 5 hours. The AgCl sample tubes were then put into storage containers, which were wrapped in aluminum foil to prevent photo-decomposition of silver chloride. Big AgCl targets containing more than 20 mg of AgCl prepared according to the above procedure show a very small sulfur content (³⁶S/³⁵Cl < 10⁻¹²) [58]. No influence of the storage time of AgCl samples on their sulfur content has been observed, although several samples were stored for more than two years. Glass vials were also tested as sample tubes but brought no improvement regarding sulfur contamination compared to the standard Eppendorf tubes.

For tuning purposes and the laser experiments (see sections 5.1 and 7.2), special AgCl materials containing 100 ppm, 1000 ppm and ~ 10 % Ag₂S were produced. The sulfur was added to a NaCl-solution (with water, no HNO₃) via Na₂S from Sigma-Aldrich (Sodium sulfide, nonahydrate, purity ≥ 98.0 %, Art# 208043, [108]) suspended in water to concentrations of 0.2–20 g/l. The resulting solution was acidified to a ph-value of ~ 6.5 by adding either 0.01 M or 0.1 M HNO₃, then the AgNO₃ solution was added immediately. This ensured precipitation of AgCl without substantial loss of sulfur via formation of H₂S. The targets were centrifuged and dried in the oven without additional cleaning steps.

For sample pressing, we use a hand press and two different punch heads, which are shown in figure 4.1. First, the conic hole of a cleaned Cu-cathode is lined with silver bromide powder and pressed with 20 kg m with punch # 1 to form the AgBr-backing (see next section). To obtain the AgBr powder, the AgBr tablets produced at our lab are ground with a teflon mortar. In a second step, the silver chloride sample material is put in the center of the cathode and pressed with 7 kg m onto the AgBr-backing with punch # 2. Only for small samples below 1 mg, punch # 1 is used also for the AgCl. Depending on the amount of sample material, the area covered with AgCl has

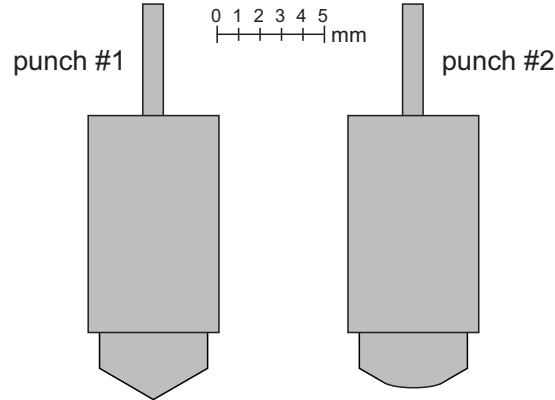


Figure 4.1: True to scale drawing of the punch heads used in our sample press. The conic head (# 1) is for pressing of the backing material, the flattened head (# 2) for the silver chloride sample material.

a diameter of 1–2 mm. Usually, the samples are pressed one day prior to mounting the sample wheel in the ion source. Up to mounting, they are kept in Eppendorf tubes in a lightproof box. In this way, even a maximum storage time after pressing of one week has no influence on the final sulfur output.

4.1.2 Target wheel, cathode design and backing material

As mentioned before, experiments have shown that the sulfur content of the silver chloride itself is very low with a corresponding $^{36}\text{S}/^{35}\text{Cl}$ ratio in the extracted ion beam below 10^{-12} [58]. In practice, the sulfur content of the ion beam from AMS samples is much higher and the majority of sulfur comes from other sources such as the surrounding sample holder or materials within the ion source. Therefore most labs use special cathode and/or backing materials with low sulfur content, a recent overview is given in table 1 in [99]. Additionally, most ^{36}Cl sample holders have a larger diameter than typical AMS sample holders for other isotopes. After some initial tests, we are now using cylindrical Cu-cathodes (6 mm diameter) with a conical hole (5 mm inner diameter) coated with silver bromide as backing material. The Cu-cathodes are produced at our own workshop, hence easy machining was also a design criteria. A new aluminum sample wheel allows loading 40 targets, which are held by clips on the backside of the wheel. Pictures are shown in figure 4.2.

Figure 4.3 shows a cross-section of the cathodes as well as a scan of the chlorine and sulfur output over the sample arrangement made possible via some modifications of our ion source [54]. Despite the backing material, the sulfur output from areas adjacent to the sample material is up to two orders of magnitude higher than with the Cs beam centered on the AgCl sample. These results motivated further investigations of the sulfur output of different materials.

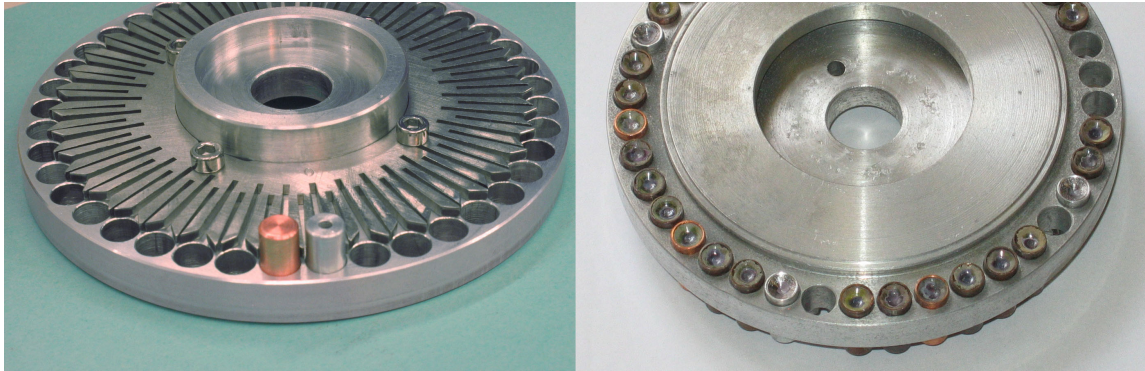


Figure 4.2: Photos of the new sample wheel for 40 cathodes and the clips at the back side of the wheel. Apart from the standard Cu-cathodes, also test cathodes made of aluminum were used at the time the pictures were taken.

As part of a search for suitable backing materials, we screened different batches of silver bromide. Table 4.1 lists the average sulfur output from 4 mg AgCl samples on various backing materials. Results with commercially available AgBr from Alfa Aesar (Silver bromide, Premion®, purity 99.998 % metals basis, Art# 12110, [105]) and Sigma-Aldrich (Silver bromide, purity 99.999 %, Art# 226807, [108]) were rather unsatisfactory and this material is now only used for tuning samples. By far the lowest sulfur output was achieved with our own AgBr produced at the VERA laboratory from KBr cleaned from sulfur by precipitation of BaSO₄ according to the procedure for AgCl described in section 4.1.1. The low sulfur content of this material was very reproducible and varied only a little between different batches. Higher sulfur contents tended to occur for AgBr produced in winter, which was attributed to seasonal changes in the sulfur content of the air due to household emissions. Subsequently, our

| cathode material | backing material | average sulfur output (³⁶ S ⁻ / ³⁵ Cl ⁻) |
|------------------|--------------------|---|
| Cu | AgBr VERA | 5×10^{-11} |
| Cu | AgBr Alfa Aesar | 2×10^{-10} |
| Cu | AgBr Sigma-Aldrich | 3×10^{-10} |
| Al | Ta | 5×10^{-10} |
| Al | Ta (H-baked) | 4×10^{-10} |
| Ni | none | 6×10^{-10} |

Table 4.1: Average sulfur output from the ion source using various cathode and backing materials. All cathodes contained around 4 mg of the same AgCl blank material and were sputtered for at least 30 min prior to measurement to remove surface contaminations and establish stable conditions. Best results were achieved with AgBr produced at VERA.

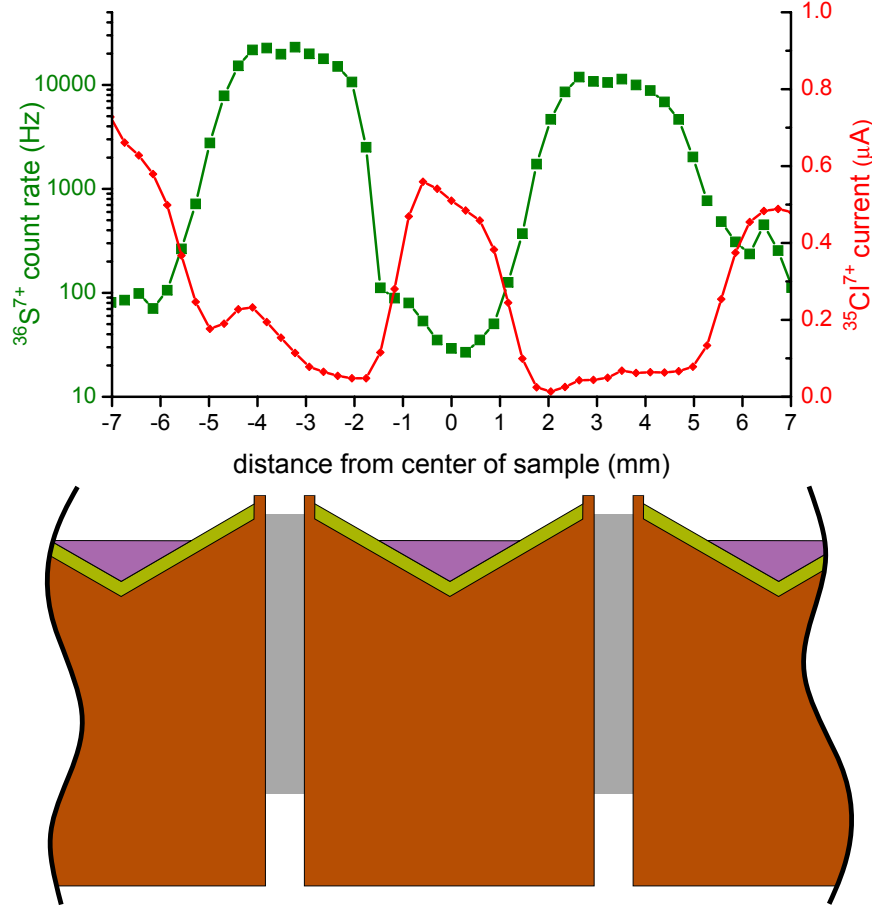


Figure 4.3: Cross section of Cu sample holders (brown) with AgBr backing (yellow) and the AgCl sample material (pink) in the center. The upper graph shows results from a lateral scan with the Cs beam over the target surface. The sulfur output (green curve) from the backing material and especially the sample holder materials is significantly higher than from the silver chloride sample itself.

inhouse AgBr was preferably produced during summer months. Following the results from Conard et al. [103] and Synal et al. [109], we also tried aluminum cathodes with tantalum plates as backing material. Despite etching the plates with hydrofluoric acid and/or baking them in H_2 for several hours at $700^\circ C$, the sulfur output still was one order of magnitude higher than from AgBr. In addition, stability of the AgCl sample in the tantalum plates turned out to be a delicate issue under thermal conditions in the ion source and a few test samples were lost.

Experiments with Ni-cathodes (Nickel rod, purity 99.5 % metals basis, Art# 11454 from Alfa Aesar [105]) without additional backing material (suggested by [11]) showed that the sulfur content in nickel was orders of magnitude lower than in copper, steel or aluminum. Nevertheless, the sulfur output from AgCl in Ni-cathodes was one

order of magnitude higher than with the standard AgBr-backing. It may well be that this is because a different nickel material than in [11] was used. Summarizing, the advantages of a silver bromide backing are its low sulfur output and the excellent stability of the AgCl sample material within the sample holder. No satisfying alternative to this quite laborious method has been found so far.

4.1.3 Sample size and sulfur contamination

Since chemically cleaned AgCl typically has a lower sulfur content than the backing materials, the sulfur output from a sample strongly depends on the size of the AgCl-sample or more precisely the area covered with AgCl. Most labs therefor require $\sim 4 - 6$ mg AgCl per sample, although only a small fraction is used up during measurement. In order to facilitate a reduction of primary sample material and chemical effort, we investigated the limitations regarding minimum sample size. While output currents of several $\mu\text{A } ^{35}\text{Cl}^-$ at typical source settings can be achieved even for 1 mg samples, the sulfur output increases significantly with decreasing sample size. The average sulfur output for various sample sizes is summarized in table 4.2. Misalignment of the small AgCl samples during pressing is no issue for the measurement since our ion source provides a mechanism for scanning the target wheel position both in horizontal as well as in vertical position for maximum chlorine output [54]. At one of the sources, position offset values can be set individually for each target during automated measurement.

For samples with a $^{36}\text{Cl}/\text{Cl}$ ratio of 10^{-12} or above, a higher sulfur induced background is usually acceptable, provided that the ^{36}S count rate is still manageable for the detection system, and a few samples below 0.5 mg AgCl have been measured successfully. For low ratio samples on the other hand, the increase in sulfur induced background is of course significant and a reduction of sample size below 2 mg AgCl for

| sample size AgCl [mg] | average sulfur output ($^{36}\text{S}^-/^{35}\text{Cl}^-$) | detector count rate at $10 \mu\text{A } ^{35}\text{Cl}^-$ [Hz] |
|--------------------------|---|---|
| > 4 | 5×10^{-11} | 500 |
| ~ 2 | 1×10^{-10} | 1 000 |
| ~ 1 | 6×10^{-10} | 6 000 |
| ~ 0.5 | 1×10^{-9} | 12 000 |

Table 4.2: Average sulfur output from the ion source as a function of sample size. All cathodes had the same AgBr backing and contained the same AgCl blank material. Each sample was presputtered for at least 30 min. The sulfur output quoted is the average over all samples with the same amount of sample material, with at least 2 h of measurement time on each sample. The corresponding ^{36}S count rate in the detector is stated for the current goal of $10 \mu\text{A } ^{35}\text{Cl}^-$, which was not reached for the smallest samples.

routine measurements seems only feasible with additional means of sulfur suppression (possible techniques are discussed in chapter 7).

The negative ionization yield measured on 3 mg AgCl-samples is 11–13 %. This value is only a lower limit since there is usually a fair amount of residual sample material left in the cathode when the high sulfur count rate (> 20 kHz), which arises once a hole has been sputtered through the AgCl layer, does not allow further measurements. At $10\text{ }\mu\text{A}$ $^{35}\text{Cl}^-$ current, 3 mg of AgCl therefore correspond to more than 6 hours of available measurement time on each target. This is long enough to acquire $\sim 1\,000$ ^{36}Cl events (corresponding to 3 % statistical uncertainty excluding sulfur induced background correction and normalization) on a sample with a $^{36}\text{Cl}/\text{Cl}$ isotopic ratio of 10^{-14} . Most targets are larger, thus allowing even longer acquisition times. The high grade of automation of our facility allows for such long measurements, even though only exceptional samples may justify this effort under routine conditions.

4.2 The SNICS ion source and sulfur output

Currently two 40-sample-MC-SNICS ion sources from NEC [48, 110] are in operation at VERA. Both have undergone significant modifications to allow fine adjustment of the horizontal and vertical position of the sample wheel [54]. While the more recently installed MC-SNICS-II (source S2) at the new injector [52] still uses the original pneumatic wheel drive for sample changing, the older source (source S1) has been equipped with a stepper-motor driven sample changer [54]. It has the advantage of shorter switching time between samples due to generally faster sample changing as well as the ability to turn the wheel in both directions. This difference has implications for the regulation of the ion source output in the case of volatile elements such as chlorine, as discussed in the next section. During operation, the admittance of Cs into the source volume is controlled via the heating of the Cs-capillary, the Cs oven temperature is kept constant.

Based on the results from Weisser et al. [111], both sources now have spherical ionizers instead of conical ones to achieve higher source output and better focussing of the Cs beam on the sample. Especially the latter is of importance for Cl measurements because it helps to reduce the sulfur output from the ion source by confining most of the Cs-beam on the very sulfur poor silver chloride target itself. The dependence of the sulfur output on the size of the Cs-beam at the sputter target can be very well measured by changing the Cs-focus-voltage and has also been observed at other facilities [98].

Although very high chlorine output currents are theoretically possible, experience has shown that the volatility of chlorine requires operation of the ion source at outputs around $10\text{--}20\text{ }\mu\text{A}$ $^{35}\text{Cl}^-$ current to avoid melting of the sample (compare e.g. [109]). Generally, ion source regulation for chlorine is quite delicate, our recipe is presented in the next section. Furthermore, changes in ion source conditions also

seem to influence the sulfur to chlorine ratio in the negative ion beam. The issue of cross contamination and memory effect of the ion source is discussed in section 6.3.1.

4.2.1 The ion source regulation

The source output at VERA is controlled and stabilized with a dedicated source regulation program. It uses either the cathode current or the current from the source high voltage power supply for a feedback regulation of the ionizer power and/or the cesium admittance to the source volume via the capillary heating (line heater). The regulation used has ID (integration-differentiation) characteristics. Additionally, the program automatically evaluates the quality of individual samples and reduces the regulation on bad targets to avoid misleading changes of source parameters. For most isotopes, the ionizer power is kept constant around 170 W and the source output is only controlled via the Cs capillary heating to compensate slow changes in ion currents with typical time constants of hours.

In early experiments with ^{36}Cl however, the volatility of the sample material easily caused an uncontrolled, even exponential increase of the source output from around 5 μA to over 100 μA $^{35}\text{Cl}^-$ current within a few minutes. This runaway behavior could not be stopped with the usual settings of the source regulation and often ended in complete melting of the sample. It soon became obvious that much faster means of source control were necessary for chlorine and we subsequently adopted an approach from the AMS facility at ANU, Canberra, which have a very similar ion source and routinely measure a high number of ^{36}Cl samples [112]. In order to achieve constant Cl^- output from our Cs-sputter source, we now regulate the ionizer power while the cesium capillary temperature is kept at typical values used for other AMS isotopes and is only adjusted according to the longterm mean of the ionizer power. Since the cathode current during ^{36}Cl measurements is extremely low as a result of cold source conditions, the source output is monitored via the current from the high voltage power supply. The regulation calculates and sets a new ionizer control current value roughly every 20 s within upper and lower limits for the ionizer power. The step size of the change is adjusted according to the deviation of the measured output from the desired value and its derivative and allows for changes of up to 3 W per minute. For most other isotopes, the scaling factors employed in the calculation of the response are several orders of magnitude lower, for chlorine however, sharp response proved essential to avoid runaway conditions.

With optimized regulation parameters, the control program now achieves the same Cl^- current on all samples in the wheel typically within 100 s after sample change. The Cl^- current can be kept constant within 25 % during a beamtime of several days. Figure 4.4 shows the $^{35}\text{Cl}^-$ current and the ionizer power over a 20 h period during measurement. The source regulation achieves almost constant output with quick but only minor changes of the ionizer power. Initial problems of overshoots of the regulation, as shown in figure 4.6, were eliminated.

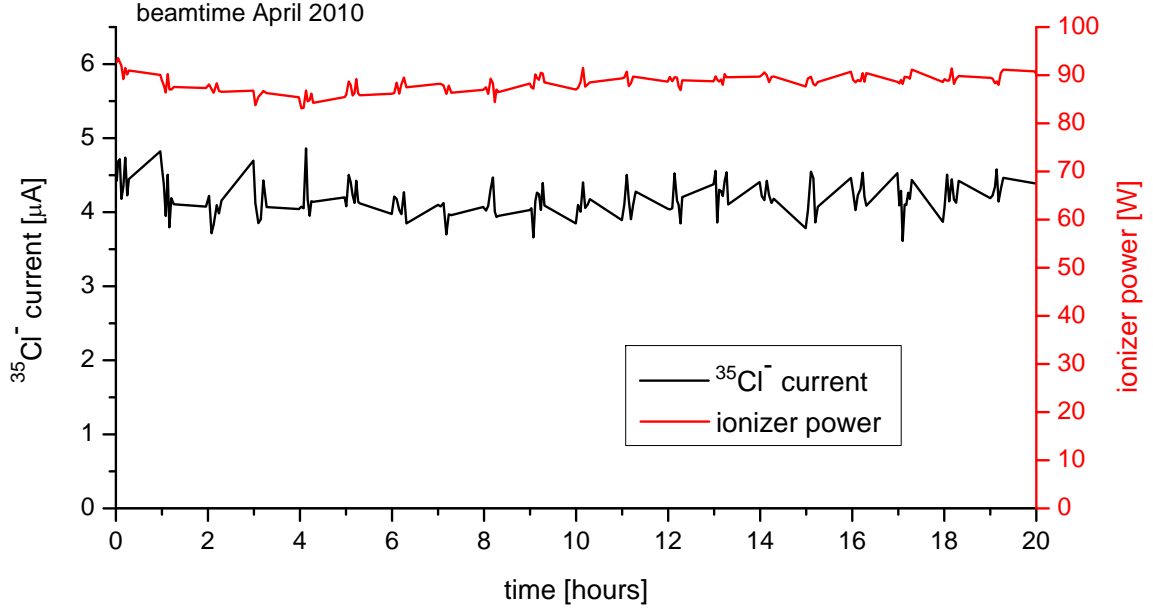


Figure 4.4: $^{35}\text{Cl}^-$ current (black) and ionizer power (red) over a 20 h period during a beamtime in April 2010. The regulation achieves very constant source output on all samples of the wheel despite the relatively short measurement times of $\sim 7\text{--}10$ min per sample. Because of the fast reaction time of the regulation, the ionizer power has to be varied by just a few watts.

The only problem, which still remains, is that long changing times between different targets apparently disturb the ion source and lead to significant cool-down. This occurs especially at source S2 during changes to far away wheel positions (almost full turns of the wheel by the pneumatic drive). In such cases, the regulation takes substantially longer to reach the normal source output again. For this reason, most measurements were performed from source S1 with its faster changing mechanism.

4.2.2 Operation parameters and sulfur output

The power transfer of the Cs beam to the silver chloride sample during sputtering has to be kept as low as possible to avoid melting of the sample and to minimize evaporation of chlorine. For this reason, we follow the approach of other labs [98] and reduce the cathode voltage during chlorine measurements from normally 5 kV to 3 kV. Subsequently, also the extraction voltage has to be lowered to only 9 kV instead of the 15 kV used for other isotopes to have similar beam focussing in the source region. In order to compensate for these lower source voltages, the main acceleration voltage of the source is set to 58 keV. Thus the energy in the injector is the standard 70 keV. The Cs-oven temperature is around 150° and the capillary heating current is 15–25 A, which is the same as for other isotopes. The ionizer power typically is

around 90 W for 5–10 μA $^{35}\text{Cl}^-$ current, the actual value differs quite a lot among various beamtimes, which is most likely related to the amount of Cs present in the source. Generally, a higher ionizer power (110 W) is required shortly after source maintenance or cleaning.

With these source settings, the measured cathode current is below 50 μA , which is close to our measurement limit. This number is only an upper limit for the actual Cs^+ current as the cathode current may contain contributions from other species such as accelerated electrons. Experiments on the cross contamination and memory effect of the ion source, which are discussed in section 6.3.1, suggest that also evaporated chlorine plays an important role. For these reasons, the current of the high voltage power supply is used instead to monitor the source output for the feedback-regulation. In this way, the above source parameters and the regulation now guarantee a stable chlorine beam and no loss of samples due to melting has occurred since.

The stability of the sulfur content in the ion beam is another crucial parameter in an AMS measurement and hence deserves some attention. Experience has shown that, even after long sputtering, the $^{36}\text{S}/^{35}\text{Cl}$ ratio from one sample is not constant, as one might intuitively expect. Apart from the previously discussed influences of materials and sample size, the sulfur output also depends on the conditions in the ion source and to a certain extent seems to follow its own rules. One general feature

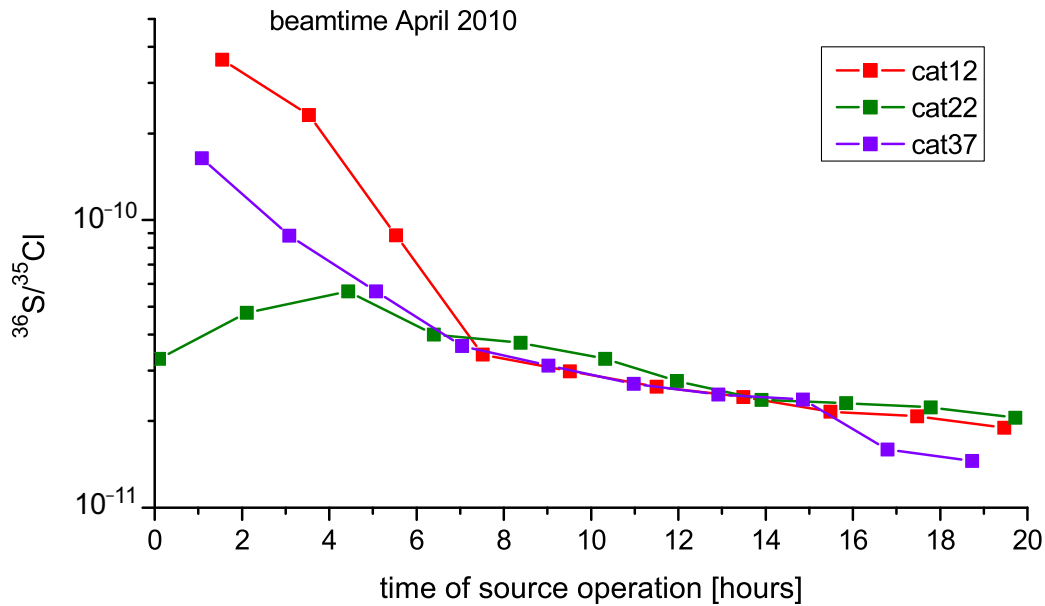


Figure 4.5: Sulfur output as a function of measurement time for three different samples containing the same ^{36}Cl blank material. Each symbol corresponds to a single run with ~ 7 min sputter time. The $^{35}\text{Cl}^-$ current was stable at 4–5 μA with the ionizer around 90 W. All samples were presputtered for 5 min to remove any surface contaminations and establish stable surface conditions.

is that the $^{36}\text{S}/^{35}\text{Cl}$ ratio almost always decreases with sputter time as long as no hole has been sputtered through the AgCl layer. This decrease in sulfur is strongest when first sputtering a fresh sample. Within the first minutes, the $^{36}\text{S}/^{35}\text{Cl}$ ratio typically drops by one order of magnitude until it reaches a comparably constant level. We attribute this to surface impurities that either contain sulfur or change the surface chemistry in favor of sulfur negative ion formation. Also the cesium coverage might play a role and influence surface conditions. For this reason, all samples are presputtered for several minutes prior to data acquisition. Under stable source conditions, the sulfur output from a sample continues to decrease even after hours of sputtering, but at much slower rate than in the first minutes. Whether this behavior is mainly related to further cleaning of the samples or a general cleaning effect in the ion source could not be established so far. Experiments on the origin of the sulfur in the ion beam by sputtering very sulfur poor materials (e.g. a silicon wafer) yielded no useful hints.

Figure 4.5 shows the sulfur output from three typical samples as a function of measurement time with optimized regulation parameters. The data was taken under very stable source conditions (compare figure 4.4), each symbol corresponds to a run of around 7 min. After three runs on each sputter target, initial differences in sulfur output have vanished and all samples have almost the same sulfur content in the ion beam. For the rest of the measurement, the $^{36}\text{S}/^{35}\text{Cl}$ ratio steadily decreases with sputter time.

Interestingly, the above behavior of the sulfur output is only observed under stable source conditions. In other cases we found a strong dependence of the sulfur output on the ionizer power, an example from our investigations is shown in figure 4.6. The data was actually obtained in the early phase of source regulation development with an unfavorable set of regulation parameters that lead to overshoots of the regulation and therefore oscillation of the ionizer power. Surprisingly, a 30 % change in ionizer power can induce a change in the $^{36}\text{S}/^{35}\text{Cl}$ ratio by a factor of up to 40, whereas the chlorine current during this measurement varied only between 0.5 and 2 μA . Although there is some kind of source memory, a higher ionizer power clearly favors conditions which cause a high sulfur output for several runs. The reason for this behavior is not yet clear. During measurement, such unfavorable conditions are now avoided by optimized source regulation and an ionizer power goal of $\sim 90\text{ W}$.

Combination of all the findings presented in this chapter results in an average sulfur output from our ion source of only $^{36}\text{S}/^{35}\text{Cl} \approx 5 \times 10^{-11}$, which translates into a detector count rate of $\sim 500\text{ Hz}$ at $10\text{ }\mu\text{A}$ $^{35}\text{Cl}^-$ current. The corresponding sulfur induced signal in the ^{36}Cl bin is $^{36}\text{Cl}/\text{Cl} \approx 2.5 \times 10^{-15}$. This leaves a satisfactory margin for a possibly higher sulfur output during measurement due to a higher sulfur content of the silver chloride material. For samples with a high $^{36}\text{Cl}/\text{Cl}$ ratio, even sulfur outputs around $^{36}\text{S}/^{35}\text{Cl} \approx 2 \times 10^{-9}$ are acceptable and no higher outputs have been observed for samples with at least 2 mg AgCl. Such high sulfur content in the ion beam can be handled by reducing the beam current, which is easily feasible

for high ratio samples with ample ^{36}Cl count rate. Only for low level samples with $^{36}\text{Cl}/\text{Cl}$ ratios below 1×10^{-14} , a similar sulfur content of the ion beam would require additional means of sulfur suppression. A technique, which provides such additional suppression, is presented in chapter 7.

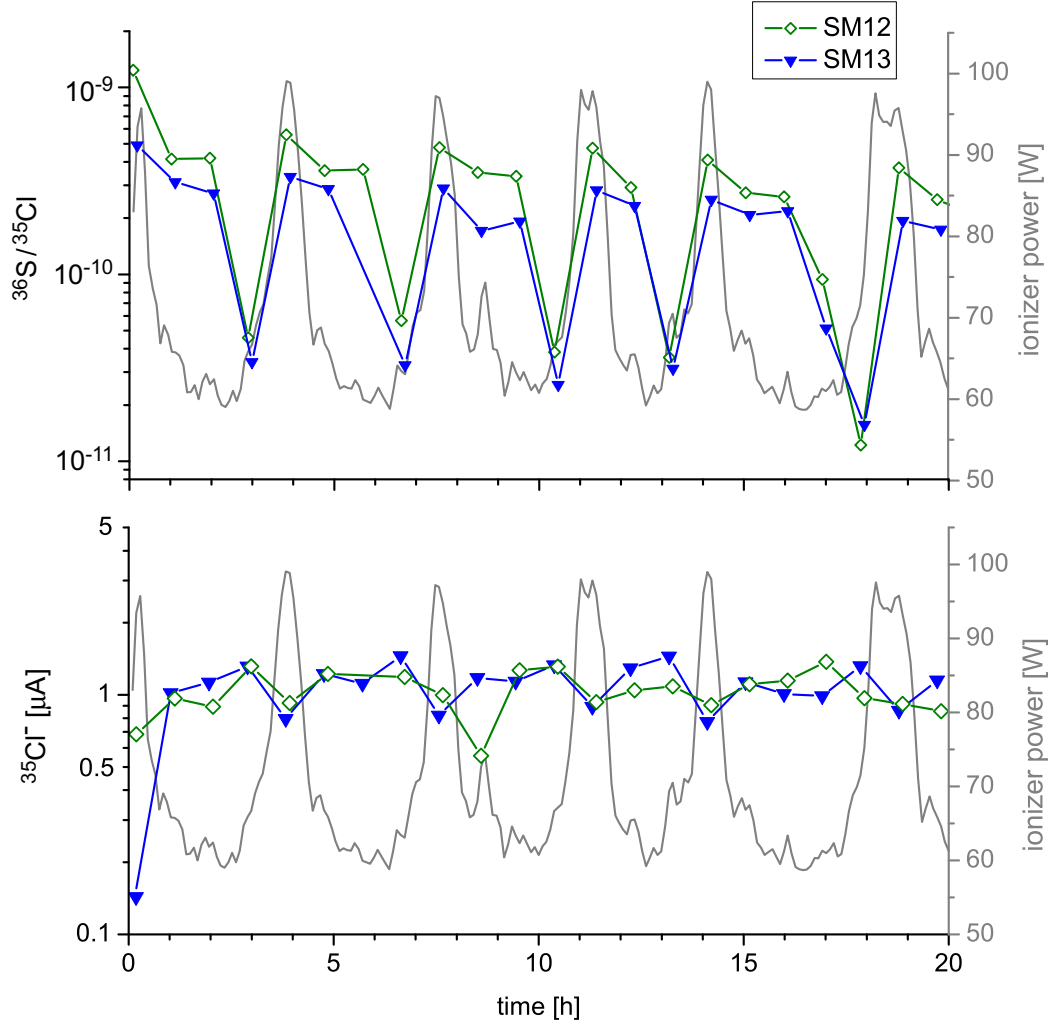


Figure 4.6: Variation of the $^{36}\text{S}/^{35}\text{Cl}$ ratio and the ionizer power over a 20 h period. The two different samples plotted here exhibit the same behavior as the other 8 samples in this measurement. Each point shows the results from one run lasting ~ 5 min. The lower graph shows the $^{35}\text{Cl}^-$ current for comparison. The sulfur output is clearly correlated to the ionizer power, the reason for this is still unclear.

5 Measurement procedure

5.1 Tuning the machine

Initial tuning of the machine for ^{36}Cl measurements takes ~ 8 h. Measurement of all 40 samples in the wheel then typically takes 1–4 days depending on the $^{36}\text{Cl}/\text{Cl}$ ratios of the samples and the required precision of results. If another sample wheel is inserted, retuning is done within less than 3 hours. Hence, tuning consumes only a reasonably small amount of the total beamtime. Like for many other isotopes, tuning of VERA for ^{36}Cl is performed with a semi-automated script and the optimization software *automax* [24]. This program allows a multi-dimensional optimization of a set of machine parameters for maximum signal in one of the diagnostic elements (Faraday cups or detectors). The main components used during tuning and measurement are shown in figure 5.1.

First, the machine is tuned with a pilot beam and gas stripping. Usually, the settings from a previous ^{36}Cl measurement are loaded and electrical components in-

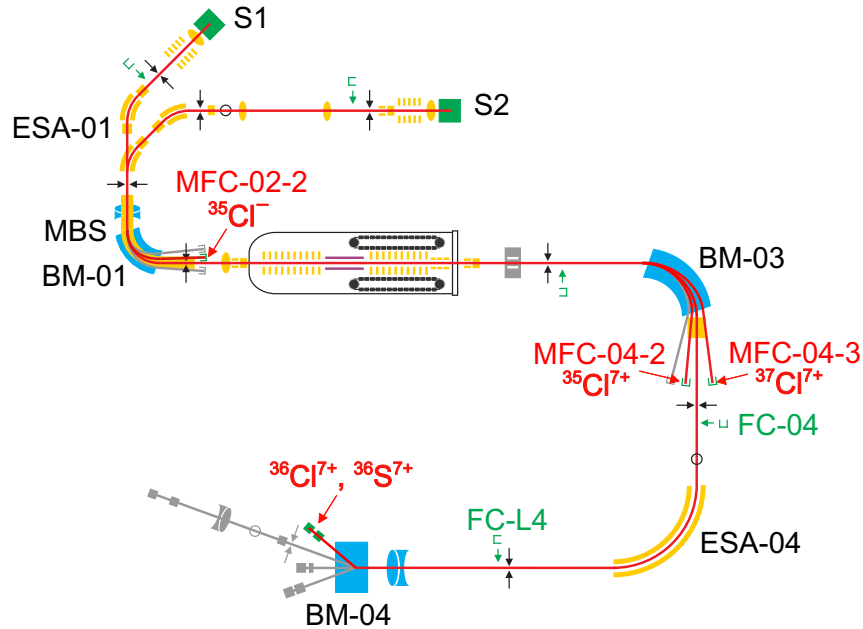


Figure 5.1: Overview of the main components of VERA used for tuning and measurement of ^{36}Cl . For other components, please refer to figure 2.2.

cluding the terminal voltage are scaled for transport of $^{37}\text{Cl}^-$ and $^{37}\text{Cl}^{7+}$ respectively. Most slit apertures are set to 4 mm during tuning, afterwards all slits are opened to at least 8 mm except the slits after BM-01, which stay closed to ± 2 mm for good mass resolution of the injector. The components of the injector are tuned for maximum $^{37}\text{Cl}^{7+}$ current in the Faraday cup FC-04 after the analyzer magnet BM-03. Bending elements, lenses and steerers of the high energy side are optimized using the $^{37}\text{Cl}^{7+}$ current in the last Faraday cup FC-L4. While the tuning is done at 5–10 μA $^{35}\text{Cl}^-$ current, typical $^{37}\text{Cl}^{7+}$ currents with gas stripping are only 20–40 nA due to less than 0.5 % yield for the 7+ charge state.

In the next step, this pilot beam setup is scaled back to mass 36 by changing the electrical components including the terminal voltage. The magnetic fields of BM-01 and BM-03 again stay untouched. The parameters for the multi-beam-switcher (MBS) used for fast sequential injection of masses 35, 36 and 37 are then optimized using the respective currents in the offset Faraday cups on the low and high energy side. Since stable isotope currents from now on are injected just for a few hundred μs with a repetition rate of roughly 5 times per second, it is possible to use terminal foil stripping in the following. Changing to foil stripping is the only sequence in the tuning procedure, for which the operator has to be on-site because the stripper foil drive is manual. Any small energy loss introduced by the stripping foil is compensated for by slightly increasing the terminal voltage.

Since there is no Faraday cup after the switcher magnet BM-04, the last part of the high energy side needs to be tuned with the $^{36}\text{S}^{7+}$ count rate in the silicon strip detector. For this purpose, special AgCl targets containing ~ 50 ppm of Ag_2S have been produced (see section 4.1.1) with corresponding $^{36}\text{S}^{7+}$ count rates of 20 kHz. Use of those special tuning targets assures that most of the sulfur in the beam originates from the sample itself and not from surrounding material. In this way, all components are tuned for optimal transport of the sample material to the detection setup. The alternative use of other sulfur rich target materials such as copper or steel for tuning requires the use of a beam attenuator, the same is the case for the $^{37}\text{Cl}^{7+}$ pilot beam count rate. At VERA, strong attenuation of the beam is only possible with a perforated steel shield, which, from our experience, significantly changes the emittance of the beam and deteriorates the tuning.

During the actual AMS measurement, the terminal voltage is automatically retuned every 24 h to compensate for possible, however seldom occurring thickness changes of the foil. Breaking of the foil occurred only once, normally one foil lasts for 4–5 days of continuous measurement without noticeable changes. Retuning of the injector and the analyzer is also done automatically with the $^{35}\text{Cl}^{7+}$ current in MFC-04-2 and the $^{36}\text{S}^{7+}$ count rate in the detector, generally after 2 days of measurement.

During the tuning procedure, the ionization chamber is operated with a constant gas throughflow to flush the gas volume. Prior to measurement, the detector volume is then closed off to ensure a constant areal density of the counting gas.

5.2 Measurement and data acquisition

As mentioned above, fast sequential injection of different masses is used for the measurement of the $^{36}\text{Cl}/^{35}\text{Cl}$ ratio and the accelerator transmission. For many samples, also the $^{35}\text{Cl}^{7+}/^{37}\text{Cl}^{7+}$ needs to be accurately measured in the offset Faraday cups after the analyzer magnet (MFC-04). The $^{35}\text{Cl}/^{37}\text{Cl}$ ratio allows simultaneous determination of the total chlorine content of the rock material with AMS if an isotopically enriched carrier in sample preparation has been used. Further details about this isotope dilution technique in exposure dating can be found in [113–115].

A typical measurement cycle at VERA lasts about 0.2 s and consists of the measurement of the following parameters: $^{35}\text{Cl}^-$ current in the offset Faraday cup MFC-02-2, $^{35}\text{Cl}^{7+}$ and $^{37}\text{Cl}^{7+}$ currents in the offset cups MFC-04-2 and MFC-04-3 and of course the $^{36}\text{Cl}^{7+}$ and $^{36}\text{S}^{7+}$ count rate in the detection setup. For this purpose, a cycle is split into 16 different states and measurement of each parameter is attributed to one or more of these. In each state, one out of four different settings for the multi-beam-switcher is loaded. An overview of a measurement cycle including the duration of various states is given in table 5.1. Stable isotope currents are only injected for very short times, most of the measurement time is dedicated to the rare isotope. The length of the state used for measurement of $^{37}\text{Cl}^{7+}$ is adjusted automatically for each target according to the current in MFC-04-3 to allow a reliable measurement.

| state # | duration [ms] | MBS settings | task |
|---------|---------------|-----------------------------------|---|
| 1 | 0.05 | injection ^{35}Cl (reg0) | switching masses |
| 2 | 0.15 | injection ^{35}Cl (reg0) | curr. measurement $^{35}\text{Cl}^{7+}$ |
| 3 | 0.05 | injection ^{35}Cl (reg0) | switching masses |
| 4 | 0.05 | injection ^{37}Cl (reg1) | switching masses |
| 5 | 0.15 – 3 | injection ^{37}Cl (reg1) | curr. measurement $^{37}\text{Cl}^{7+}$ |
| 6 | 0.05 | injection ^{37}Cl (reg1) | switching masses |
| 7 | 0.05 | ^{35}Cl to LE-cup (reg2) | switching masses |
| 8 | 0.15 | ^{35}Cl to LE-cup (reg2) | curr. measurement $^{35}\text{Cl}^-$ |
| 9 | 0.05 | ^{35}Cl to LE-cup (reg2) | switching masses |
| 10 | 5 | injection ^{36}Cl (reg3) | switching masses |
| 11&12 | 100 | injection ^{36}Cl (reg3) | counting $^{36}\text{Cl}^{7+}$ and $^{36}\text{S}^{7+}$ |
| 13–16 | 0.0005 | injection ^{36}Cl (reg3) | not used |

Table 5.1: Measurement cycle for ^{36}Cl at VERA and the duration of states used for measurement of various parameters. The length of state 5 was automatically adjusted according to the sensitivity range of the respective SRS-amplifier to allow a reliable measurement of $^{37}\text{Cl}^{7+}$ currents in the nA as well as in the μA range depending on the $^{35}\text{Cl}/^{37}\text{Cl}$ ratio of the sample.

A typical run on a sample consists of 1500–3000 cycles and lasts 5–10 minutes. After changing to a new sample, the sensitivities of the SRS-amplifiers connected to the Faraday cups are adjusted according to the measured currents. This takes only several seconds after which data acquisition is started. The measurement order of samples is not necessarily the order in the target wheel but can be defined in the control file. This is important to minimize the effects of cross contamination and memory effect in the ion source (see section 6.3.1). Automatic retuning of single parameters like the target wheel position is also possible but only used for very small targets (cf. section 4.1.3). The number of runs on a specific sample can also be set in the control file, usually only one run is performed per wheel turn.

Prior to the regular measurement and the first sputtering of ^{36}Cl rich materials, over 2 million ^{36}S events are recorded to determine the sulfur suppression factor for data evaluation (cf. section 3.3.4). Next, all samples are presputtered until the initially high ^{36}S count rate drops below 3 kHz, which typically happens within 5 min. The maximum presputtering time per sample is 15 min. In the rare case that a sample still exhibits ^{36}S count rates above 10 kHz after presputtering, it is excluded from automated measurement and later measured separately at lower beam current.

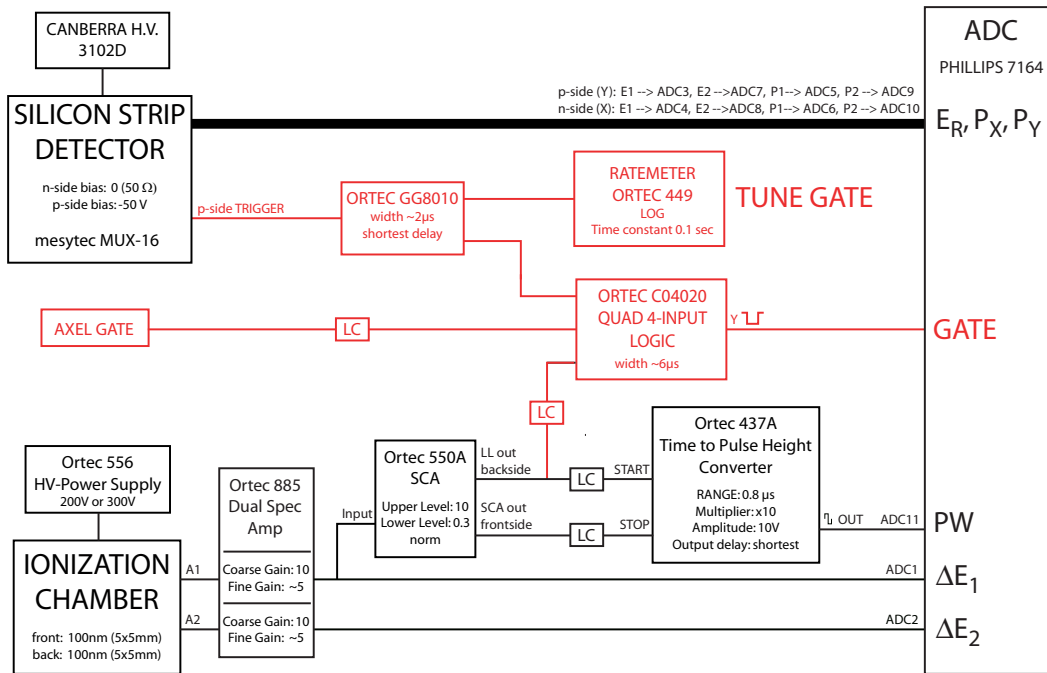


Figure 5.2: Data acquisition electronics for the detection setup. The red components are for the generation of the gate signals. LC stands for level converter. For each event producing a gate signal, two differential energy loss signals (ΔE_1 , ΔE_2), a pulse width signal (PW), two redundant residual energy signals (E_R) and two position signals (P_X , P_Y) are recorded.

After each run, the collected data is submitted to an evaluation server. In each measurement sequence for counting of the rare isotope ^{36}Cl , all events producing a gate signal are recorded and no prior discrimination of ^{36}S is made. This allows for complete post-measurement analysis of the data and later optimization of the ^{36}Cl region of interest, as will be described in one of the next sections. The data acquisition electronics for the detection setup is shown in figure 5.2. The individual signals from the ionization chamber and the silicon strip detector are discussed in detail in chapter 3. The red elements produce the gate signal that triggers conversion of the 11 channels of the ADC. The AXEL-GATE is a status signal from the accelerator control system that all components like the multi-beam-switcher were set for measurement of ^{36}Cl . If this status signal is "ready", the electronics allows the ADC to be triggered by either the silicon strip detector or the ionization chamber. Triggering on both detectors is required to record all information since the signals from the silicon strip detector arrive $3\text{ }\mu\text{s}$ earlier than those of the ionization chamber, but not all ions pass the exit window aperture. The quite long gate width of $6\text{ }\mu\text{s}$, during which the ADC watches for the maximum peak height, is necessary to collect also the pulse width signal. This signal comes only after the ΔE_1 signal has fallen below 10 % of its height. Concerning dead time, the length of the gate signal is still small compared to the $\sim 20\text{ }\mu\text{s}$ conversion time of the ADC.

5.3 Reference materials

The primary reference material used for the normalization of measurement results at VERA is the *K-381/4N* standard from the ETH Zurich with a nominal $^{36}\text{Cl}/\text{Cl}$ ratio of $(1.714 \pm 0.006) \times 10^{-11}$, which was recently cross-calibrated against other ^{36}Cl standard materials [116]. In the course of this work, it became clear that reference materials with lower $^{36}\text{Cl}/\text{Cl}$ ratios are needed to avoid cross contamination in the ion source (see section 6.3.1). For this reason, we produced a series of inhouse standards by stepwise dilution of a ^{36}Cl standard solution with a nominal ^{36}Cl ratio of 10^{-10} provided by the GAMS group at the TU Munich. A similar procedure has been used in [58]. The blank material was NaCl from Alfa Aesar (Sodium chloride, Puratronic®, with a purity of 99.999 %, Art# 10862, [105]) suspended in distilled water to a concentration of 15 g/l. The dilution series covers isotopic ratios from 10^{-11} to 3×10^{-16} and about 15–45 ml per standard solution with concentrations of NaCl of $\sim 15\text{ g/l}$ were produced.

These inhouse standards were calibrated in several beamtimes against *K-381/4N*. Initially calculated $^{36}\text{Cl}/\text{Cl}$ values of the dilution series turned out to be wrong due to a deviation of the initial concentration of the primary solution from the nominal value. This is probably the cause for the $\sim 25\text{ }\%$ offset of VERA's earlier ^{36}Cl results reported in [58]. Isotopic ratios of the dilution series and the produced quantities are shown in table 5.2. Especially the *DiluSeII*-standard solution with a $^{36}\text{Cl}/\text{Cl}$

| name | amount [ml] | # AMS samples | calibrated $^{36}\text{Cl}/\text{Cl}$ |
|-------------------|-------------|---------------|---|
| <i>DiluSeI</i> | 15 | ~ 140 | $(1.194 \pm 0.008) \times 10^{-11}$ (meas.) |
| <i>DiluSeII</i> | 42 | ~ 390 | $(1.236 \pm 0.009) \times 10^{-12}$ (meas.) |
| <i>DiluSeIII</i> | 20 | ~ 190 | $(3.627 \pm 0.082) \times 10^{-13}$ (meas.) |
| <i>DiluSeIV</i> | 16 | ~ 150 | $(1.310 \pm 0.034) \times 10^{-13}$ (meas.) |
| <i>DiluSeV</i> | 20 | ~ 190 | $(3.63 \pm 0.23) \times 10^{-14}$ (meas.) |
| <i>DiluSeVI</i> | 16 | ~ 150 | $(1.52 \pm 0.22) \times 10^{-14}$ (meas.) |
| <i>DiluSeVII</i> | 20 | ~ 190 | $(3.1 \pm 1.0) \times 10^{-15}$ (meas.) |
| <i>DiluSeVIII</i> | 16 | ~ 150 | 1.32×10^{-15} (calc.) |
| <i>DiluSeIX</i> | 20 | ~ 190 | 3.63×10^{-16} (calc.) |

Table 5.2: List of the inhouse standards produced by stepwise dilution of a solution with $^{36}\text{Cl}/\text{Cl} \approx 10^{-10}$. They are all NaCl suspended in bi-distilled water with a concentration of 15 g/l. The corresponding number of AMS samples was calculated based on the amount of NaCl in the solution assuming ~ 4 mg AgCl per sample. The measured values were calibrated against $K-381/4N$. The uncertainties include both the measurement uncertainties as well as the uncertainty of the nominal value of $K-381/4N$. The low ratio solutions *DiluSeV*, *DiluSeVI* and *DiluSeVII* have only been measured in one beamtime, hence the quite large uncertainty. The two lowest standards have not been measured so far and only calculated values are listed.

ratio of $(1.236 \pm 0.009) \times 10^{-12}$ turned out to be a good compromise between low cross contamination and ample counting statistics. Typical AMS samples of this material have a low sulfur output of $^{36}\text{S}/^{35}\text{Cl} \approx 5 \times 10^{-11}$. *DiluSeII* has already been successfully used as reference material in several beamtimes including the exposure dating measurements described in section 6.5 and it will be used as the main reference material in future ^{36}Cl measurements at VERA. The available quantity corresponds to roughly 400 AMS samples, which is sufficient for at least 100 beamtimes. For samples with expected $^{36}\text{Cl}/\text{Cl}$ ratios below 10^{-14} , a set of *DiluSeIV* standards is also mounted and used during measurement to avoid cross contamination. In this case, the *DiluSeII* samples are only sputtered if some of the unknown samples exhibit similarly high $^{36}\text{Cl}/\text{Cl}$ ratios. In one of the exposure dating measurements, additional standard materials from the Helmholtzzentrum Dresden-Rossendorf were used.

5.4 Data evaluation

Routine measurements of ^{36}Cl of course require a reliable and work efficient data evaluation. The coming sections describe our approach for ^{36}Cl data analysis and the underlying considerations. Recording of the complete set of measurement parameters for all events including the ^{36}S events allows for full post-measurement analysis

of the data. This is especially important for samples with a very low $^{36}\text{Cl}/\text{Cl}$ ratio, as described in the coming sections, but also samples with ample ^{36}Cl benefit significantly. A preliminary data evaluation by an automated data evaluation program is used to monitor the AMS measurement. Fine-tuning of the data evaluation including correction of the data for several effects is then made after the measurement. All raw data is stored on a server and can be retrieved at any time for reevaluation.

5.4.1 Defining the ^{36}Cl region of interest

In order to discriminate between ^{36}Cl and ^{36}S events in the course of data evaluation, regions of interest are set in the spectra recorded with the detection setup and all events fulfilling the conditions are counted as the respective isotopes. A wide region of interest is of course desirable to achieve a high efficiency, nevertheless the ^{36}Cl region of interest has to be tight enough to reduce the contribution of ^{36}S events and ensure sufficient sulfur suppression. Therefore, these regions of interest are determined by comparison of the spectra from a sulfur rich material without ^{36}Cl with those from a reference material with a distinct ^{36}Cl peak.

The "pure" sulfur data is always collected right after tuning to avoid cross contamination from ^{36}Cl rich materials as described in section 3.3.4. The precise determination of the ^{36}Cl region of interest is preferably done with the spectra from a reference material with a $^{36}\text{Cl}/\text{Cl}$ ratio around or above 10^{-12} . Due to the possibility of complete post-measurement data evaluation, there is however no need to sputter this reference material prior to the unknown samples. To minimize the risk of cross contamination of the unknown samples, the data from the ^{36}Cl rich material is thus usually collected at the end of the measurement, unless the unknown samples have high $^{36}\text{Cl}/\text{Cl}$ ratios anyway. In any case, a preliminary ^{36}Cl region of interest based on results from 10^{-13} -samples is sufficient for a rough online evaluation of ^{36}Cl ratios and control of the AMS measurement.

With our detection setup, six parameters are recorded for each event (for details see chapter 3): two differential energy losses in the ionization chamber (ΔE_1 , ΔE_2), the pulse width of the first energy loss signal (PW), the residual energy in the silicon strip detector (E_R) and the final position (P_X , P_Y). Since the latter two provide no information for the separation of ^{36}Cl and ^{36}S (cf. section 3.5.3), each region of interest should be a 4-dimensional ellipsoid. In practice, bins are set on each individual parameter and in two 2-dimensional projections.

First, pile-up events are rejected by setting a bin on the pulse-width signal. For ^{36}S , the region of interest is set by a rectangle in the ΔE_1 - ΔE_2 spectrum without any further conditions. The ^{36}Cl region of interest is more sophisticated and determined by stepwise improvement of boundaries in the ΔE_1 - ΔE_2 spectrum and the $(\Delta E_1 + \Delta E_2)$ - E_R spectrum. The latter is chosen since the isobars are best separated in the total energy loss signal from the ionization chamber. By setting a bin on the E_R -signal, only events, which pass the exit window of the ionization chamber and

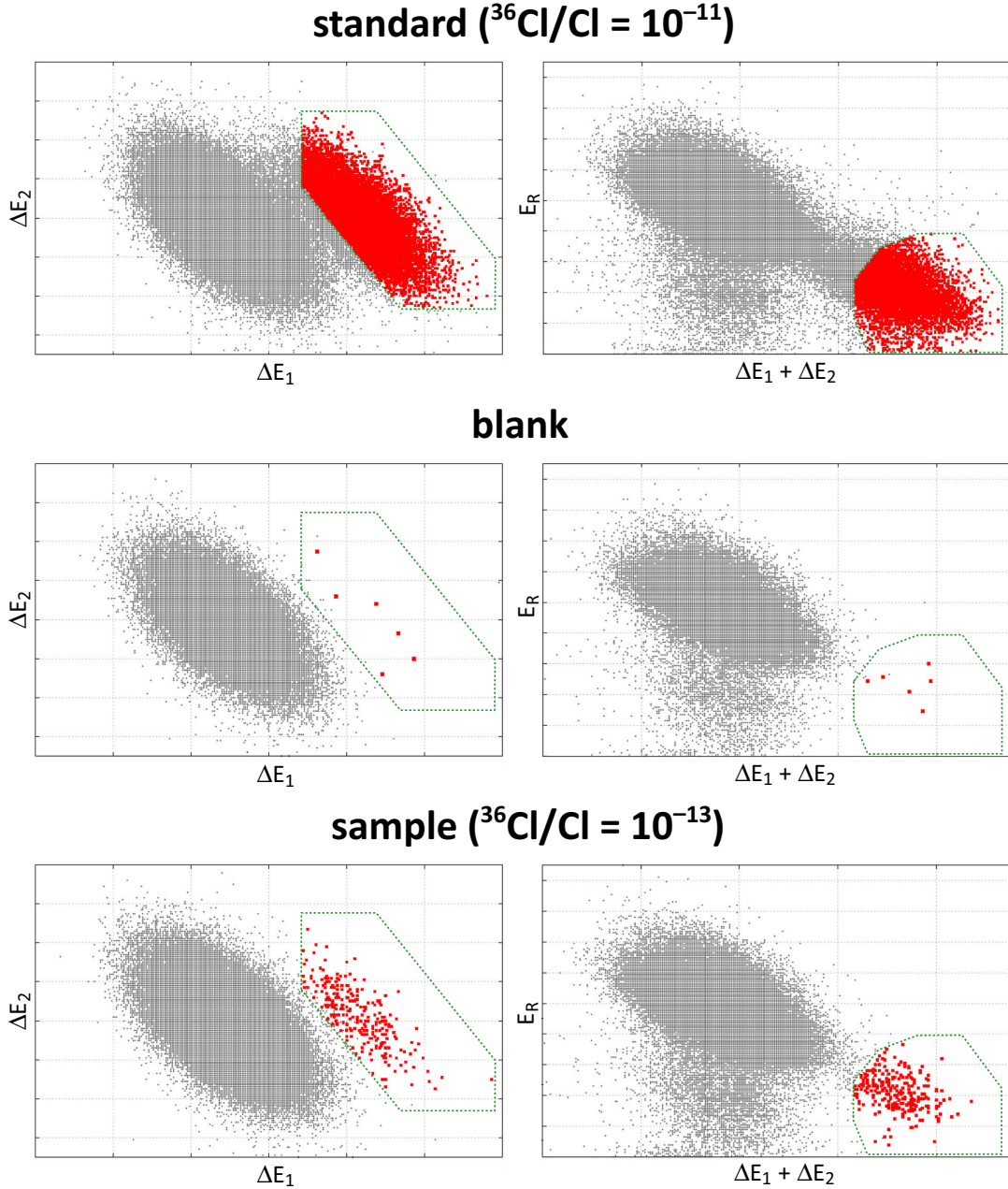


Figure 5.3: Sample spectra recorded on three different AgCl samples. Only ions that produced a signal in the silicon strip detector and passed the pulse width criteria are plotted. ΔE_i are the energy loss signals from the two anodes of the ionization chamber and E_R is the residual energy signal from the strip detector. The green dotted line shows the ^{36}Cl region of interest. All events (mostly sulfur) are plotted in gray and the events finally accepted as ^{36}Cl are plotted in red. The 6 counts on the blank sample correspond to a normalized background of $^{36}\text{Cl}/\text{Cl} \approx 4 \times 10^{-15}$ (prior to sulfur-induced background correction).

produce a signal in the silicon strip detector, are accepted. The final ^{36}Cl region of interest is chosen such that the number of ^{36}Cl counts on the reference material is maximized under the condition that the number of sulfur events misinterpreted as ^{36}Cl (monitored via the sulfur rich material) is as low as possible. The general shape of the bins is of course the same in all measurements. Sample spectra from 3 materials are shown in figure 5.3. The ^{36}Cl region of interest is set loosely around the ^{36}Cl peak except for very tight conditions on the side bordering the ^{36}S peak.

5.4.2 The peak drift correction

For decent isobar suppression, the ^{36}Cl region of interest needs to be very tight where it borders the sulfur peak, as shown in the previous section. Since $\sim 30\%$ of the ^{36}Cl events are cut away, drifts in the spectra caused by electronics or changes in the detector gas can thus easily change the detector efficiency and deteriorate precision. Even with the ionization chamber filled and closed completely, we typically observe drifts in the spectra of at least 2 channels (3%) per day. Therefore we implemented a special drift correction where the position of the ^{36}S peak, which is much more pronounced than the ^{36}Cl peak, is continuously evaluated and all energy loss spectra are shifted accordingly prior to bin evaluation. Thereby, the precision on a single sample is improved by roughly a factor of 2. Usually, the sulfur peak position is evaluated for each block of 10 000 events, which corresponds to roughly 20 seconds of measurement time at typical ^{36}S count rates. Data from bad cycles, which were identified by the automated evaluation program due to irregularities in stable isotope currents or the machine setup, are automatically excluded from the peak shift and further data evaluation.

The limitations of this method were tested by operating the detector with gas through-flow and our pressure regulation, which achieves a constant pressure within 1%. The results are shown in figure 5.4. The pressure fluctuations caused by the regulator lead to drifts in the uncorrected spectra of ± 4 channels within 100 s. With the drift correction enabled, the peak positions are stable with a deviation of less than ± 0.5 channels. This clearly demonstrates how the drift correction can even compensate short fluctuations in the spectra making it an important tool to achieve good overall precision.

5.4.3 Turnwise evaluation and applied corrections

After peak drift correction, the number of events in the respective regions of interest are evaluated and compared to the acquired stable isotope charges for each run. The dead time of the detection system is calculated from the total number of events and automatically corrected for. Parts of the runs, where stable isotope currents were out of range of the SRS-amplifiers or showed strange behaviors like steps or strong slopes, are excluded from this evaluation. For each run, the following parameters are

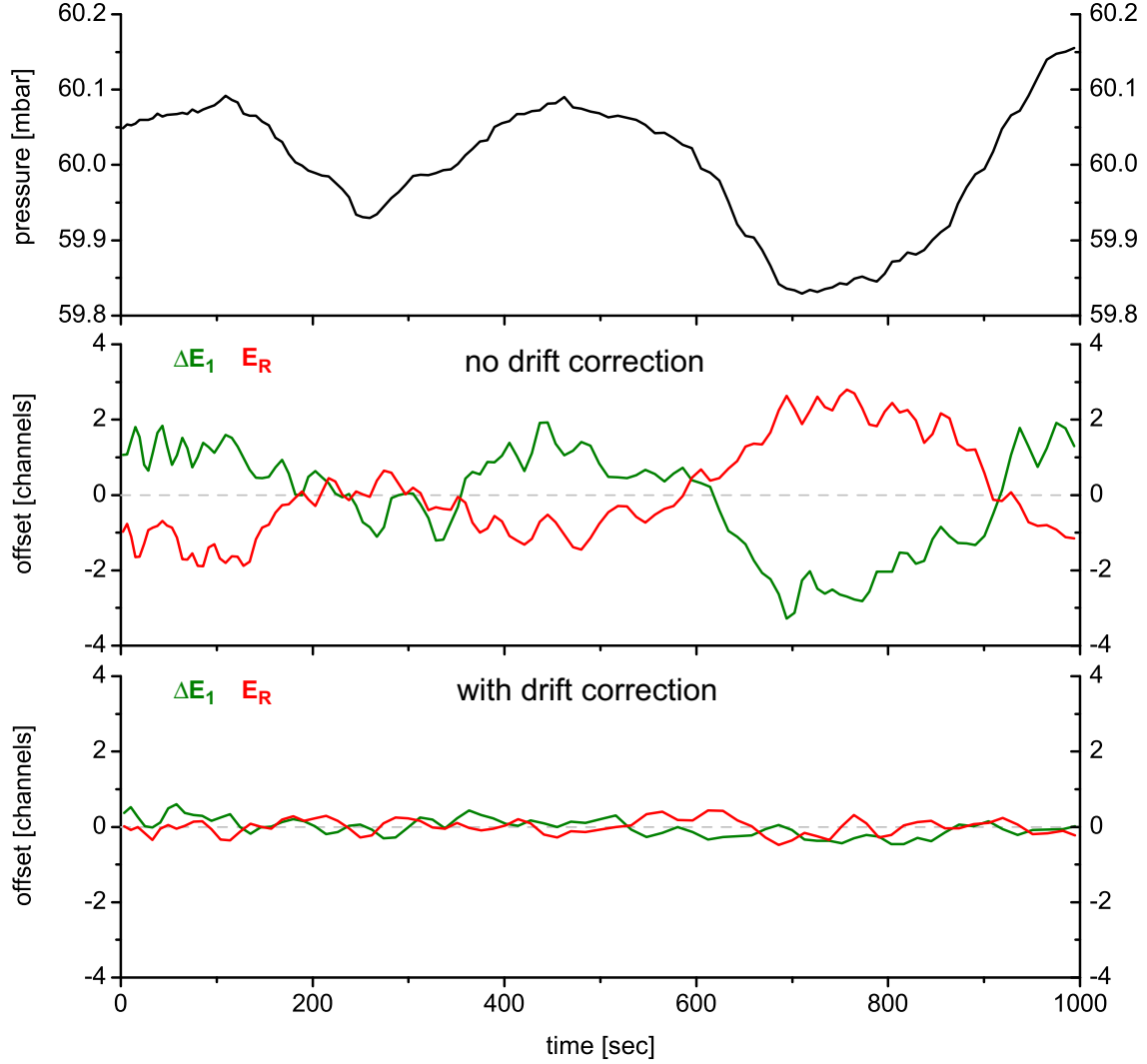


Figure 5.4: Drift of the position of the sulfur peak in the energy loss spectra over time with and without peak drift correction. The upper graph shows the intentionally unstable pressure in the ionization chamber over 1000s. The latter two graphs show the respective drift of the sulfur peak position both for the ΔE_1 signal from the ionization chamber and the residual energy signal from the silicon strip detector E_R . Positive offset corresponds to higher energy loss, thus ΔE_1 and E_R offsets are anticorrelated. Apparently, the drift correction can compensate even for fast drifts and significantly enhances precision of the measurement.

handed over to a second, semi-automated ^{36}Cl data evaluation program: the number of events identified as ^{36}Cl ($N_{36\text{Cl}}$), the number of ^{36}S events ($N_{36\text{S}}$), the total number of events in the ionization chamber (N_{IC}), the total number of events in the residual energy detector (N_{ER}), the dead time corrected measurement time (t), the average $^{35}\text{Cl}^-$ current (LE35CL), the average $^{35}\text{Cl}^{7+}$ current (HE35Cl), the average $^{37}\text{Cl}^{7+}$ current (HE37Cl), the run number and the wheel turn number.

The ^{36}Cl data evaluation program checks if all necessary information is available and marks corrupted runs. It also allows to set an upper limit for the sulfur content in the ion beam, runs with higher $^{36}\text{S}/^{35}\text{Cl}$ ratios are neglected. This ensures that data, which has been collected once a whole has been sputtered through the AgCl layer, is rejected and does not distort the final results. Likewise, upper and lower limits for the $^{35}\text{Cl}^-$ current or the run number are optional. Next, an additional parameter identifying each sample as a reference, blank or unknown material has to be assigned. The sulfur suppression factor (SSF) is calculated by comparison of $N_{36\text{Cl}}$ and $N_{36\text{S}}$ in the initial runs on a sulfur rich material (cf. section 3.3.4).

The ^{36}Cl data evaluation program then performs the automated steps described below. For the calculation of weighted mean values \bar{x} , the program uses the uncertainties of the individual results σ_i as weights. For the uncertainty of the weighted mean value $\sigma_{\bar{x}}$ it uses the maximum of internal and external uncertainty.

$$\bar{x} = \frac{\sum_i \frac{x_i}{\sigma_i^2}}{\sum_i \frac{1}{\sigma_i^2}} \quad \sigma_{\text{int } \bar{x}} = \frac{1}{\sqrt{\sum_i \frac{1}{\sigma_i^2}}} \quad \sigma_{\text{ext } \bar{x}} = \sqrt{\frac{\sum_i \frac{(x_i - \bar{x})^2}{\sigma_i^2}}{(N-1) \cdot \sum_i \frac{1}{\sigma_i^2}}} \quad (5.1)$$

First, the sulfur induced background is subtracted from the measured number of ^{36}Cl events for each run. The sulfur induced background is proportional to the number of sulfur events in this run and calculated based on the sulfur suppression factor:

$$N_{36\text{Cl corr}} = N_{36\text{Cl}} - N_{36\text{S}} \cdot \text{SSF}, \quad \sigma_{36\text{Cl corr}} = \sqrt{N_{36\text{Cl}} + N_{36\text{S}} \cdot \text{SSF} + 1} \quad (5.2)$$

The corrected $^{36}\text{Cl}/^{35}\text{Cl}$ ratios from one wheel turn are then normalized according to the normalization factor (NF) calculated from the weighted mean of the measured sulfur-corrected $^{36}\text{Cl}/^{35}\text{Cl}$ values of the reference samples in this turn.

$$(^{36}\text{Cl}/^{35}\text{Cl})_{\text{norm}} = (^{36}\text{Cl}/^{35}\text{Cl})_{\text{corr}} \cdot \text{NF} \quad \text{with } \text{NF} = \frac{(^{36}\text{Cl}/^{35}\text{Cl})_{\text{nom REF}}}{(^{36}\text{Cl}/^{35}\text{Cl})_{\text{corr REF}}} \quad (5.3)$$

The uncertainty of the normalization factor for each turn is calculated from the uncertainty of the weighted mean of the sulfur-corrected $^{36}\text{Cl}/^{35}\text{Cl}$ ratios from the reference material. The small uncertainty of the nominal value (cf. section 5.3) can usually be neglected.

$$\sigma_{\text{NF}} = \text{NF} \cdot \frac{\sigma_{(^{36}\text{Cl}/^{35}\text{Cl})_{\text{corr REF}}}}{(^{36}\text{Cl}/^{35}\text{Cl})_{\text{corr REF}}} \quad (5.4)$$

This turnwise normalization ensures that slow changes of the beam transport efficiency on the high energy side between different turns do not deteriorate the overall precision when averaging results over the whole beamtime.

Next, a weighted mean of the normalized $^{36}\text{Cl}/^{35}\text{Cl}$ values from all runs on a specific sample is calculated. Experience has shown that slight differences in the shapes of the AgCl samples also have to be corrected for since they cause small variations in the transmission through the detection setup. Therefore, the transmissional losses in the detection setup are determined for each sample by comparison of the sum of events in the respective detectors (N_{IC} and N_{ER}). Small deviations of individual detector transmissions (DT) from the average detector transmission of the reference materials are corrected for in the following way.

$$(^{36}\text{Cl}/^{35}\text{Cl})_{\text{effcorr}} = \overline{(^{36}\text{Cl}/^{35}\text{Cl})}_{\text{norm}} \cdot \frac{\overline{\text{DT}}_{\text{REF}}}{\text{DT}} \quad \text{with } \text{DT} = \frac{\sum N_{\text{ER}}}{\sum N_{\text{IC}}} \quad (5.5)$$

The detector transmission (DT) for each sample bears no significant uncertainty due to the sheer number of recorded events for each sample. Finally, an average $^{36}\text{Cl}/^{35}\text{Cl}$ blank value is calculated as the weighted mean over all blank samples and subtracted from the results of unknown samples.

6 Performance and results

This chapter discusses the main characteristics of ^{36}Cl measurements at VERA including detection efficiency, reproducibility and background values and compares them to other facilities. Furthermore, results from the first ^{36}Cl exposure dating measurements at 3 MV terminal voltage are presented.

6.1 Efficiency

The overall detection efficiency for ^{36}Cl is an important parameter since it directly relates to the amount of sample material required for a reliable measurement and thus determines the effort in chemical sample preparation. With limited source output current, the efficiency also influences the necessary data acquisition time per sample. The overall detection efficiency for ^{36}Cl at VERA is $\sim 1\%$ and comprises the negative

| | |
|---|--------------|
| negative ionization yield | $> 11\%$ |
| terminal transmission and yield for 7+ charge state | 16 % |
| transport efficiency through mass spectrometers | $\sim 100\%$ |
| detector efficiency for ^{36}Cl | $\sim 50\%$ |
| overall detection efficiency for ^{36}Cl | $> 0,88\%$ |

Table 6.1: Overall detection efficiency for ^{36}Cl at VERA and its individual contributions. Since no additional degrader foil is used, the overall beam transport efficiency from the injector to the detector is 16 %.

ionization yield, the terminal transmission and charge state yield and the detector efficiency for ^{36}Cl , as shown in table 6.1. The negative ionization yield for 3 mg AgCl samples was measured to be above 11 – 13 %. This number is only a lower limit since not all of the sample material can be used up in a measurement. Once a hole has been sputtered through the AgCl layer, the high ^{36}S count rate from the backing material makes further data acquisition impossible. Fortunately, we do not observe cratering similar to other materials like graphite on the AgCl targets. Despite a proper focussing of the Cs-sputter-beam, only a broad shallow dimple slowly evolves with time and it takes long sputtering times to produce a hole in the AgCl layer. We attribute this behavior to local melting of the AgCl on the AgBr-backing.

The highest losses of the ion beam are introduced by selection of the 7+ charge state after terminal stripping. With $2.6 \mu\text{g}/\text{cm}^2$ carbon foils produced by laser ablation [60], the yield for the 7+ charge state at 3 MV terminal voltage is 16 %. The transport efficiency through the two mass spectrometers is almost 100 %. Since no additional degrader foil in front of the detection setup is necessary due to the low sulfur content of the ion beam (cf. chapter 4), the overall beam transport efficiency is 16 % and compares well to other facilities (cf. section 6.4). The detector efficiency of 50 % for ^{36}Cl includes the transmissional losses in the detection setup, which occur mainly at the exit window aperture of the ionization chamber (for details see chapter 3), as well as the losses due to a tight ^{36}Cl region of interest in data evaluation (cf. section 5.4.1).

6.2 Precision and accuracy

Several systematic studies have been performed to determine the precision and accuracy of ^{36}Cl results from VERA. As shown in the following sections, reproducibility and accuracy of ^{36}Cl results are very competitive to other facilities.

6.2.1 Precision and reproducibility

Generally, the precision on a single cathode was significantly improved by the advances in data evaluation described in section 5.4.3, especially the drift correction and the turnwise evaluation. Furthermore, the reliable tuning procedure (cf. section 5.1) and the stabilization of source output by the ion source regulation (cf. section 4.2.1) also play an essential role. Since many of the systematic effects are either minimized or corrected for, the precision on a single cathode is now mostly limited by counting statistics. With turnwise evaluation and the drift correction enabled, high ratio samples with $^{36}\text{Cl}/\text{Cl} \geq 10^{-12}$ are typically measured to 0.8 % precision for a single cathode. However, systematic differences between samples (see below) still play a role and limit the overall reproducibility to $\sim 2\%$. Figure 6.1 summarizes our reproducibility as a function of $^{36}\text{Cl}/\text{Cl}$ ratio. The reproducibility was derived from the standard deviation of the various results obtained for the same sample material in different beamtimes. All results were obtained on different sputter targets and normalized to the reference material for each beamtime. We consider this the best estimate of the accuracy of results on a single target of unknown sample material, provided that sufficient counting statistics is available.

For samples below $^{36}\text{Cl}/\text{Cl} \approx 3 \times 10^{-13}$, the reproducibility is mostly limited by the available acquisition time and counting statistics in a typical beamtime of 3 days for a 40 sample wheel. On average, the measurement time per target is 1.5 h but adjusted according to the isotopic ratios. For very low ratio samples ($^{36}\text{Cl}/\text{Cl} < 10^{-14}$) the uncertainty of sulfur induced background correction starts to play a role as well.

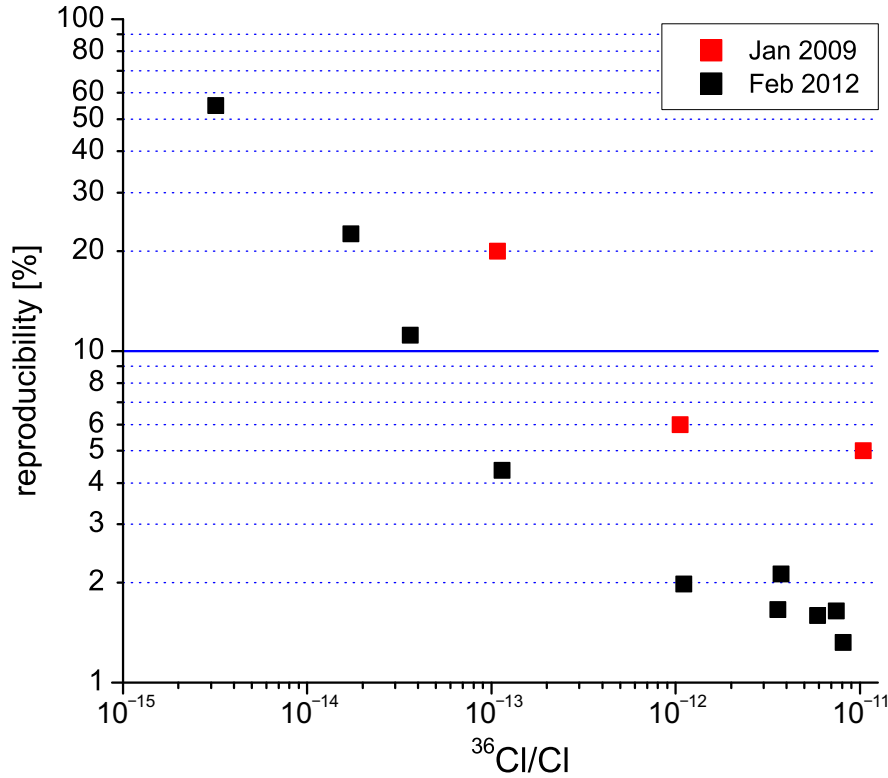


Figure 6.1: Reproducibility of ^{36}Cl measurement results including sulfur induced background correction for various $^{36}\text{Cl}/\text{Cl}$ ratios. All samples plotted have been measured at least in five cathodes and in different beamtimes. For high ratio samples, reproducibility is now around 2 % and limited by systematic uncertainties (see also figure 6.2). For low ratio samples, counting statistics usually limits the precision. Looking at the reproducibility in the earliest beamtime (plotted in red) the progress made in the course of this work is also reflected in enhanced precision of ^{36}Cl results.

For high ratio samples, the reproducibility is, as mentioned above, limited to $\sim 2\%$ due to slight systematic discrepancies between various cathodes containing the same sample material. These differences probably originate from minor variations in the shape of the pressed AgCl , which are suspected to cause small transmissional losses at the detector entrance window aperture. While the correction for differences in the detector transmission (see section 5.4.3) during data evaluation reduces this problem, the scatter of measurement results from samples of the same material is not completely eliminated. The reduced χ^2 of a large set of samples typically lies slightly above 2. Figure 6.2 shows the long-term stability of our Cl -measurements over several beamtimes. Apart from the described discrepancies between various cathodes, there is no statistically relevant offset between the normalized results of different beamtimes.

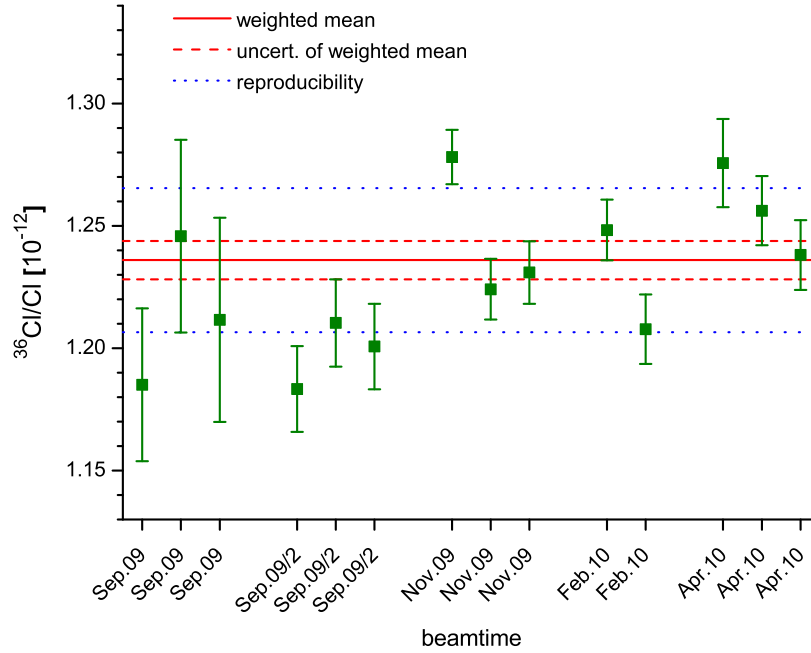


Figure 6.2: Comparison of 14 measurement results (already normalized to the reference material) for one sample material from several cathodes and beamtimes. The red line shows the weighted mean value, the red dashed line the standard deviation of the weighted mean calculated from the individual uncertainties and the scatter of results. The blue dotted line shows the reproducibility. The scatter between different cathodes in one beamtime is usually larger than the uncertainties on the single cathodes would suggest, the corresponding reduced χ^2 is 1.87. This is probably due to different shapes of the pressed AgCl targets and limits the reproducibility. There is no additional statistically significant offset between results of various beamtimes.

6.2.2 The ^{36}Cl round robin

The accuracy of ^{36}Cl results from VERA was demonstrated by taking part in a ^{36}Cl round robin intercomparison of several AMS labs [99]. Three different AgCl materials with $^{36}\text{Cl}/\text{Cl}$ ratios around 10^{-11} , 10^{-12} and 10^{-13} respectively were issued to 8 AMS laboratories. Preliminary results in the early stages of this work yielded that previous deviations of our results from others reported by [58] have been resolved and were mainly due to a wrong nominal value used for the standard material (cf. section 5.3). Since the AMS labs were given the chance to resolve initial discrepancies and update their ^{36}Cl results, the final results from VERA were obtained after implementation of most of the advances described within this work. Hence, not only the accuracy but also the uncertainties of our results now compare well with results from other labs, as shown in figure 6.3. Even for the 10^{-13} -sample, results from VERA are now competitive to other facilities.

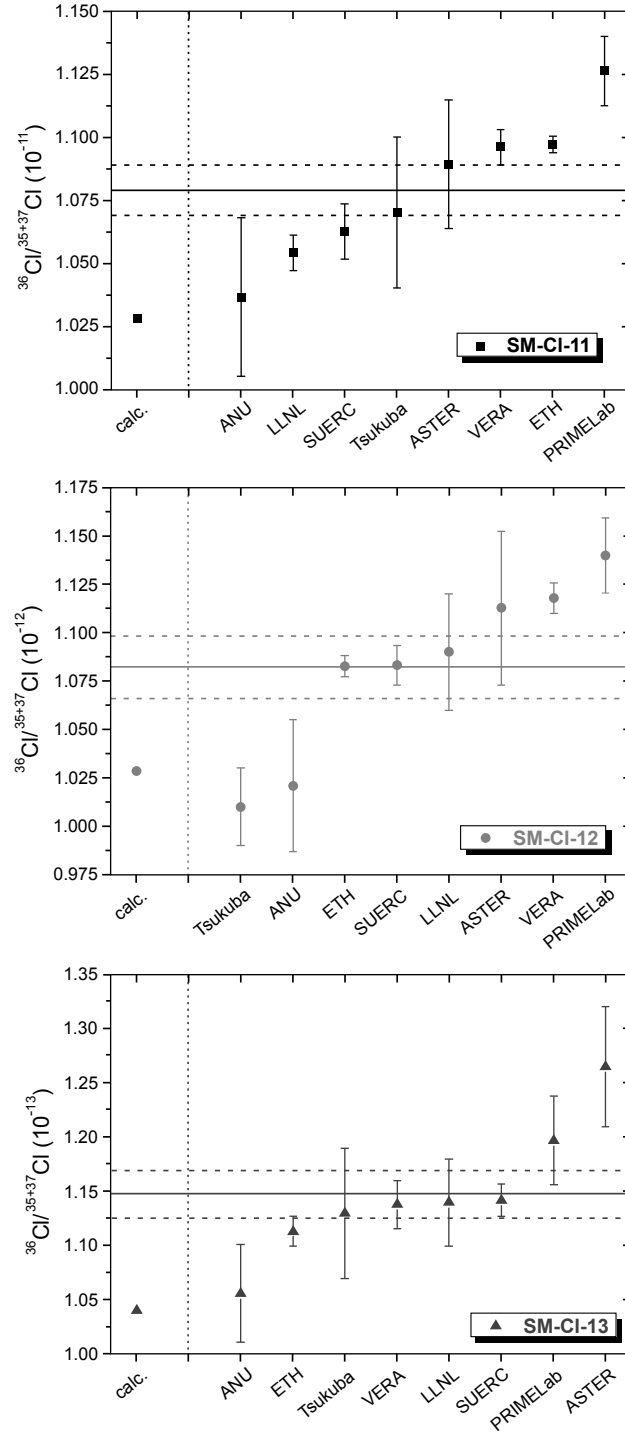


Figure 6.3: Comparison of ^{36}Cl results from 8 different laboratories in a ^{36}Cl round robin. Results from VERA are competitive to the other labs regarding accuracy and precision. The figures were taken from [99]. The solid line shows the mean value, the dashed lines indicate the standard deviation of the mean.

6.2.3 Cross calibration via the $^{35}\text{Cl}(n,\gamma)^{36}\text{Cl}$ cross section

Within the framework of the diploma thesis of Stefan Pavetich [117], the reference materials described in section 5.3 were cross-calibrated via the $^{35}\text{Cl}(n,\gamma)^{36}\text{Cl}$ reaction. Three NaCl-tablets were irradiated with thermal neutrons at the Budapest Research Reactor [118]. The neutron fluence was monitored with activity measurements of ^{198}Au and the established thermal cross section for $^{197}\text{Au}(n,\gamma)^{198}\text{Au}$. The $^{36}\text{Cl}/^{35}\text{Cl}$ ratios were then calculated via the well known thermal neutron capture cross section $^{35}\text{Cl}(n,\gamma)^{36}\text{Cl}$. The results of this study are presented in table 6.2. AMS results and $(^{36}\text{Cl}/^{35}\text{Cl})_{n,\gamma}$ values calculated from irradiation data agree for all three samples and no statistically significant offset of AMS results was observed. This further demonstrates the accuracy of ^{36}Cl measurements at VERA and indicates that the nominal $^{36}\text{Cl}/\text{Cl}$ values of the reference materials were determined correctly.

| sample | $(^{36}\text{Cl}/^{35}\text{Cl})_{n,\gamma}$ [10^{-12}] | $(^{36}\text{Cl}/^{35}\text{Cl})_{\text{VERA}}$ [10^{-12}] | $\frac{(^{36}\text{Cl}/^{35}\text{Cl})_{\text{VERA}}}{(^{36}\text{Cl}/^{35}\text{Cl})_{n,\gamma}}$ |
|--------|--|---|--|
| BUD1 | 7.78 ± 0.19 | 7.75 ± 0.06 | 0.996 ± 0.025 |
| BUD2 | 10.48 ± 0.25 | 10.69 ± 0.07 | 1.020 ± 0.025 |
| BUD3 | 9.53 ± 0.23 | 9.79 ± 0.08 | 1.027 ± 0.026 |

Table 6.2: Results from the cross calibration of $^{36}\text{Cl}/\text{Cl}$ reference materials with neutron activated samples. Within uncertainties, AMS results from all three samples agree with the $(^{36}\text{Cl}/^{35}\text{Cl})_{n,\gamma}$ values calculated from neutron irradiation. The $(^{36}\text{Cl}/^{35}\text{Cl})_{\text{VERA}}$ values were normalized to the *K-381/4N* reference material.

6.3 Background

The machine background during ^{36}Cl measurements is a crucial parameter, which limits the abundance sensitivity. On the one hand, insufficient suppression of ^{36}S causes some events misinterpreted as ^{36}Cl , on the other hand the volatility of chlorine poses some problems in the ion source since ^{36}Cl ions can possibly originate from residual chlorine vapor of preceding samples. With an average $^{36}\text{S}/^{35}\text{Cl}$ ratio of 5×10^{-11} in the negative ion beam and a sulfur suppression factor of 20 000 (compare chapters 3 and 4), the sulfur induced blank value is $^{36}\text{Cl}/\text{Cl} \approx 2.5 \times 10^{-15}$. This background from fake ^{36}Cl events can be subtracted from the measurement results by a correction proportional to the number of ^{36}S events, for details see section 5.4.3. For samples with a significantly higher sulfur content, the interference from ^{36}S can be reduced by narrowing the ^{36}Cl region of interest. While this of course reduces the measurement efficiency, the sulfur suppression in the detection setup is increased significantly, e.g. to a suppression of $\sim 100\,000$ reducing the detector efficiency for

^{36}Cl from 50 % to 40 % (cf. figure 3.19). After sulfur-induced background correction, our average machine blank value from true ^{36}Cl counts now is $(5\pm5)\times 10^{-16}$, which compares well to other facilities. This low background value is the result of some investigations on the memory effect and the cross contamination in the ion source, which are discussed in detail in the next section.

6.3.1 Cross contamination and memory effect of the ion source

The memory effect of the ion source was first studied by periodic measurements on a set of blank samples. The results of this study are summarized in table 6.3.

| sample #0 at the beginning of the cycle | blank #1, sputtered 3 min after sample #0 ($^{36}\text{Cl}/\text{Cl}$) [$\times 10^{-15}$] | blank #5, sputtered 2 h after sample #0 ($^{36}\text{Cl}/\text{Cl}$) [$\times 10^{-15}$] |
|---|--|--|
| only ^{36}Cl blanks sputtered (initial value) | 0.4 ± 0.8 | 0.5 ± 0.9 |
| 10^{-12} reference material sputtered for 5 min | 2.5 ± 1.3 | 0.5 ± 1.0 |
| 10^{-11} reference material sputtered for 5 min | 14 ± 1 | 3 ± 1 |
| ^{36}Cl blank sputtered for 24 h (final value) | 3.0 ± 0.7 | 1.5 ± 0.5 |

Table 6.3: Cross contamination and memory effect of the ion source studied with periodic measurements on a set of ^{36}Cl blank samples. A reference material was sputtered prior to the set of blank samples. Results from the blank following directly after the reference material (blank #1) and from the last blank in the cycle (blank #5) are shown.

The average initial blank value after sulfur induced background correction was $^{36}\text{Cl}/\text{Cl} \approx (4\pm 8)\times 10^{-16}$. In the next step, a 10^{-12} reference material (*DiluSeII*) mounted at the opposite side of the sample wheel was sputtered for several minutes at the beginning of each measurement cycle. The observed memory effect of the ion source on the first blank sample (blank #1) was below 10^{-3} and after 30 min no more statistically significant increase of the blank value was observed. When sputtering a 10^{-11} reference material (*DiluSeI*), the blank value after sulfur induced background correction starts at $^{36}\text{Cl}/\text{Cl} \approx (1.4\pm 0.2)\times 10^{-14}$ and follows an almost exponential decrease with a time constant of ~ 60 min to a constant blank value of $^{36}\text{Cl}/\text{Cl} \approx (3\pm 1)\times 10^{-15}$.

After 24 hours of source "cleaning" on a new blank cathode, a second measurement series only on the blank samples yielded that, independent from the cathode positions, the first blank sample in the cycle (blank #1) still showed the highest cross contamination, $^{36}\text{Cl}/\text{Cl} \approx (3.0\pm 0.7)\times 10^{-15}$ compared to $^{36}\text{Cl}/\text{Cl} \approx (1.5\pm 0.5)\times 10^{-15}$

on the last sample in the cycle (blank #5). This effect can clearly not be explained by any build-up of a Cl reservoir in the ion source. In our understanding, Cl vapor from the samples also takes part in the sputtering process and therefore is implanted in the following target materials at a level of $\sim 10^{-4}$.

Later, these results were verified by a detailed look on data from natural chlorine samples with a $^{35}\text{Cl}/^{37}\text{Cl}$ ratio of 3.125 ± 0.030 [17] and from isotopically enriched materials with $^{35}\text{Cl}/^{37}\text{Cl} \geq 100$ used as carrier in the isotope dilution technique (cf. section 5.2). The use of stable isotope currents has the advantage that data acquisition is very fast and no long counting times as for low $^{36}\text{Cl}/\text{Cl}$ ratios are necessary. Hence, it is possible to resolve short-time effects. It should be noted that the following data was collected during routine ^{36}Cl measurements on exposure dating samples and only later used to study memory effect and cross contamination. While some additional insight may have been gained in a dedicated experiment, the recent results strengthen the conclusions from the previous experiment.

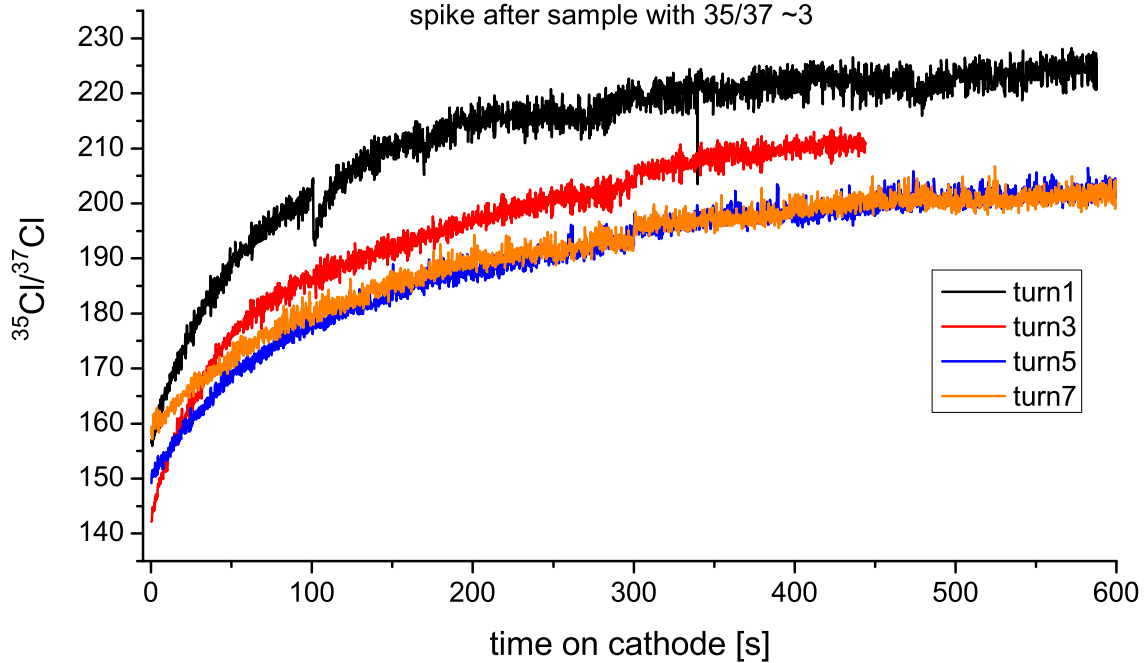


Figure 6.4: Study of memory effect and cross contamination in the ion source with the $^{35}\text{Cl}/^{37}\text{Cl}$ ratio. The figure shows the measured $^{35}\text{Cl}/^{37}\text{Cl}$ ratio from a ^{35}Cl enriched sample as function of sputter time for different wheel turns. The source memory effect from the preceding sample with a $^{35}\text{Cl}/^{37}\text{Cl}$ ratio of ~ 3 is apparent. Data acquisition started about 1 minute after sample change. The difference between results from various turns indicates some cross contamination or longterm memory effect.

Figure 6.4 shows the measured $^{35}\text{Cl}/^{37}\text{Cl}$ ratio as a function of sputter time for several wheel turns. The material was a ^{35}Cl enriched carrier with a $^{35}\text{Cl}/^{37}\text{Cl}$ ratio

of ≥ 230 . The sample sputtered directly before had the natural $^{35}\text{Cl}/^{37}\text{Cl}$ ratio of ~ 3.125 . The memory effect of the ion source is clearly visible for each new run. The amount of ^{37}Cl decreases quite strongly with sputter time for the first minutes and then reaches an almost constant level. The average $^{35}\text{Cl}/^{37}\text{Cl}$ ratio in the first wheel turn calculated from the collected charges is 189. Assuming that the $^{35}\text{Cl}/^{37}\text{Cl}$ value of 225 measured at the end of the run is close to the true value, the memory effect is $\sim 2.5 \times 10^{-3}$ within the first 10 minutes of sputtering. In consecutive turns, the $^{35}\text{Cl}/^{37}\text{Cl}$ at the end is somewhat lower indicating some permanent cross contamination of the sample. The change is strongest from the first to the second turn, after several turns some equilibrium is reached. Since the ion source was running on natural chlorine samples for more than 24 hours prior to these measurements, it is very unlikely that the observed change is caused by the build-up of a chlorine reservoir in the ion source. This suggests that cross contamination (including some memory effect, which decreases only with a time constant of several hours) is above 10^{-3} . Another set of measurements yields a contamination of the following sample of $\sim 4 \times 10^{-4}$. Again, no indications for a wheel-position-dependence of the cross contamination were observed.

Taking these effects into account, their influence can be mitigated by careful choice of the target order and the use of appropriate standard materials. As described in section 5.3, we now routinely use a reference material with $^{36}\text{Cl}/\text{Cl} \approx 1.2 \times 10^{-12}$ instead of 10^{-11} -reference materials to avoid cross contamination. For samples with expected $^{36}\text{Cl}/\text{Cl}$ ratios below 10^{-14} , a 10^{-13} -reference material is used during measurement. Since the memory effect of the ion source is about 2×10^{-3} within the first 10 minutes, the expected $^{36}\text{Cl}/\text{Cl}$ background is $\sim 2 \times 10^{-15}$ for the sample following the reference material. To further reduce the influence, we try to avoid measurements of low ratio samples directly after sputtering of reference material. For this purpose, we mount a "cleaning" sample with ^{36}Cl blank material into the wheel. The target order during measurement is then adjusted for increasing $^{36}\text{Cl}/\text{Cl}$ ratios during one wheel turn. Initially, the order is based on the expected isotopic ratios but can later be changed any time in the control file of the automated measurement. The "cleaning" sample is always sputtered as the first sample in the turn, hence right after the reference material or the sample with the highest $^{36}\text{Cl}/\text{Cl}$ ratio. In this way, the average measured $^{36}\text{Cl}/\text{Cl}$ blank value after sulfur-induced background correction now is $(5 \pm 5) \times 10^{-16}$.

Based on the $^{35}\text{Cl}/^{37}\text{Cl}$ results, a new strategy for the measurement of the $^{35}\text{Cl}/^{37}\text{Cl}$ ratios of isotope diluted ^{36}Cl samples will be adopted in the future. The $^{35}\text{Cl}/^{37}\text{Cl}$ measurements will be done prior to the actual measurement when presputtering the samples for reduction of ^{36}S output (compare section 5.2). To avoid cross contamination and reduce the memory effect, an additional sample of the carrier material will be mounted into the target wheel and sputtered following every sample with a low or natural $^{35}\text{Cl}/^{37}\text{Cl}$ ratio. This sample can later be used as a "cleaning" sample during ^{36}Cl measurement.

6.4 Comparison with other labs

Most of the performance data of VERA for ^{36}Cl compares well to those of larger facilities, as shown in table 6.4. The slightly lower sulfur suppression factor at 24 MeV is partly compensated for by the comparably low sulfur content in the ion beam. The average sulfur induced background of $\sim 2 \times 10^{-15}$ is usually no limitation during measurement and can be very well corrected for. Especially for samples with $^{36}\text{Cl}/\text{Cl}$ ratios $\geq 10^{-14}$, which constitute the majority of natural ^{36}Cl samples, AMS measurements at VERA are competitive to other facilities. Only for samples with $^{36}\text{Cl}/\text{Cl}$ ratios below 5×10^{-15} , additional sulfur suppression would be desirable. Here, larger facilities partly profit from higher isobar separation capabilities, although in many cases it is the ^{36}Cl background from memory effects of the ion source rather than the ^{36}S interference which limits the abundance sensitivity.

| | VERA | SUERC | ASTER | ETH | LLNL | ANU |
|---|-----------------|-----------------|---------------------|-------------------|---------------------|-----------------|
| energy [MeV] | 24 | 30 | 30 | 48 | 66 | 112 |
| degrader foil | no | no | yes | no | no | no |
| ^{36}S suppr. factor | 2×10^4 | 1×10^5 | 2.7×10^6 | 1.5×10^5 | 1×10^6 | 3×10^6 |
| beam transport efficiency [%] | 16 | ~ 20 | 2 | 15–20 | ~ 20 | 12–15 |
| ^{36}Cl detector efficiency [%] | 50 | ~ 50 | 55 | 70–80 | – | 100 |
| reproducibility on 10^{-12} samples [%] | 2 | < 3 | 1–2 | 2 | 3 | 3 |
| background $^{36}\text{Cl}/\text{Cl}$ | $< 10^{-15}$ | $< 10^{-15}$ | 3×10^{-16} | $< 10^{-15}$ | 3×10^{-15} | $< 10^{-16}$ |

Table 6.4: Comparison of measurement conditions and performance data of ^{36}Cl measurements at different AMS facilities, which are described in the following publications: SUERC [98], ASTER [119], ETH [80, 109], LLNL [120, 121] and ANU [112]. Apart from the listed references, several values were taken from [99] and private communication during the preparation of the manuscript. The beam transport efficiency includes all beam losses (including charge state yields) up to the detection setup.

One technique for additional sulfur suppression at VERA would be the use of a degrader foil like at ASTER. While it significantly reduces the interference from ^{36}S , it introduces quite high losses in chlorine beam resulting in only 2 % beam transport efficiency into the detector. This motivated the investigation of alternative techniques for additional isobar suppression described in chapter 7.

6.5 Measurement of exposure dating samples

Following the implementation of most of the developments described in previous chapters, several sets of natural ^{36}Cl samples were successfully measured at VERA. Results from the first two sets of ^{36}Cl exposure dating samples measured at 3 MV terminal voltage are presented in the next two sections. In both cases, sample preparation and interpretation of results was done by our collaborators and the final results will be published separately. Therefore, only the direct ^{36}Cl AMS results are discussed in the following to underline the reliability of ^{36}Cl measurements at VERA. Additionally, several beamtimes were dedicated to the measurement of ^{36}Cl samples from neutron-irradiated salt with expected $^{36}\text{Cl}/\text{Cl}$ ratios between 10^{-12} and 10^{-11} with the goal to determine the $^{35}\text{Cl}(n,\gamma)^{36}\text{Cl}$ cross section at stellar neutron energies. AMS results were very satisfying concerning the reproducibility of high ratio samples, for details about this project see [117].

6.5.1 The Lonar crater samples

The first set of ^{36}Cl exposure dating samples originated from the Lonar crater in India. The main aim of this project is to establish the age of the impact crater and to resolve the discrepancy between earlier results from thermoluminescence [122] or fission track dating [123] and recent $^{40}\text{Ar}/^{39}\text{Ar}$ dating [124]. While the first two yielded quite young ages around 12–62 ka, the latter technique indicates an age of 570 ± 47 ka. This age difference should in principle be easily distinguishable by ^{36}Cl exposure dating. The rock samples were collected by C. Koeberl (Department of Lithospheric Research, University of Vienna), coordination of the project and sample preparation were done by Y. Kashiv (Department of Physics, University of Notre Dame) in close cooperation with M. Paul (Racah Institute of Physics, Hebrew University). During sample preparation, an enriched ^{35}Cl carrier was used.

We received 11 AgCl samples including two chemistry blanks. The samples were then pressed at VERA following the procedure described in section 4.1.1. For many samples the yield in chemical sample preparation was quite low resulting in small amounts of AgCl. The AMS results are summarized in table 6.5. All measured $^{36}\text{Cl}/^{35}\text{Cl}$ ratios are around or below 5×10^{-13} . The smallest sample contained less than 0.5 mg AgCl but was measured to 17 % precision. The reference material in this beamtime was *DiluSeII* (cf. section 5.3), the normalized machine blank measured on our inhouse blank material was $^{36}\text{Cl}/\text{Cl} \approx (2.4 \pm 7.0) \times 10^{-16}$. While the sulfur content of the negative ion beam from machine blank and reference samples was $^{36}\text{S}/^{35}\text{Cl} \approx 2.5 \times 10^{-11}$, the average sulfur content from the natural samples was more than 10^{-10} .

Results from this measurement demonstrate that good ^{36}Cl data can be obtained even under "harsh" conditions with only very small amounts of sample material and a high sulfur content of the ion beam. Despite the high $^{36}\text{S}/^{35}\text{Cl}$ ratios, a precision

| sample | AgCl [mg] | $^{36}\text{S}/^{35}\text{Cl}$ | $^{36}\text{Cl}/^{35}\text{Cl}$ | precision [%] |
|---------|-----------|--------------------------------|-----------------------------------|---------------|
| LO 29 | 2 | 9.9×10^{-10} | $(1.21 \pm 0.11) \times 10^{-13}$ | 8.8 |
| LO 60D | 3 | 4.1×10^{-10} | $(4.85 \pm 0.55) \times 10^{-14}$ | 11.4 |
| LO 62 | 1.5 | 1.5×10^{-9} | $(1.75 \pm 0.19) \times 10^{-13}$ | 10.6 |
| LO 72 | 2 | 4.0×10^{-10} | $(6.42 \pm 0.72) \times 10^{-14}$ | 11.2 |
| LO 73 | 2 | 1.4×10^{-10} | $(1.96 \pm 0.25) \times 10^{-14}$ | 12.7 |
| LO 7 | 2 | 1.2×10^{-9} | $(2.44 \pm 0.42) \times 10^{-13}$ | 17.3 |
| LO 14 | ~ 1 | 2.0×10^{-9} | $(5.10 \pm 0.53) \times 10^{-13}$ | 10.3 |
| CF 6 | < 1 | 1.7×10^{-9} | $(5.07 \pm 0.36) \times 10^{-13}$ | 7.0 |
| CF 1 | < 0.5 | 2.5×10^{-9} | $(5.24 \pm 0.97) \times 10^{-13}$ | 18.5 |
| blank A | 1.5 | 2.8×10^{-10} | $(1.33 \pm 0.41) \times 10^{-14}$ | 30.7 |
| blank B | 5 | 1.4×10^{-10} | $(6.7 \pm 2.1) \times 10^{-15}$ | 30.9 |

Table 6.5: AMS results for the ^{36}Cl exposure dating samples from the Lonar impact crater. Due to the low yield in chemical sample preparation, the AMS samples contained comparably small amounts of AgCl and exhibited quite high sulfur contents. The $^{36}\text{Cl}/^{35}\text{Cl}$ results are already normalized to *DiluSeII*.

of 10 % was achieved on samples with a $^{36}\text{Cl}/^{35}\text{Cl}$ ratio in the low 10^{-14} range. For samples with higher $^{36}\text{Cl}/^{35}\text{Cl}$ ratios, even sulfur contents of $^{36}\text{S}/^{35}\text{Cl} > 10^{-9}$ did not hinder successful measurement. The calculation of exposure ages from these results is not yet finished.

6.5.2 Samples from the Anatolian Plateau

This set of ^{36}Cl samples was for exposure dating of carbonate rocks from the Central Anatolian Plateau. The aim of this project is to data fluvial terraces in the Kastamonu Basin in order to determine fluvial incision rates in this actively deforming region of the North Anatolian Fault [125]. The samples were collected and prepared by C. Yildirim (University of Potsdam and Deutsches GeoForschungsZentrum Potsdam) and T. Schildgen (Leibniz Center for Surface Processes and Climate Studies, University of Potsdam). The chemical sample preparation was done at the Helmholtzzentrum Dresden-Rossendorf under the supervision of S. Merchel (Ion Beam Analysis, Helmholtz-Institut Freiberg für Ressourcenmanagement).

We received 9 exposure dating samples and a chemistry blank, all prepared with an enriched ^{35}Cl carrier. Additionally we got two reference materials from the Helmholtzzentrum Dresden-Rossendorf (*SM-12*, *SM-13*). Sample pressing was done at VERA following the established procedures. Different from the samples of the Lonar project (see above), all exposure dating samples yielded at least 4 mg AgCl with the exception of the chemistry blank, from which less than 0.5 mg AgCl were

available. The average sulfur content of this set of samples was considerably lower than in the Lonar project and the $^{36}\text{Cl}/^{35}\text{Cl}$ ratios ranged from 10^{-13} to several 10^{-12} . Hence the sulfur-induced background plays only a negligible role and the precision is limited by counting statistics and systematic effects. The AMS results are summarized in table 6.6. The data in the table was normalized to our inhouse standard

| sample | # | $^{36}\text{S}/^{35}\text{Cl}$ | $^{36}\text{Cl}/^{35}\text{Cl}$ | precision [%] |
|---------|---|--------------------------------|-----------------------------------|---------------|
| TC01 | 1 | 1.1×10^{-10} | $(3.97 \pm 0.17) \times 10^{-13}$ | 4.4 |
| TC02 | 1 | 3.1×10^{-10} | $(1.83 \pm 0.04) \times 10^{-12}$ | 2.4 |
| TC03 | 1 | 1.2×10^{-10} | $(5.02 \pm 0.15) \times 10^{-13}$ | 2.9 |
| TC04 | 1 | 2.9×10^{-10} | $(2.42 \pm 0.06) \times 10^{-12}$ | 2.3 |
| TC05 | 1 | 5.3×10^{-10} | $(1.70 \pm 0.09) \times 10^{-13}$ | 5.6 |
| TC06 | 2 | 5.9×10^{-10} | $(6.62 \pm 0.10) \times 10^{-12}$ | 1.5 |
| TC07 | 1 | 2.1×10^{-10} | $(3.53 \pm 0.08) \times 10^{-12}$ | 2.2 |
| TC08 | 1 | 3.5×10^{-11} | $(2.36 \pm 0.05) \times 10^{-12}$ | 2.0 |
| TC09 | 1 | 2.4×10^{-11} | $(2.06 \pm 0.04) \times 10^{-12}$ | 2.1 |
| TC10 | 1 | 7.1×10^{-10} | $(6.19 \pm 0.10) \times 10^{-12}$ | 1.6 |
| TCblank | 1 | 6.4×10^{-10} | $(1.5 \pm 1.1) \times 10^{-14}$ | 73.6 |
| SM-12 | 3 | 6.0×10^{-11} | $(1.10 \pm 0.02) \times 10^{-12}$ | 2.0 |
| SM-13 | 3 | 5.2×10^{-11} | $(1.18 \pm 0.04) \times 10^{-13}$ | 3.8 |

Table 6.6: AMS results for the ^{36}Cl exposure dating samples from the northern margin of the Central Anatolian Plateau. For sample materials, which have been measured in more than one cathode, the weighted mean is listed. The $^{36}\text{Cl}/^{35}\text{Cl}$ results are already normalized to *DiluSeII*. The TCblank sample contained < 0.5 mg AgCl, for all other samples at least 4 mg AgCl were available.

DiluSeII, the wheel however also contained the *SM-12* and *SM-13* reference materials, which are used by our collaborators for the calculation of exposure ages. The machine blank in this measurement was $^{36}\text{Cl}/\text{Cl} \approx (1.5 \pm 0.8) \times 10^{-15}$. The uncertainties of the AMS results are in good agreement with the expected reproducibilities shown in figure 6.1.

This measurement demonstrates that ^{36}Cl results from exposure dating samples meet the quality expected from systematic tests. The precision of results is very competitive to other facilities and proves VERA's capability of measuring natural ^{36}Cl samples.

7 A novel technique for sulfur suppression

This chapter gives a detailed account of our investigations concerning techniques for additional isobar suppression and discusses the discovered light-induced suppression of sulfur in a cesium sputter negative ion source.

7.1 Motivation and first experiments

In AMS measurements of ^{36}Cl , element-selective techniques for additional sulfur suppression in the ion source or injector are of great interest. Most obviously, such a technique can significantly increase the abundance sensitivity of small and medium-sized AMS facilities for ^{36}Cl . At VERA, such a method can significantly improve measurements of samples with isotopic ratios $^{36}\text{Cl}/\text{Cl} < 5 \times 10^{-15}$ (as discussed in the previous chapter). However, also large facilities benefit significantly from a reduction of the ^{36}S count rate in the detector, which often limits the measurement current. This is especially true for all facilities where the ion beam is injected directly into the detection setup without a degrader foil in order to achieve high efficiency, e.g. [98, 109, 112]. Furthermore, additional suppression of sulfur by one order of magnitude can also compensate the increased sulfur output caused by smaller sample sizes (cf. section 4.1.3). Hence, such technique can potentially facilitate a reduction of the amount of sample material (AgCl) required for a reliable ^{36}Cl measurement.

We are aware of two promising techniques capable of separating ^{36}Cl and ^{36}S prior to injection into the accelerator: optical filtering via selective photodetachment and resonant charge transfer (cf. section 2.2.3). Each yielded sulfur suppression factors of more than 10^3 in demonstration experiments [43, 45]. In their present form, both methods however require the use of one or more ion coolers to extend the interaction time and avoid collisional neutralization of the wanted ions. These devices introduce significant beam losses and can not be integrated into existing accelerators without substantial changes of the injection system.

Since one order of magnitude in sulfur suppression would be sufficient for our needs, we have tried to implement both techniques directly inside a standard cesium sputter ion source. In a first approach, a modified cathode arrangement of the sputter source was built. It allows gas to be leaked into a cylindrical gas reaction cell (6 mm long and 4 mm diameter) in front of the sputter target. The reaction cell is formed by

a metal cap mounted onto the sample holder. Its interior is dominated by a weak focusing fringe field (~ 30 V from the sample surface to the center of the cell) reaching all the way in from the exit opening. The effect of ~ 0.1 mTorr of NO_2 at the target surface, decreasing through the cell to 10^{-5} mTorr, on the $^{36}\text{S}/^{35}\text{Cl}$ ratio was studied. This was the maximum pressure that allowed operation of the ion source, above, discharges in the source hampered operation. Since NO_2 is a very corrosive gas, the cesium oven was disconnected during this measurement. Still, output currents above $1\text{ }\mu\text{A}$ $^{35}\text{Cl}^-$ current were achieved at ~ 180 W ionizer power. Unfortunately, the $^{36}\text{S}/^{35}\text{Cl}$ ratio from a sample containing AgCl with 1000 ppm Ag_2S was found unaffected (within quite high uncertainties due to random variations) with the gas flow on. Only the total current output decreased by a factor of 5–10, probably due to collisional neutralization on the high density of gas in the source region. Therefore, we didn't further pursue this technique.

The potential of laser photodetachment of sulfur in the ion source was explored by directing a 1 W cw laser beam onto the sample surface. Assuming that the average residence time of ions in the source region is smaller than $10\text{ }\mu\text{s}$, the expected sulfur suppression factors are below 1 %. However, previous experiments with high power pulsed lasers, but different goals in mind, revealed interesting changes in the sulfur and chlorine production [126, 127]. In the course of this experiment we discovered a novel technique for sulfur suppression, which is described in detail in the following sections. The method is based on optical interaction with the environment immediately in front of, or at the surface of the cathode in a cesium sputter negative ion source of the Middleton type [128]. It requires only a free optical path to the target and a high power laser.

7.2 Experimental setup

Experiments were performed at the GUNILLA facility of the University of Gothenburg [129, 130] and at VERA at the University of Vienna using a new injector [52]. In both experiments the same 1.2 W, 445 nm continuous wave diode laser was used. The corresponding photon energy of 2.79 eV lies between the electron affinities of sulfur (2.077 eV) and chlorine (3.613 eV) [131]. Thus, sulfur suppression by photodetachment is energetically possible. At GUNILLA, we also investigated the effect of a 1064 nm (1.17 eV) laser with similar output power. The optical setup was almost identical at both facilities and is shown schematically in figure 7.1. The laser beam entered the ion beamline through a borosilicate window and was directed by a set of four mirrors outside and one mirror inside the vacuum chamber. Two apertures were centered on the laser beam path and positioned about 1 m apart. The mirror placed inside the vacuum chamber was covered by a glass plate with a transparent, conductive layer of ITO ($\text{In}_2\text{O}_3:\text{SnO}_2$). This prevented the glass plate and the mirror from being charged by stray ions that unavoidably hit the mirror. The outside mirror

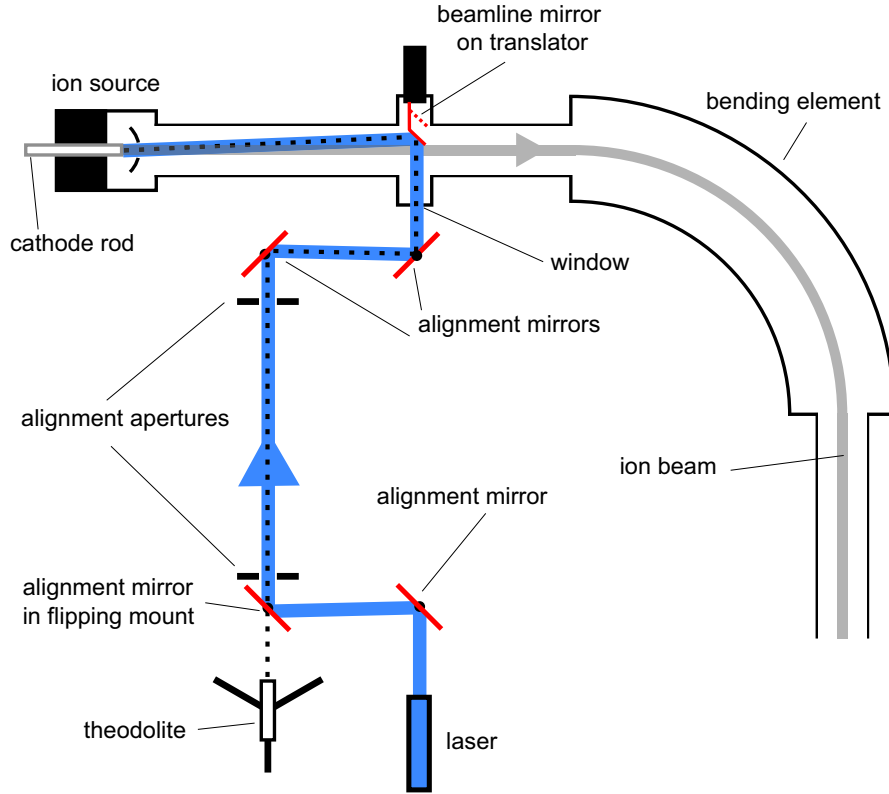


Figure 7.1: Schematic of the optical setup used at GUNILLA and at VERA.

situated in front of the first aperture was mounted in a flipping mirror mount. By flipping this mirror out of the optical path it was possible to optically observe the cathode and the hot ionizer using a theodolite. The system was aligned such that the cathode appeared centered in the two apertures. This ensured that the laser light hit the cathode when the flipping mirror was inserted in the beam path. Fine-tuning of the alignment was achieved by maximizing the effect caused by the laser on either the sulfur or the chlorine signal. The maximum laser power at the cathode position in a $1 \times 1 \text{ mm}^2$ area was approximately 200 mW at GUNILLA and 400 mW at VERA. The highest losses came from absorption in the ITO coated glass plate (about 20 % measured at 445 nm). The optical losses for both wavelengths were about 10 % in the borosilicate window and about 5 % in each mirror.

At GUNILLA the sample material was AgCl containing approximately 10 % Ag_2S (cf. section 4.1.1). Around 500 mg of this material was pressed into a cylindrical cathode with 5 mm inner diameter. At VERA the samples contained 2–20 mg AgCl pressed into a copper cathode with AgBr backing. The area covered with AgCl was 1–3 mm in diameter. Since VERA is an AMS facility, only microscopic amounts of sulfur could be put into the ion source in order to avoid contamination in future measurements. Most samples contained chemically cleaned AgCl with a typical sulfur

content of approximately 1 ppm. At GUNILLA, only one mass can be measured at a time. Hence, the time structure of the effect had to be studied consecutively for various isotopes. At VERA, on the other hand, several masses can be measured almost simultaneously using the offset-Faraday-cups and particle detectors. Here, the switching time between the different detectors allowed for several measurements per second.

7.3 Results with macroscopic amounts of sulfur at GUNILLA

7.3.1 Response of the ion current to laser light

Figure 7.2 shows a comparison of two mass spectra recorded with and without laser. An increase in chlorine current by a factor of 2 and a decrease in oxygen and sulfur currents by more than a factor of 5 were observed when approximately 100 mW of laser light was directed onto the cathode. Furthermore, the light strongly increased the production of Cl_2^- . The ion currents did not change immediately after switching the laser on or off. The time constants for the currents to adjust to a change in laser intensity were of the order of several seconds up to minutes. Since we could not resolve atomic from molecular ions, the mass peaks could possibly contain substantial molecular contributions. This is, however, unlikely since the measured isotopic

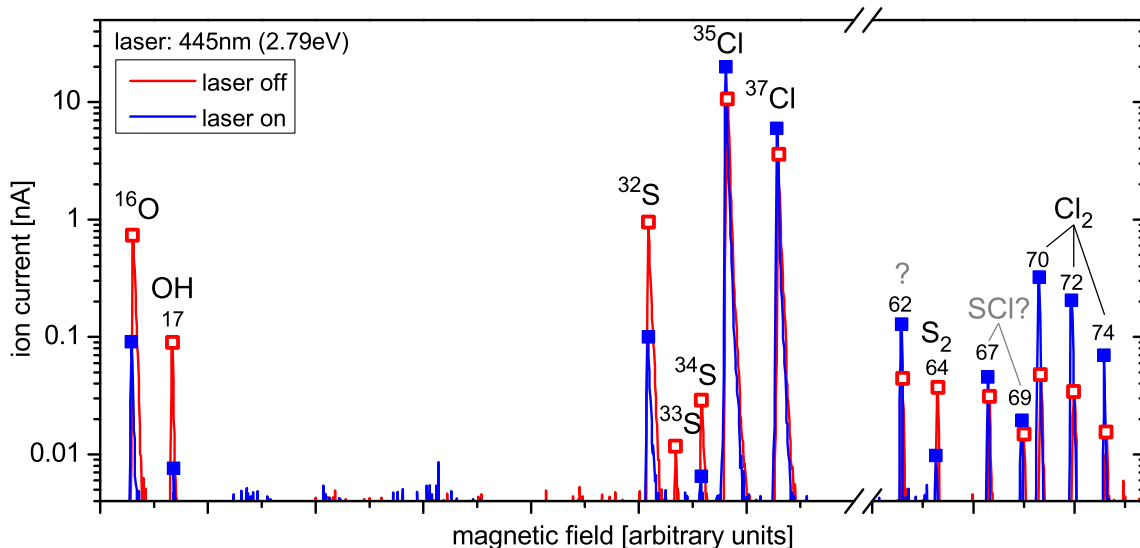


Figure 7.2: Mass spectra obtained at GUNILLA by scanning the analyzing magnet. The figure shows the ion currents without laser light and with 100 mW of laser light with a wavelength of 445 nm (2.79 eV).

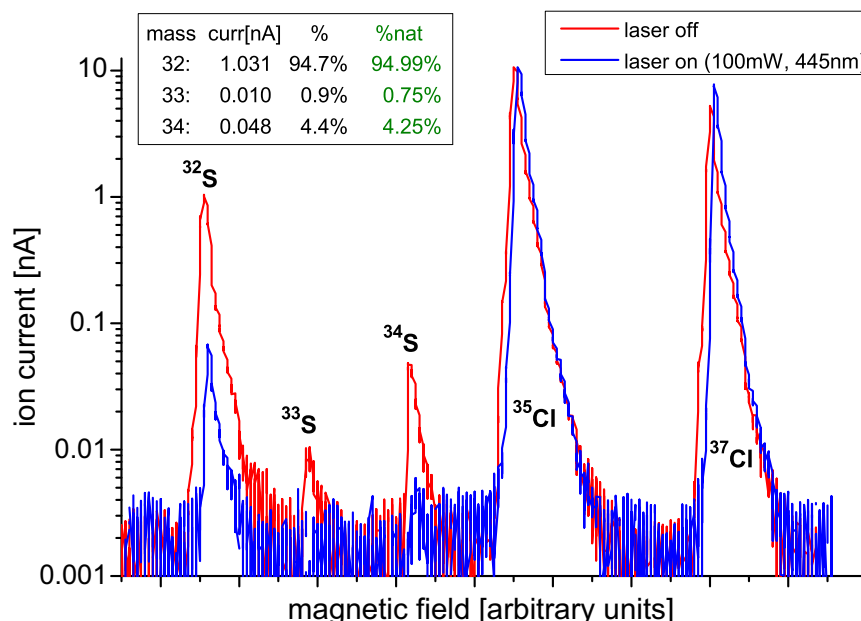


Figure 7.3: Mass spectra of sulfur and chlorine obtained at GUNILLA by scanning the analyzing magnet. The figure shows the ion currents without laser light and with 100 mW of laser light with a wavelength of 445 nm (2.79 eV). The table shows the measured abundances of masses 32, 33 and 34 without laser light and compares them to the natural abundances of sulfur isotopes.

abundances match the natural abundances of sulfur and chlorine isotopes, as shown in figure 7.3. In particular, there was no observed excess at mass 32, indicating only little if any interference from O_2 . After sputtering the sample for more than an hour, the mass scans in both figures were taken minutes apart. The ion source output was stable and the observed change in the ion currents of the elements is an effect of laser light and not an effect of sputter time. The measurements were repeated several times on the same sample giving sulfur suppression factors of 10–20. The ion current for Cl^- shown in figures 7.2 and 7.3 was about 10 nA. However, the transmission of the ion beam apparatus at GUNILLA is only 0.1 % [129]. Thus, the estimated total Cl^- current emitted from the source was of the order of 10 μA , i.e. at the same level as at VERA (cf. section 7.4).

When the operational parameters of the ion source were varied, significant changes in the size of the effect could be observed. While the ionizer power given below may not be best suited to quantify ion source conditions, it is the only parameter directly accessible at the two facilities. The Cs currents could not be measured directly nor inferred from cathode currents. Generally, sulfur suppression worked best with low ionizer power of 70–80 W, producing 5–10 μA Cl^- output. Increasing the Cl^- output to 40 μA with 100–120 W of ionizer power reduced the effect on the sulfur to chlorine ratio to approximately 1.5. Even with constant operating

parameters of the ion source, i.e. ionizer power, output current, cathode current and cesium oven temperature, the magnitude of the effect differed over time without obvious correlation to the sputter age of the cathode. Therefore, we believe that other source parameters, which could not be measured in the current apparatus, played an essential role. This could be, for instance, the cesium vapor pressure, the sample surface temperature or the cesium coverage on the sample. Thus, the observations are hard to disentangle and they cannot be attributed to a particular parameter.

7.3.2 Power and wavelength dependence of the effect

The dependence of the effect on the laser power was also investigated. The results are summarized in figure 7.4. Already as little as 8 mW laser power at the cathode induced a noticeable change in the sulfur output. The data shows a quadratic behavior of the sulfur reduction as a function of the laser power. We also observe a peculiar effect when the laser light is turned off. While the chlorine current quickly drops to its original value, the sulfur current first increases to a value that is substantially larger than the value before the target was illuminated and then returns to its original value on a time scale of a few minutes. This behavior was observed in about one third of the runs. The reason for this effect is still unclear.

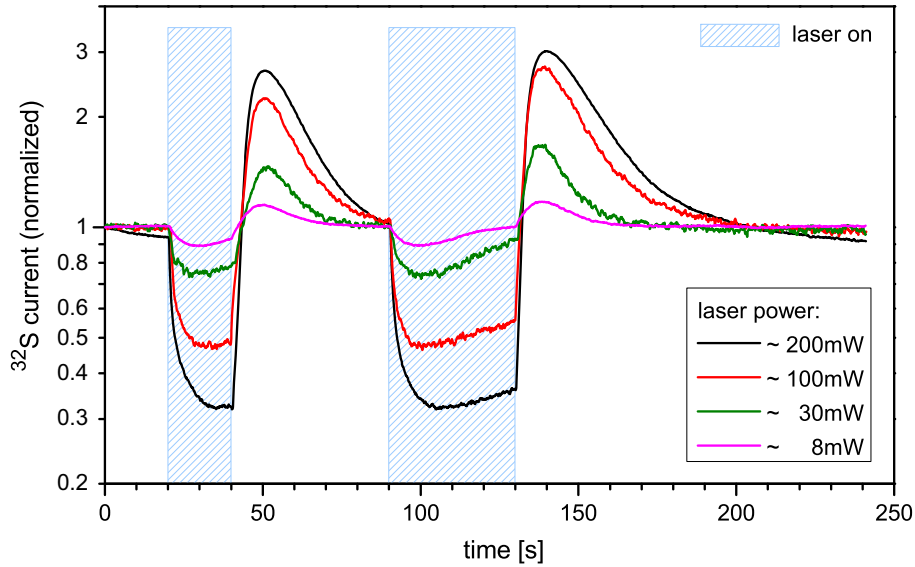


Figure 7.4: Time resolved effect on the $^{32}\text{S}^-$ current for different laser powers. The plotted currents are normalized individually to the initial currents prior to the first laser shot. As little as 8 mW of laser light reduces the sulfur output by 10 %. The high sulfur output after removal of the laser light is not a general feature but was present at various times.

In order to investigate the contribution of photodetachment of sulfur to the effect, the laser source was replaced with a Nd:YAG laser producing radiation with a

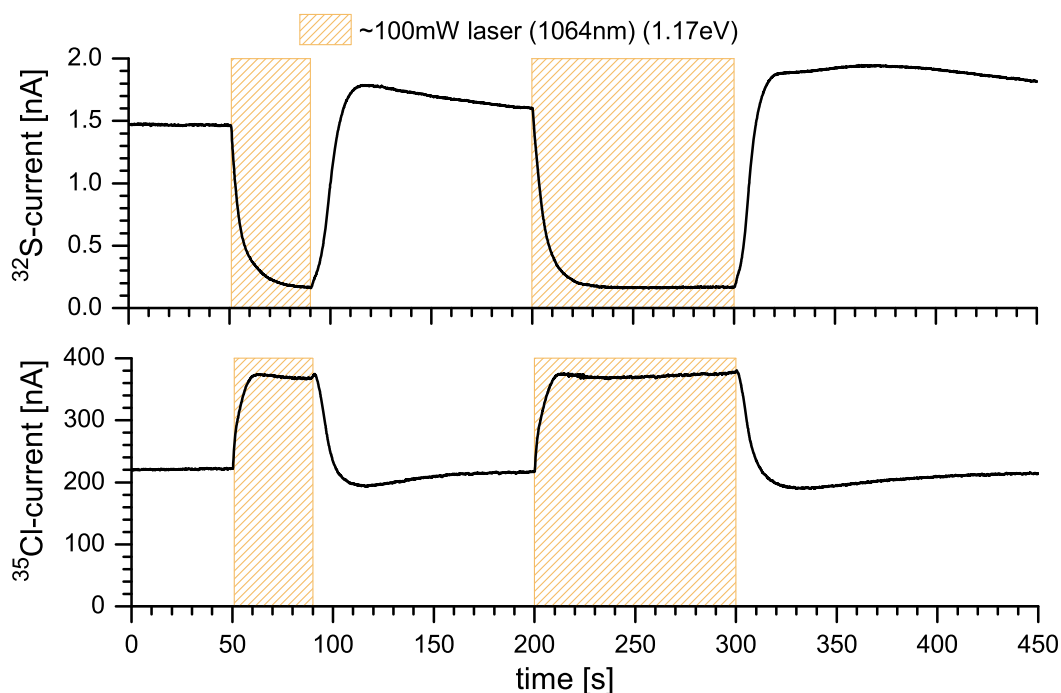


Figure 7.5: Response of the $^{32}\text{S}^-$ and $^{35}\text{Cl}^-$ current to 100 mW IR-laser light. The two scans were obtained one after the other by repeating the experiment.

wavelength of 1064 nm. The corresponding photon energy of 1.17 eV is too small to neutralize any of the ions of interest. The experimental results are shown in figure 7.5. Interestingly, both the $^{35}\text{Cl}^-$ and the $^{32}\text{S}^-$ currents showed the same behavior as with the 445 nm laser. These results rule out photodetachment of S^- as the cause of the reduction of the sulfur beam. No substantial overshoot was seen when the IR-laser was turned off. The time constant for changes in the source output was close to 20 s.

7.4 Results with microscopic amounts of sulfur at VERA

7.4.1 General features of the effect

The general trend of the results from GUNILLA could be reproduced at VERA using typical AgCl-samples for AMS, i.e. with sulfur at ppm levels. The sulfur output from the ion source was monitored via the $^{36}\text{S}^{7+}$ count rate in the split anode ionization chamber (cf. section 3.1.1). Since molecules are efficiently destroyed during the stripping process in the tandem accelerator, events in the detector are unambiguously sulfur ions without any molecular background. Reproducing the effect on sulfur also strengthens the argument that molecular background played a very minor role in

the results obtained at GUNILLA (see above sections). Figure 7.6 shows a typical response of the source output to the laser light. The source delivered 5–12 μA of $^{35}\text{Cl}^-$ current at an ionizer power of 70 W. The response in sulfur had a time constant of several seconds, while the chlorine current took a few minutes to reach equilibrium conditions. This behavior suggests that two different processes are involved. The finding that a low ionizer power favors the investigated laser effect was verified.

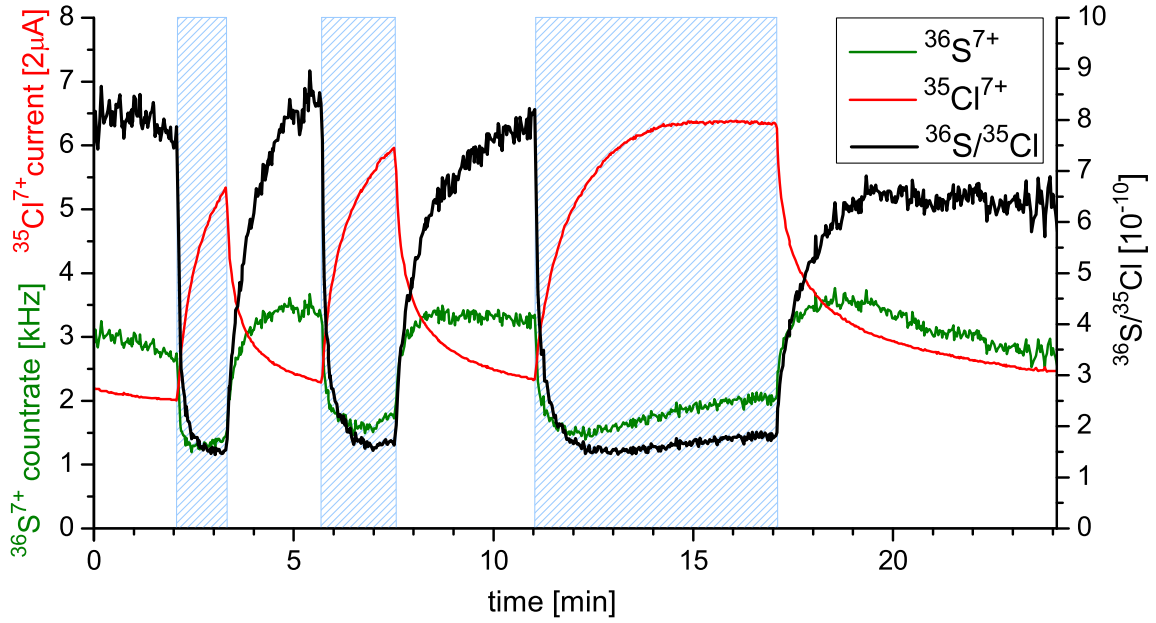


Figure 7.6: Typical response of a 2 mg AgCl target to laser light (445 nm) at VERA. The chlorine (red line) and sulfur output (green line) could be monitored simultaneously and changed in opposite ways by applying the laser light. The $^{36}\text{S}/^{35}\text{Cl}$ ratio (black line) stays constantly low even for a 6 min laser shot.

Even at constant ionizer power the size of the effect varied between different targets. The observed decrease in the sulfur to chlorine ratio ranged from a factor of about 1.3 for all 4 large targets (20 mg AgCl) to a factor of almost 6 for 5 out of 6 small targets (2 mg AgCl). Generally, these changes in sulfur to chlorine ratio were smaller than at GUNILLA, despite a better focusing of the laser beam that yielded 400 mW of laser light in a $1 \times 1 \text{ mm}^2$ area at the target. The explanation could be the less efficient cooling of the cathode via the multi-cathode target wheel compared to the direct cooling of the cathode rod in the single-cathode source used at GUNILLA. It could also be due to different target properties. Apart from initial differences described above, the flat target used at GUNILLA developed a deep sputter crater, whereas no signs of cratering were found on VERA's targets.

7.4.2 Systematic studies

A study of ten identical cathodes was conducted to investigate the reliability of this method for routine AMS measurements. Figure 7.7 shows the sulfur to chlorine ratio as well as the chlorine current for a two-hour period of constant sputtering of the same sample, which was illuminated during time periods ranging from two to ten minutes. Although the lasers used throughout the experiments were cw-lasers, the word shot will be used for these minute-long illumination periods in the following. The high sulfur output when first sputtering the sample arises from surface conditions and is present in almost all AgCl-samples. The sulfur to chlorine ratio then stays

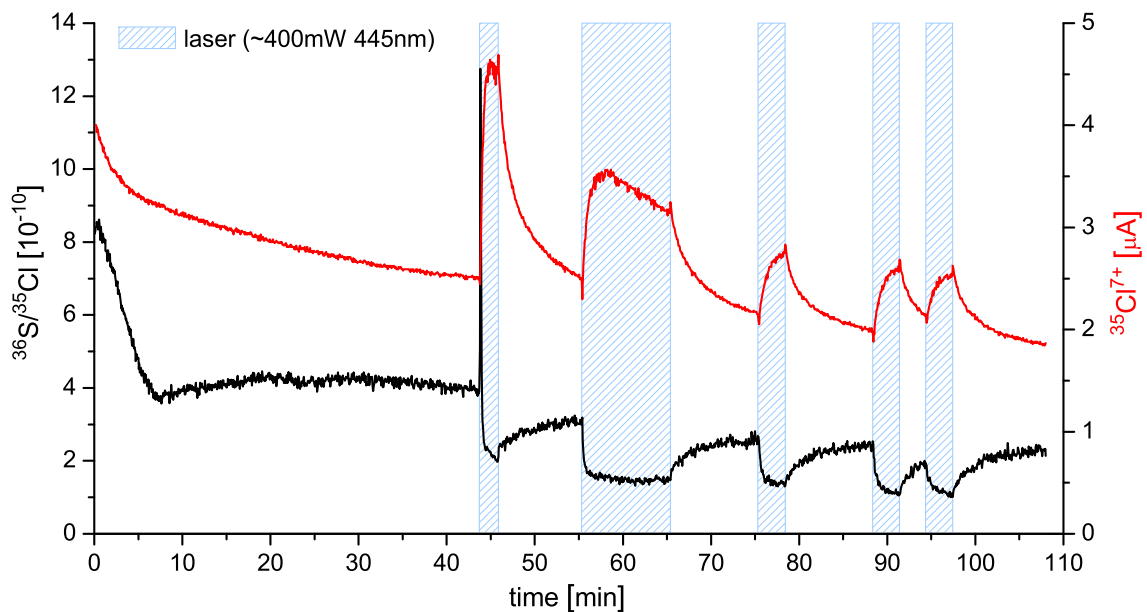


Figure 7.7: $^{36}\text{S}/^{35}\text{Cl}$ ratio (black, left scale) and $^{35}\text{Cl}^{7+}$ -current (red, right scale) over a 2 h-period while turning the laser on and off in periods ranging from a few minutes up to ten minutes (blue areas). Despite prior sputtering for 45 min, the first laser shot seems to have a long-term cleaning effect for sulfur. The response in chlorine output changes with the number of laser shots.

constant for almost an hour until the laser is applied. Interestingly, the typical sulfur reduction is preceded by a several seconds long "cleaning peak" in sulfur output, but only for the first laser illumination. Afterwards no such behavior is observed. When switching off the laser light, the sulfur to chlorine ratio rises again, although in most cases not to its initial value. Such a long-term cleaning effect was only observed for small AgCl-targets with very low sulfur content. Provided that the initial sulfur contamination is sputtered away, the effect of laser light on the isotope currents seems independent of sputter age. Presputtering the sample for an hour did not change the response to laser light. Another effect is that the time constant of the response of the

^{35}Cl -current to the laser light increases with the number of laser shots applied to the cathode from about 20 s in the first shot to about 100 s after 5 shots. The amplitude of the Cl-response also tends to become smaller, typically by 50 % after 5 shots.

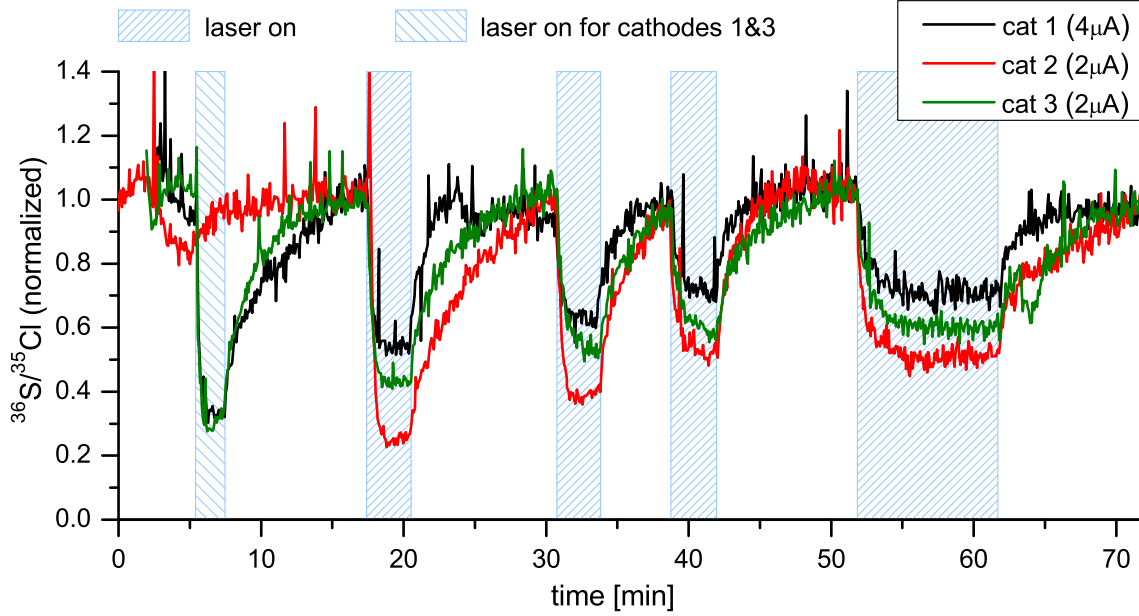


Figure 7.8: Comparison of results from three different samples with the same time sequence of laser illumination (blue areas) except for the first laser shot on cat2. The plotted $^{36}\text{S}/^{35}\text{Cl}$ ratios were normalized to a curve fitted to the $^{36}\text{S}/^{35}\text{Cl}$ values prior to each laser illumination. The effect of the laser light decreases with the number of laser shots applied and can not be enhanced by prolonging the illumination time. Sulfur suppression works best at low total source output, cat1 with a higher source output exhibits a slightly smaller response to laser light. The cathodes were presputtered less than 5 min before data recording started.

Figure 7.8 compares the results of three identical cathodes. It should be noted that another seven cathodes, not shown in the figure, showed similar behaviors. For better comparison of the laser-induced effect, the sulfur to chlorine ratios plotted here have been normalized to a curve fitted to the $^{36}\text{S}/^{35}\text{Cl}$ values prior to each laser shot. Hence, any permanent decrease of sulfur is not visible in figure 7.8. The same illumination sequence was applied to all three cathodes, except for the first laser shot, which was not applied to cathode 2. Comparing the results from this cathode with the others, the magnitude of sulfur to chlorine reduction clearly depends on the number of laser shots already applied or possibly the accumulated illumination time but not on the length of the individual laser shot. The data also shows that the effect is not depending on the sputter age of the cathode before the first illumination. Again, the effect was generally larger at lower source currents.

7.4.3 Application of the laser in an AMS measurement

Finally, the effect on the sulfur to chlorine production ratio induced by laser light has been applied in a regular ^{36}Cl AMS measurement at VERA. The sample was a reference material with a nominal $^{36}\text{Cl}/^{35}\text{Cl}$ ratio of $(1.57 \pm 0.02) \times 10^{-11}$. Measured values are expected to be somewhat lower because of roughly 70 % detector efficiency for ^{36}Cl with the ionization chamber.

Initially, the sample was sputtered for ~ 15 min until the sulfur output reached a stable value. Next, two runs of 7 min each with 30 min of continuous sputtering in between, were performed without laser light. Both yielded the same $^{36}\text{Cl}/^{35}\text{Cl}$ ratio of $(1.14 \pm 0.02) \times 10^{-11}$, and almost equal $^{36}\text{S}/^{35}\text{Cl}$ ratios of $(23.3 \pm 0.05) \times 10^{-11}$ and $(23.9 \pm 0.05) \times 10^{-11}$, respectively. Immediately after the second run the laser was turned on, and after a 2 min wait a run of 7 min was performed with laser light. The $^{36}\text{Cl}/^{35}\text{Cl}$ ratio of $(1.11 \pm 0.02) \times 10^{-11}$ agrees very well to the previous runs. The interfering isobar ^{36}S was reduced by a factor of 2.5 to a $^{36}\text{S}/^{35}\text{Cl}$ ratio of $(8.99 \pm 0.03) \times 10^{-11}$. This substantial reduction of sulfur is clearly visible in the

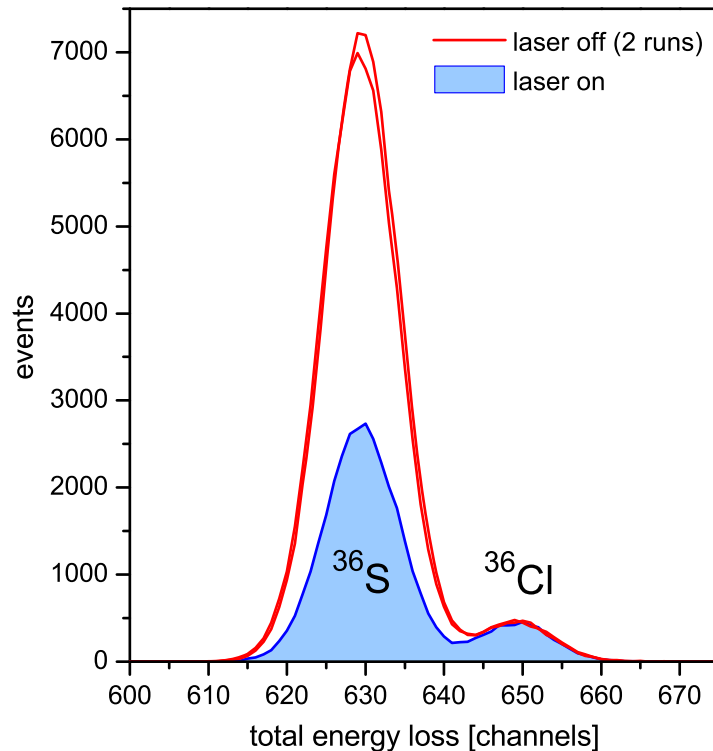


Figure 7.9: Total energy loss spectra from the ionization chamber obtained with and without laser light in an AMS measurement of ^{36}Cl . The laser light reduces the sulfur output from the ion source by a factor of 2.5 but leaves the $^{36}\text{Cl}/^{35}\text{Cl}$ ratio unchanged. Results from each run plotted here are normalized to the same accumulated $^{35}\text{Cl}^{7+}$ charge.

energy loss spectra from the ionization chamber shown in figure 7.9. The $^{35}\text{Cl}/^{37}\text{Cl}$ values remained constant throughout the measurement. Hence, the laser introduces no isotope fractionation but changes only the elemental composition of the negative ion beam.

7.5 Discussion of results and the physics behind the effect

At this point the effect induced by laser light has been studied at two facilities where the influence of several parameters has been investigated. The laser light induced a significant change in oxygen, sulfur and chlorine negative ion production from a AgCl target. However, the physics behind the observed effects remains unclear. The long time constants and the wavelength-independence of the effect are strong evidence that no direct photo-induced process on the respective ions is responsible for the observations. In particular, photodetachment of negative sulfur ions can be ruled out since sulfur suppression also worked with an IR-laser. Bulk heating of the cathode by the laser is also unlikely to cause the effect. Even though the laser power is comparable to the radiation power from the ionizer and to the power transfer of the 3 keV Cs beam, an increase of the target temperature by other means, i.e. reduced cooling or higher ionizer power, does not induce similar changes in the sulfur to chlorine ratio. From our experience gained during the improvement of the ion source regulation, hotter source conditions even favor negative sulfur formation (cf. figure 4.5). One possible cause could be a localized heating effect in the laser focus on the target surface much stronger than the bulk heating. Alternatively, a microplasma might be formed just in front of the sputter area. However, we have no explanation why this should change the sulfur and chlorine output in opposite ways.

Recently, Vogel et al. [132] suggested that post-ionization of sputtered neutrals by excited neutral cesium plays an important role in cesium sputter ion sources of the Middleton type. For sulfur, a significant contribution of post-ionization to the negative ion formation in a cesium rich sputter source has already been postulated by Doucas [133] based on measured energy distributions of negative ions. While charge transfer cross sections for oxygen (and likely also for sulfur due to its similar electronic configuration) with excited neutral cesium are one order of magnitude higher than with ground state neutral cesium [134], the case for chlorine is the opposite [135]. Additionally, charge transfer cross sections for chlorine are generally smaller than for oxygen at eV collision energies. Changing the population of Cs states by laser light may therefore influence the sulfur to chlorine ratio. The presence of excited neutral cesium close to the sample surface in a Middleton-type sputter source was recently confirmed by spectroscopy of the blue light emitted from the source region [136]. Nevertheless it remains to be explained, why the two largely different

photon energies used yielded similar effects. An explanation could be that neutral cesium (both ground state and excited) is reduced by thermal effects induced by the laser. For chlorine, post-ionization might play a minor role compared to the increased output due to local heating of the sample. Also photo-ionization of higher excited states of neutral cesium by both wavelengths can not be excluded, the first excited state can however not be directly ionized with a 1064nm laser. We would like to emphasize that the above discussion is merely an attempt to indicate possible explanations for the observed phenomena. Exploring the physics and disentanglement of observed phenomena requires probing the target surface temperature and diagnosing the cesium conditions, especially the population of various atomic states.

The most important outcome of this study is that the effect induced by laser light can be successfully applied in regular ^{36}Cl AMS measurements. The experiment clearly demonstrates that this method is a viable technique to reduce the interference of ^{36}S in ^{36}Cl detection without introducing losses in the chlorine beam. While an additional sulfur reduction by a factor of 2.5 may not seem impressive, additional improvements in chemical sample preparation require enormous efforts. Furthermore, implementation of the technique requires no major investments and no major changes to existing AMS facilities.

8 Discussion and outlook

The main outcome of this work is that the separation of ^{36}Cl and ^{36}S is feasible at energies of only 24 MeV and competitive ^{36}Cl AMS measurements are now possible at VERA, being a 3 MV tandem accelerator.

From the physics point of view, significant progress was achieved. Detailed investigations of isobar suppression in an ionization chamber led to a better understanding of the physical processes, which determine the separation. Optimal use of the strong energy focussing effect at energies below the maximum of the Bragg curve requires new measurement strategies with ionization chambers (e.g. different configuration of anodes) in order to achieve maximum isobar separation. Additional potential for further optimization of ionization chambers was revealed by our study of the properties of different counting gases. Following advances in detector electronics and design within the last years, the influence of the detector gas is now the major limitation concerning the energy resolution of ionization chambers over a wide energy range. This topic seems to have gone largely unnoticed over the past years and published data on the properties of the gases is very sparse. Therefore we hope that our new insights into the processes, which limit isobar separation, will not only be beneficial for further projects at VERA but also be useful for the measurement of heavier isotopes (e.g. ^{60}Fe) at larger accelerators. Based on all the findings with our detector setup, a dedicated ionization chamber with an additional anode for residual energy measurement and the possibility to insert apertures in between the anodes is currently in preparation. This detector is expected to provide even higher sulfur suppression than the existing setup due to the absence of dead layers (windows) between the differential energy loss measurements and the residual energy measurement. Besides, it will not suffer from radiation damage and simplify the general handling.

In the course of this work, every step of the AMS measurement procedure for ^{36}Cl starting from sample handling to data evaluation was closely examined and optimized. Important advances include the implementation of the ion source regulation, the automation of the tuning procedure and the assessment of memory effect and cross contamination in the ion source.

With the achievements for ^{36}Cl , VERA is now capable of measuring all AMS isotopes, which are currently accessible at facilities with 5–6 MV terminal voltage. This is an important step in the light of the general trend towards cost-efficient, high-precision low-energy AMS systems. At VERA, the excellent sensitivity for ^{36}Cl opens a large field of interesting applications for the near future, a first glimpse is given by the two ^{36}Cl exposure dating projects presented within this thesis.

A highlight is the discovery of a novel method for sulfur suppression in a cesium sputter negative ion source. Continuous wave laser light induces a significant reduction of the sulfur and oxygen negative ion production from a silver-chloride target. At the same time, the formation of Cl^- and Cl_2^- is strongly increased. While no explanation of the observed phenomena has been found so far, the technique was studied at two facilities and finally successfully applied in an AMS measurement at VERA. It provides additional reduction of sulfur in the ion beam that would require substantial efforts by other means, e.g. by improved sample preparation. Furthermore, implementation of the technique requires no major investments and no major changes to existing AMS facilities. Whether this technique potentially provides isobar separation for other isotopes as well has to be investigated. Future exploration of the physics behind the effect will hopefully also shed some light on the process of negative ion formation in a cesium-rich environment.

The implementation of other isobar separation techniques like selective photodetachment of negative ions or resonant charge transfer *directly in the ion source* proved difficult. Their use definitely requires longer interaction times with the ions and thus the use of reaction cells or ion coolers. This is the main aim of a current project funded by the Austrian Science Fund (FWF, grant P 22164-N20).

Bibliography

- [1] A. E. Litherland, Ultrasensitive mass spectrometry with accelerators, *Annual Review of Nuclear and Particle Science* 30 (1980) 437–473.
- [2] D. Elmore, F. M. Phillips, Accelerator mass spectrometry for measurement of long-lived radioisotopes, *Science* 236 (1987) 543–550.
- [3] R. C. Finkel, M. Suter, AMS in the earth-sciences: Technique and applications, *Advances in Analytical Chemistry* 1 (1993) 1–114.
- [4] W. Kutschera, Progress in isotope analysis at ultra-trace level by AMS, *International Journal of Mass Spectrometry* 242 (2005) 145–160.
- [5] H. A. Synal, L. Wacker, AMS measurement technique after 30 years: Possibilities and limitations of low energy systems, *Nuclear Instruments and Methods in Physics Research B* 268 (2010) 701–707.
- [6] P. Steier, R. Golser, V. Liechtenstein, W. Kutschera, A. Priller, C. Vockenhuber, A. Wallner, Opportunities and limits of AMS with 3-MV tandem accelerators, *Nuclear Instruments and Methods in Physics Research B* 240 (2005) 445–451.
- [7] M. Suter, 25 years of AMS - a review of recent developments, *Nuclear Instruments and Methods in Physics Research B* 223-224 (2004) 139–148.
- [8] Laboratoire National Henri Becquerel, Recommended Data, www.nucleide.org/DDEP_WG/DDEPdata.htm, accessed 2011.
- [9] D. Lal, B. Peters, Cosmic Ray Produced Radioactivity on the Earth, in: K. Sitte, S. Flügge (Eds.), *Handbuch der Physik*, vol. 46/2, chap. Kosmische Strahlung, Springer, Berlin, 551–612, 1967.
- [10] S. P. H. T. Freeman, P. Bishop, C. Bryant, G. Cook, A. Fallick, D. Harkness, S. Metcalfe, M. Scott, R. Scott, M. Summerfield, A new environmental sciences AMS laboratory in Scotland, *Nuclear Instruments and Methods in Physics Research B* 223-224 (2004) 31–34.
- [11] M. G. Klein, A. Gottdang, D. J. W. Mous, D. L. Bourlès, M. Arnold, B. Hamelin, G. Aumaître, R. Braucher, S. Merchel, F. Chauvet, Performance

- of the HVE 5 MV AMS System at CEREGE using an absorber foil for isobar suppression, *Nuclear Instruments and Methods in Physics Research B* 266 (2008) 1828–1832.
- [12] M. G. Klein, A. Dewald, A. Gotttdang, S. Heinze, D. J. W. Mous, A new HVE 6 MV AMS system at the University of Cologne, *Nuclear Instruments and Methods in Physics Research B* 269 (2011) 3167–3170.
 - [13] S. Akhmadaliev, R. Heller, D. Hanf, G. Rugel, S. Merchel, The new 6 MV-AMS-facility DREAMS at Dresden, *Nuclear Instruments and Methods in Physics Research B* (2012), doi:10.1016/j.nimb.2012.01.053.
 - [14] J. C. Gosse, F. M. Phillips, Terrestrial in situ cosmogenic nuclides: theory and application, *Quaternary Science Reviews* 20 (2001) 1457–1560.
 - [15] S. Merchel, R. Braucher, L. Benedetti, O. Grauby, D. L. Bourlès, Dating carbonate rocks with in-situ produced cosmogenic ^{10}Be : Why it often fails, *Quaternary Geochronology* 3 (2008) 299–307.
 - [16] S. Merchel, L. Benedetti, D. L. Bourlès, R. Braucher, A. Dewald, T. Faestermann, R. C. Finkel, G. Korschinek, J. Masarik, M. Poutivtsev, P. Rochette, G. Rugel, K. O. Zell, A multi-radionuclide approach for in-situ produced terrestrial cosmogenic nuclides: ^{10}Be , ^{26}Al , ^{36}Cl , and ^{41}Ca from carbonate rocks, *Nuclear Instruments and Methods in Physics Research B* 268 (2010) 1179–1184.
 - [17] J. R. De Laeter, J. K. Böhlke, P. De Bièvre, H. Hidaka, H. S. Peiser, K. J. R. Rosman, P. D. P. Taylor, Atomic weights of the elements review 2000, *Pure Applied Chemistry* 75 (6) (2003) 683–800.
 - [18] X. L. Zhao, A. E. Litherland, J. P. Doupé, W. E. Kieser, The potential for AMS analysis of ^{10}Be using BeF^- , *Nuclear Instruments and Methods in Physics Research B* 223-224 (2004) 199–204.
 - [19] G. M. Raisbeck, F. Yiou, A. Peghaire, J. Guillot, J. Uzereau, Instability of KH_3^- and potential implication for detection of ^{41}Ca with a tandem electrostatic accelerator, in: W. Henning, W. Kutschera, R. Smilher, J. Ynlema (Eds.), *Proceedings of the Symposium on Accelerator Mass Spectrometry*, Argonne National Laboratory Report ANL/PHY-81-1, Argonne, 426–430, 1981.
 - [20] D. Fink, R. Middleton, J. Klein, P. Sharma, ^{41}Ca : measurement by accelerator mass spectrometry and applications, *Nuclear Instruments and Methods in Physics Research B* 47 (1990) 79–96.
 - [21] X. L. Zhao, A. E. Litherland, J. Eliades, W. E. Kieser, Q. Liu, Studies of anions from sputtering I: Survey of MF_n^- , *Nuclear Instruments and Methods in Physics Research B* 268 (2010) 807–811.

- [22] S. A. W. Jacob, M. Suter, H. A. Synal, Ion beam interaction with stripper gas - Key for AMS at sub MeV, *Nuclear Instruments and Methods in Physics Research B* 172 (2000) 235–241.
- [23] L. Kilius, X.-L. Zhao, A. E. Litherland, K. Purser, Molecular fragment problems in heavy element AMS, *Nuclear Instruments and Methods in Physics Research B* 123 (1997) 10–17.
- [24] P. Steier, Exploring the limits of VERA, Ph.D. thesis, University of Vienna, 2000.
- [25] P. Kubik, G. Korschinek, E. Nolte, Accelerator mass spectrometry with completely stripped ^{36}Cl ions at the Munich postaccelerator, *Nuclear Instruments and Methods in Physics Research B* 1 (1984) 51–59.
- [26] P. Collon, T. Antaya, B. Davids, M. Fauerbach, R. Harkewicz, M. Hellstrom, W. Kutschera, D. J. Morrissey, R. C. Pardo, M. Paul, B. M. Sherrill, M. Steiner, Measurement of ^{81}Kr in the atmosphere, *Nuclear Instruments and Methods in Physics Research B* 123 (1997) 122–127.
- [27] R. A. Muller, Radioisotope Dating with a Cyclotron, *Science* 196 (1977) 489–494.
- [28] J. Klein, R. Middleton, H. Tang, Modifications of an FN tandem for quantitative ^{10}Be measurement, *Nuclear Instruments and Methods* 193 (1982) 601–616.
- [29] D. Fink, O. Meirav, M. Paul, H. Ernst, W. Henning, W. Kutschera, R. Kaim, A. Kaufman, M. Magaritz, Accelerator mass spectrometry at the Rehovot Pelletron Tandem: Measurements of abundances of cosmogenic radioisotopes and future prospects, *Nuclear Instruments and Methods in Physics Research B* 5 (1984) 123–128.
- [30] G. M. Raisbeck, F. Yiou, D. Bourles, J. Lestringuez, D. Deboffe, Measurement of ^{10}Be with a tandetron accelerator operating at 2MV, *Nuclear Instruments and Methods in Physics Research B* 5 (1984) 175–178.
- [31] M. Paul, B. G. Glagola, W. Henning, J. G. Keller, W. Kutschera, Z. Liu, K. E. Rehm, B. Schneck, R. H. Siemssen, Heavy ion separation with a gas-filled magnetic spectrograph, *Nuclear Instruments and Methods in Physics Research A* 277 (1989) 418–430.
- [32] V. Alfimov, G. Possnert, A. Aldahan, Measurement of ^{36}Cl with a gas-filled magnet at the Uppsala tandem laboratory, *Nuclear Instruments and Methods in Physics Research B* 259 (2007) 199–203.

- [33] H. J. Hofmann, G. Bonani, E. Morenzoni, M. Nessi, M. Suter, W. Wölfl, Charge state distributions and resulting isotopic fractionation effects of carbon and chlorine in the 1-7 MeV energy range, *Nuclear Instruments and Methods in Physics Research B* 5 (1984) 254–258.
- [34] H. D. Betz, Charge states and charge-changing cross sections of fast heavy ions penetrating through gaseous and solid media, *Reviews of Modern Physics* 44 (3) (1972) 465–539.
- [35] A. M. Müller, M. Christl, J. Lachner, M. Suter, H. A. Synal, Competitive ^{10}Be measurements below 1 MeV with the upgraded ETH-TANDY AMS facility, *Nuclear Instruments and Methods in Physics Research B* 268 (2010) 2801–2807.
- [36] K. Knie, T. Faestermann, G. Korschinek, AMS at the Munich gas-filled analyzing magnet system GAMS, *Nuclear Instruments and Methods in Physics Research B* 123 (1997) 128–131.
- [37] L. G. Gladkis, L. K. Fifield, C. R. Morton, T. T. Barrows, S. G. Tims, Manganese-53: Development of the AMS technique for exposure-age dating applications, *Nuclear Instruments and Methods in Physics Research B* 259 (2007) 236–240.
- [38] K. Hain, T. Faestermann, L. Fimiani, G. Korschinek, P. Ludwig, G. Rugel, ^{93}Zr measurements with Accelerator Mass Spectrometry using a passive absorber, presentation at the DPG Spring Meeting 2012 - Section AMOP, Stuttgart, Germany.
- [39] D. Elmore, B. R. Fulton, M. R. Clover, J. R. Marsden, H. E. Gove, H. Naylor, K. H. Purser, L. R. Kilius, R. P. Beukens, A. E. Litherland, Analysis of ^{36}Cl in environmental water samples using an electrostatic accelerator, *Nature* 277 (1979) 22–25.
- [40] H. A. Synal, J. Beer, G. Bonani, H. J. Hofmann, M. Suter, W. Wölfl, Detection of ^{32}Si and ^{36}Cl with the ETH/SIN EN-tandem, *Nuclear Instruments and Methods in Physics Research B* 29 (1987) 146–150.
- [41] C. Maden, P. A. F. Anastasi, A. Dougans, S. P. H. T. Freeman, R. Kitchen, G. Klody, C. Schnabel, M. Sundquist, K. Vanner, S. Xu, SUERC AMS ion detection, *Nuclear Instruments and Methods in Physics Research B* 259 (2007) 131–139.
- [42] D. Berkovits, E. Boaretto, G. Hollos, W. Kutschera, R. Naaman, M. Paul, Z. Vager, Selective Suppression of Negative Ions by Lasers, *Nuclear Instruments and Methods in Physics Research A* 281 (1989) 663–66.

-
- [43] Y. Liu, C. C. Havener, T. L. Lewis, A. Galindo-Uribarri, J. R. Beene, Efficient Isobar Suppression by Photodetachment in a RF Quadrupole Ion Cooler, AIP Conference Proceedings 1099 (2009) 737–741.
- [44] P. Andersson, A. O. Lindahl, D. Hanstorp, C. C. Havener, Y. Liu, Y. Liu, Nearly complete isobar suppression by photodetachment, Journal of Applied Physics 107 (2010) 026102.
- [45] J. Eliades, A. E. Litherland, W. E. Kieser, L. M. Cousins, S. J. Ye, X. L. Zhao, Cl/S isobar separation using an on-line reaction cell for ^{36}Cl measurement at low energies, Nuclear Instruments and Methods in Physics Research B 268 (2010) 839–842.
- [46] A. E. Litherland, I. Tomschi, X. L. Zhao, L. M. Cousins, J. P. Doupé, G. Javaheery, W. E. Kieser, Isobar separation at very low energy for AMS, Nuclear Instruments and Methods in Physics Research B 259 (2007) 230–235.
- [47] W. E. Kieser, J. Eliades, X. L. Zhao, A. E. Litherland, On-line Ion Chemistry for the AMS Analysis of ^{90}Sr and $^{135,137}\text{Cs}$, presentation at the AMS-12 Conference, Wellington, New Zealand, 2011.
- [48] NEC, Wisconsin, USA, www.pelletron.com.
- [49] W. Kutschera, P. Collon, H. Friedmann, R. Golser, P. Hille, A. Priller, W. Rom, P. Steier, S. Tagesen, A. Wallner, E. M. Wild, G. Winkler, VERA: A new AMS facility in Vienna, Nuclear Instruments and Methods in Physics Research B 123 (1997) 47–50.
- [50] A. Priller, T. Brandl, R. Golser, W. Kutschera, S. Puchegger, W. Rom, P. Steier, C. Vockenhuber, A. Wallner, E. M. Wild, Extension of the measuring capabilities at VERA, Nuclear Instruments and Methods in Physics Research B 172 (2000) 100–106.
- [51] C. Vockenhuber, I. Ahmad, R. Golser, W. Kutschera, V. Liechtenstein, A. Priller, P. Steier, S. Winkler, Accelerator mass spectrometry of heavy long-lived radionuclides, International Journal of Mass Spectrometry 223–224 (2003) 713–732.
- [52] A. Priller, K. Melber, O. Forstner, R. Golser, W. Kutschera, P. Steier, A. Wallner, The new injection beamline at VERA, Nuclear Instruments and Methods in Physics Research B 268 (2010) 824–826.
- [53] P. Steier, R. Golser, W. Kutschera, A. Priller, C. Vockenhuber, S. Winkler, VERA, an AMS facility for "all" isotopes, Nuclear Instruments and Methods in Physics Research B 223–224 (2004) 67–71.

- [54] A. Priller, M. Auer, R. Golser, A. Herschmann, W. Kutschera, J. Lukas, P. Steier, A. Wallner, Ion source refinement at VERA, *Nuclear Instruments and Methods in Physics Research B* 259 (2007) 94–99.
- [55] C. Vockenhuber, R. Golser, W. Kutschera, A. Priller, P. Steier, K. Vorderwinkler, A. Wallner, The Delta-TOF detector for isobar separation at ion energies below 1 MeV/amu, *Nuclear Instruments and Methods in Physics Research B* 240 (2005) 490–494.
- [56] Silson Ltd., www.silson.com.
- [57] M. Stocker, M. Döbeli, M. Grajcar, M. Suter, H. A. Synal, L. Wacker, A universal and competitive compact AMS facility, *Nuclear Instruments and Methods in Physics Research B* 240 (2005) 483–489.
- [58] P. Steier, O. Forstner, R. Golser, W. Kutschera, M. Martschini, S. Merchel, T. Orlowski, A. Priller, C. Vockenhuber, A. Wallner, ^{36}Cl exposure dating with a 3-MV tandem, *Nuclear Instruments and Methods in Physics Research B* 268 (2010) 744–747.
- [59] O. Forstner, P. Andersson, C. Diehl, R. Golser, D. Hanstorp, W. Kutschera, A. O. Lindahl, A. Priller, P. Steier, A. Wallner, Isobar suppression in AMS using laser photodetachment, *Nuclear Instruments and Methods in Physics Research B* 266 (2008) 4565–4568.
- [60] P. Maier-Komor, A. Bergmaier, G. Dollinger, C. M. Frey, H. J. Körner, Improvement of the preparation procedure of carbon stripper foils from the laser plasma ablation-deposition process, *Nuclear Instruments and Methods in Physics Research A* 397 (1997) 131–136.
- [61] T. Orlowski, O. Forstner, R. Golser, W. Kutschera, S. Merchel, M. Martschini, A. Priller, P. Steier, C. Vockenhuber, A. Wallner, Comparison of detector systems for the separation of ^{36}Cl and ^{36}S with a 3-MV tandem, *Nuclear Instruments and Methods in Physics Research B* 268 (2010) 847–850.
- [62] M. Döbeli, C. Kottler, M. Stocker, S. Weinmann, H. A. Synal, M. Grajcar, M. Suter, Gas ionization chambers with silicon nitride windows for the detection and identification of low energy ions, *Nuclear Instruments and Methods in Physics Research B* 219–220 (2004) 415–419.
- [63] O. Forstner, R. Golser, W. Kutschera, L. Michlmayr, A. Priller, P. Steier, A. Wallner, Potential for the application of compact ionization chambers in AMS at energies below 1 MeV/amu, Poster presented by O. Forstner at the International Nuclear Physics Conference 2007.

- [64] O. Forstner, L. Michlmayr, M. Auer, R. Golser, W. Kutschera, A. Priller, P. Steier, A. Wallner, Applications of a compact ionization chamber in AMS at energies below 1 MeV/amu, *Nuclear Instruments and Methods in Physics Research B* 266 (2008) 2213–2216.
- [65] Micron Semiconductor Ltd., www.micronsemiconductor.co.uk.
- [66] mesytec gbr innovative messsysteme, www.mesytec.com.
- [67] J. F. Ziegler, J. P. Biersack, M. D. Ziegler, SRIM, The Stopping and Range of Ions in Matter (version 03), SRIM Co., 2008.
- [68] W. Bragg, R. Kleeman, On the α Particles of Radium, and their Loss of Range in passing through various Atoms and Molecules, *Philosophical Magazine* 10 (1905) 318–340.
- [69] J. F. Ziegler, J. P. Biersack, SRIM - 2008: The Stopping and Range of Ions in Matter program package, <http://www.srim.org/>, accessed 2008.
- [70] H. Bethe, Zur Theorie des Durchgangs schneller Korpuskularstrahlen durch Materie, *Ann. Phys.* 5 (1930) 325–400.
- [71] F. Bloch, Zur Bremsung rasch bewegter Teilchen beim Durchgang durch Materie, *Ann. Phys.* 16 (1933) 285–320.
- [72] R. O. Sayer, Semi-empirical formulas for heavy-ion stripping data, *Revue de physique appliquée* 12 (1977) 1543–1546.
- [73] J. Lindhard, M. Scharff, H. E. Schiott, Range concepts and heavy ion ranges (Notes on atomic collisions, II), *Mat.-Fys. Medd. Dan. Vid. Selsk.* 33 (14) (1963) 1–42.
- [74] N. Bohr, The Penetration of Atomic Particles through Matter, *Mat.-Fys. Medd. Dan. Vid. Selsk.* 18 (8) (1948) 423–568.
- [75] Q. Yang, D. J. O'Connor, Z. Wang, Empirical formulae for energy loss straggling of ions in matter, *Nuclear Instruments and Methods in Physics Research B* 61 (1991) 149–155.
- [76] C. Tschalär, Straggling distributions of extremely large energy losses, *Nuclear Instruments and Methods* 64 (1968) 237–243.
- [77] H. Schmidt-Böcking, H. Hornung, Energy Straggling of Cl Ions in Gases, *Zeitschrift für Physik A* 286 (1978) 253–261.

- [78] G. Schultz, J. Gresser, A study of transport coefficients of electrons in some gases used in proportional and drift chambers, *Nuclear Instruments and Methods* 151 (1978) 413–431.
- [79] H. W. Fulbright, Ionization chambers, *Nuclear Instruments and Methods* 162 (1979) 21–28.
- [80] V. Alfimov, C. Vockenhuber, H. A. Synal, A new 2D sensitive detector setup for ^{36}Cl , *Ion Beam Physics*, ETH Zurich Annual report, 2010.
- [81] H. Timmers, T. R. Ophel, R. G. Elliman, Improved designs of gas ionization detectors used for elastic recoil detection, *Nuclear Instruments and Methods in Physics Research B* 156 (1999) 236–243.
- [82] NIST Chemistry Webbook, www.nist.gov, accessed 2011.
- [83] IRCU, Average Energy Required to Produce an Ion Pair, Report No. 31, International Commission on Radiation Units and Measurements, Washington, D.C., 1979.
- [84] T. D. M. Weijers, T. R. Ophel, H. Timmers, R. G. Elliman, A systematic study of the pulse height deficit in propane-filled gas ionization detectors, *Nuclear Instruments and Methods in Physics Research A* 483 (2002) 676–688.
- [85] T. D. M. Weijers-Dall, H. Timmers, R. G. Elliman, Origins of the residual pulse height deficit in propane-filled gas ionization detectors, *Nuclear Instruments and Methods in Physics Research A* 550 (2005) 139–144.
- [86] A. M. Müller, Entwicklung von universellen AMS-Anlagen bei tiefen Energien (Diss. ETH Nr. 18393), Ph.D. thesis, ETH Zurich, 2009.
- [87] G. Sun, M. Döbeli, A. M. Müller, M. Stocker, M. Suter, L. Wacker, Energy loss and straggling of heavy ions in silicon nitride in the low MeV energy range, *Nuclear Instruments and Methods in Physics Research B* 256 (2007) 586–590.
- [88] C. Vockenhuber, V. Alfimov, M. Döbeli, M. Suter, H. A. Synal, M. Martschini, P. Steier, Energy loss straggling measurements - Determination of a critical parameter for the ^{36}Cl - ^{36}S isobar separation, *Ion Beam Physics*, ETH Zurich Annual report, 2009, 32.
- [89] CREMAT, Inc., www.cremat.com.
- [90] M. Grajcar, M. Döbeli, P. Kubik, H. A. Synal, L. Wacker, M. Suter, New concepts of ^{10}Be AMS at low energies, *Nuclear Instruments and Methods in Physics Research B* 259 (2007) 173–177.

-
- [91] O. Bunemann, T. E. Cranshaw, J. A. Harvey, Design of Grid Ionization Chambers, *Canadian Journal of Research* 27A (1949) 191–206.
- [92] U. Fano, Ionization Yield of Radiations. II. The Fluctuations of the Number of Ions, *Physical Review* 72 (1) (1947) 26–29.
- [93] D. Srdoc, B. Obelic, I. K. Bronic, Statistical fluctuations in the ionisation yield for low-energy photons absorbed in polyatomic gases, *Journal of Physics B: Atomic and Molecular Physics* 20 (1987) 4473–4484.
- [94] A. Pansky, A. Breskin, R. Chechik, Fano factor and the mean energy per ion pair in counting gases, at low x-ray energies, *Journal of Applied Physics* 82 (2) (1997) 871–877.
- [95] M. Stocker, AMS bei tiefen Energien (Diss. ETH Nr. 16787), Ph.D. thesis, ETH Zurich, 2006.
- [96] M. Suter, M. Döbeli, M. Grajcar, A. M. Müller, M. Stocker, G. Sun, H. A. Synal, L. Wacker, Advances in particle identification in AMS at low energies, *Nuclear Instruments and Methods in Physics Research B* 259 (2007) 165–172.
- [97] T. Doke, N. Ishida, M. Kase, Fano factors in rare gases and their mixtures, *Nuclear Instruments and Methods in Physics Research B* 63 (1992) 373–376.
- [98] K. M. Wilcken, S. P. H. T. Freeman, A. Dougans, S. Xu, R. Loger, C. Schnabel, Improved ^{36}Cl AMS at 5 MV, *Nuclear Instruments and Methods in Physics Research B* 268 (2010) 748–751.
- [99] S. Merchel, W. Bremser, V. Alfimov, M. Arnold, G. Aumaître, L. Benedetti, D. L. Bourlès, M. Caffee, L. K. Fifield, R. C. Finkel, S. P. H. T. Freeman, M. Martschini, Y. Matsushi, D. H. Rood, K. Sasa, P. Steier, T. Takahashi, M. Tamari, S. G. Tims, Y. Tosaki, K. M. Wilcken, S. Xu, Ultra-trace analysis of ^{36}Cl by accelerator mass spectrometry: an interlaboratory study, *Analytical and Bioanalytical Chemistry* 400 (2011) 3125–3132.
- [100] L. C. Northcliffe, R. F. Schilling, Range and Stopping-Power Tables for Heavy Ions, *Nuclear Data Tables A7* (1970) 233–463.
- [101] L. Michlmayr, Isobar separation with poststripping for the measurement of cosmogenic ^{10}Be , Master’s thesis, University of Vienna, 2007.
- [102] ORTEC®, www.ortec-online.com.
- [103] N. J. Conard, D. Elmore, P. W. Kubik, H. E. Gove, L. E. Tabbs, B. A. Chrunk, M. Wahlen, The chemical preparation of AgCl for measuring ^{36}Cl in polar ice with accelerator mass spectrometry, *Radiocarbon* 28-2A (1986) 556–560.

- [104] J. O. Stone, G. Allan, L. K. Fifield, R. G. Cresswell, Cosmogenic chlorine-36 from calcium spallation, *Geochimica et Cosmochimica Acta* 60 (1996) 679–692.
- [105] Alfa Aesar, www.alfa.com.
- [106] Merck Chemicals, www.merck-chemicals.com.
- [107] Eppendorf, www.eppendorf.com.
- [108] Sigma-Aldrich, www.sigmaaldrich.com.
- [109] H. A. Synal, J. Beer, G. Bonani, C. Lukaszczuk, M. Suter, ^{36}Cl measurements at the Zürich AMS facility, *Nuclear Instruments and Methods in Physics Research B* 92 (1994) 79–84.
- [110] G. A. Norton, R. L. Loger, J. E. Raatz, R. D. Rathmell, Multi-cathode SNICS ion source, in: J. Benson, L. Rowton, J. Tesmer, R. Darling (Eds.), *Proceedings of the 25th Symposium of North Eastern Accelerator Personnel (SNEAP) 1991*, Singapore: World Scientific, 295–298, 1992.
- [111] D. C. Weisser, N. R. Lobanov, P. A. Hausladen, L. K. Fifield, H. J. Wallace, S. G. Tims, E. G. Apushkinsky, Novel matching lens and spherical ionizer for a cesium sputter ion source, *Pramana - Journal of Physics* 59 (6) (2002) 997–1006.
- [112] L. K. Fifield, S. G. Tims, T. Fujioka, W. T. Hoo, S. E. Everett, Accelerator mass spectrometry with the 14UD accelerator at the Australian National University, *Nuclear Instruments and Methods in Physics Research B* 268 (2010) 858–862.
- [113] D. Elmore, X. Ma, T. Miller, K. Mueller, M. Perry, F. Rickey, P. Sharma, P. Simms, M. Lipschutz, S. Vogt, Status and plans for the PRIME Lab AMS facility, *Nuclear Instruments and Methods in Physics Research B* 123 (1997) 69–72.
- [114] S. Ivy-Ochs, H. A. Synal, C. Roth, M. Schaller, Initial results from isotope dilution for Cl and ^{36}Cl measurements at the PSI/ETH Zurich AMS facility, *Nuclear Instruments and Methods in Physics Research B* 223-224 (2004) 623–627.
- [115] D. Desilets, M. Zreda, P. F. Almasi, D. Elmore, Determination of cosmogenic ^{36}Cl in rocks by isotope dilution: innovations, validation and error propagation, *Chemical Geology* 233 (2006) 185–195.
- [116] V. Alfimov, H. A. Synal, R. C. Finkel, K. M. Wilcken, Re-Calibration of ETH chlorine-36 standards, *Ion Beam Physics, ETH Zurich Annual report*, 2009.

-
- [117] S. Pavetich, AMS measurement of the reaction $^{35}\text{Cl}(n,\gamma)^{36}\text{Cl}$ and its relevance to astrophysics and nuclear technology, Master's thesis, University of Vienna, 2011.
- [118] S. Töszér, Full-scale reconstruction and upgrade of the Budapest Research Reactor, in: Research reactor modernization and refurbishment (IAEA-Tecdoc-1625), IAEA, 83–94, 2009.
- [119] M. Arnold, S. Merchel, D. L. Bourlès, R. Braucher, L. Benedetti, R. C. Finkel, G. Aumaître, A. Gottdang, M. G. Klein, The French accelerator mass spectrometry facility ASTER: Improved performance and developments, Nuclear Instruments and Methods in Physics Research B 268 (2010) 1954–1959.
- [120] M. L. Roberts, G. S. Bench, T. A. Brown, M. Caffee, R. C. Finkel, S. P. H. T. Freeman, L. J. Hainsworth, M. Kashgarian, J. E. McAninch, I. D. Proctor, J. R. Southon, J. S. Vogel, The LLNL AMS facility, Nuclear Instruments and Methods in Physics Research B 123 (1997) 57–61.
- [121] Center for Accelerator Mass Spectrometry (CAMS), LLNL, <https://cams.llnl.gov/about.php>, accessed 2012.
- [122] D. Sengupta, N. Bhandari, S. Watanabe, Formation age of Lonar Meteor Crater, India, Revista de Fisica Aplicada e Instrumentacao 12 (1997) 1–7.
- [123] D. Storzer, C. Koeberl, Age of the Lonar Impact Crater, India: First results from fission track dating (abstract #1309), 35th Lunar and Planetary Science Conference, Houston, Texas, 2004.
- [124] F. Jourdan, F. Moynier, C. Koeberl, S. Eroglu, $^{40}\text{Ar}/^{39}\text{Ar}$ age of the Lonar crater and consequence for the geochronology of planetary impacts, Geology 39 (2011) 671–674.
- [125] C. Yildirim, T. Schildgen, H. Echtler, D. Melnick, B. Bookhagen, A. Ciner, S. Niedermann, S. Merchel, M. Martschini, P. Steier, M. Strecker, Tectonic and climatic implications of fluvial incision at the northern margin of the Central Anatolian Plateau from multiple cosmogenic nuclides, manuscript in preparation.
- [126] D. Berkovits, E. Boaretto, G. Hollos, W. Kutschera, R. Naaman, M. Paul, Z. Vager, Observation of high intensity negative ion pulses by laser impact, Nuclear Instruments and Methods in Physics Research A 302 (1991) 379–381.
- [127] G. Korschinek, T. Henkelmann, Negative ions generated by laser-material interaction (invited), Review of Scientific Instruments 63(4) (1992) 2672–2675.

- [128] R. Middleton, A versatile high intensity negative ion source, *Nuclear Instruments and Methods* 214 (1983) 139–150.
- [129] C. Diehl, K. Wendt, A. O. Lindahl, P. Andersson, D. Hanstorp, Ion optical design of a collinear laser-negative ion beam apparatus, *Review of Scientific Instruments* 82 (2011) 053302.
- [130] D. Hanstorp, An ion beam apparatus for collinear photodetachment experiments, *Nuclear Instruments and Methods in Physics Research B* 100 (1995) 165–175.
- [131] T. Andersen, H. K. Haugen, H. Hotop, Binding Energies in Atomic Negative Ions: III, *Journal of Physical and Chemical Reference Data* 28(6) (1999) 1511–1533.
- [132] J. S. Vogel, J. A. Giacomo, S. R. Dueker, Rethinking ionization in the high intensity cesium sputter negative ion source, submitted to *Nuclear Instruments and Methods in Physics Research B*.
- [133] G. Doucas, Energy distribution of negative ions sputtered from caesiated surfaces, *International Journal of Mass Spectrometry and Ion Physics* 25 (1977) 71–87.
- [134] R. B. Vora, J. E. Turner, R. N. Compton, Single-electron excitation and transfer in collisions of alkali-metal and oxygen atoms, *Physical Review A* 9 (6) (1974) 2532–2544.
- [135] D. Arora, J. E. Turner, P. G. Khubchandani, Alkali-metal - halogen charge-exchange collisions, *Physical Review A* 14 (6) (1976) 2089–2094.
- [136] P. Andersson, M. Martschini, A. Priller, P. Steier, R. Golser, O. Forstner, Spectroscopic analysis of the blue light emitted from Middleton type Cesium sputter negative ion sources, submitted to *Review of Scientific Instruments*.

Acknowledgments

First of all, I want to thank Prof. Robin Golser for giving me the opportunity to do my PhD-thesis at VERA and his support during all stages of this work. I was in the lucky position to have Martin Suter as a "co-supervisor" and I am very grateful to him for his scientific input and guidance, for many interesting discussions and for proofreading parts of this thesis.

I feel indebted to Stefan Pavetich and Pontus Andersson, who joined forces with me during much of the experimental work, and to Oliver Forstner, who provided a lot of support including funding in the framework of his FWF-project. Furthermore, I want to express my thanks to the whole VERA staff, especially Alfred Priller and Peter Steier for technical and software-related assistance, Helga Vincro for guiding me through the jungle of bureaucracy and Ewald Friedl, Johann Lukas, Wolfgang Hieß and Gabi Obstmayer from the electronics and mechanics workshop who did a great job when some device was urgently needed - which is always the case in science. In addition I want to thank ...

... Silke Merchel from the Helmholtz-Zentrum Dresden-Rossendorf for fruitful discussion on the memory effect of the ion source and sharing her knowledge in Cl-chemistry.

... Dag Hanstorp, Anton Lindahl and Johan Rohlén from the University of Gothenburg for their hospitality and their support in the laser experiments and for lending us the blue laser.

... the AMS-group at the ETH/PSI, Zürich, Switzerland and the GAMS group at the TU Munich for providing ^{36}Cl standard material.

... the Austrian Science Fund (FWF) for providing financial support through grant P 22164-N20.

... the University of Vienna for supporting this work by a "Forschungsstipendium 2010 der Universität Wien".

... my colleagues Claudia, Daniel, Edith, Fabienne, Franz, Franz, Jakob, Jenny, Josef, Karin, Karl, Kathi, Kerstin, Klaus, Lea, Leonard, Peter, Philipp, Stefan and Thomas for the nice atmosphere in the office and at the institute.

... Barbara, Claudia, David, Fabienne, Georg, Jenny, Kerstin, Philipp, Silvia and Stefan for the entertaining "Physikerabende" and for the lively discussions at lunch.

Abschließend möchte ich meinen Eltern dafür danken, dass sie mich während meines gesamten Studiums wohlwollend unterstützt haben. Der größte Dank gebührt meiner Verlobten Viktoria, die immer für mich da war, und meiner Tochter Amelie, die mir sowohl meinen Schlaf gönnte als auch die zeitweilige Mühsal einer solchen Arbeit mit einem Lachen vergessen machen kann.

Curriculum vitae of Martin Martschini

Present Affiliation:

VERA Laboratory
University of Vienna - Faculty of Physics
Währingerstrasse 17, 1090 Vienna, Austria

Permanent Address:

Radetzkystrasse 13
2500 Baden
Austria

Personal

Date of birth: 31st March 1983
Place of birth: Baden, Austria
Nationality: Austria
Email: martin.martschini@univie.ac.at

Education

1989–1993: Elementary school in Baden, Austria
1993–2001: High school, BG&BRG Baden Biondegasse, Baden, Austria
May 2001: Graduation (*Matura with distinction*)
2001–2002: Mandatory military service, Großmittel, Lower Austria
2002–2008: Diploma study in Physics, University of Vienna
2007–2008: Master thesis at the VERA Laboratory, Faculty of Physics,
University of Vienna (supervisor: Prof. Walter Kutschera):
 *$^{10}\text{Be} - ^{10}\text{B}$ - isobar separation with a degrader foil: Implementation
and testing of an optimized ion-optical setup for AMS of ^{10}Be*
June 2008: Master degree in Physics (Mag. rer. nat.) *with distinction*
since 2008: Doctoral study in Physics, University of Vienna

Working Experience

since 2010: Teaching Assistant at the University of Vienna (*Nuclear Physics*)

Scholarships

- 2002 – 2007: 4 Academic Excellence Scholarships (Leistungsstipendien)
of the University of Vienna
- 2010: Forschungsstipendium 2010 der Universität Wien

Publications

2010

P. Steier, O. Forstner, R. Golser, W. Kutschera, M. Martschini, S. Merchel, T. Orlowski, A. Priller, C. Vockenhuber, A. Wallner, *^{36}Cl exposure dating with a 3-MV tandem*, Nuclear Instruments and Methods in Physics Research B 268 (2010) 744–747.

T. Orlowski, O. Forstner, R. Golser, W. Kutschera, S. Merchel, M. Martschini, A. Priller, P. Steier, C. Vockenhuber, A. Wallner, *Comparison of detector systems for the separation of ^{36}Cl and ^{36}S with a 3-MV tandem*, Nuclear Instruments and Methods in Physics Research B 268 (2010) 847–850.

2011

M. Martschini, O. Forstner, R. Golser, W. Kutschera, S. Pavetich, A. Priller, P. Steier, M. Suter, A. Wallner, *Recent advances in AMS of ^{36}Cl with a 3-MV-tandem*, Nuclear Instruments and Methods in Physics Research B 269 (2011) 3188–3191.

O. Forstner, H. Gnaser, R. Golser, D. Hanstorp, M. Martschini, A. Priller, J. Rohlén, P. Steier, C. Vockenhuber, A. Wallner, *Reassessment of ^{182}Hf AMS measurements at VERA*, Nuclear Instruments and Methods in Physics Research B 269 (2011) 3180–3182.

S. Merchel, W. Bremser, V. Alfimov, M. Arnold, G. Aumaître, L. Benedetti, D. L. Bourlès, M. Caffee, L. K. Fifield, R. C. Finkel, S. P. H. T. Freeman, M. Martschini, Y. Matsushi, D. H. Rood, K. Sasa, P. Steier, T. Takahashi, M. Tamari, S. G. Tims, Y. Tosaki, K. M. Wilcken, S. Xu, *Ultra-trace analysis of ^{36}Cl by accelerator mass spectrometry: an interlaboratory study*, Analytical and Bioanalytical Chemistry 400 (2011) 3125–3132.

2012

M. Martschini, P. Andersson, O. Forstner, R. Golser, D. Hanstorp, A.O. Lindahl, W. Kutschera, S. Pavetich, A. Priller, J. Rohlén, P. Steier, M. Suter, A. Wallner, *AMS of ^{36}Cl with the VERA 3 MV tandem accelerator*, Nuclear Instruments and Methods in Physics Research B (2012), doi:10.1016/j.nimb.2012.01.055.

M. Martschini, J. Rohlén, P. Andersson, R. Golser, D. Hanstorp, A.O. Lindahl, A. Priller, P. Steier, O. Forstner, *Light-induced suppression of sulfur in a cesium sputter ion source*, International Journal of Mass Spectrometry (2012), doi:10.1016/j.ijms.2012.02.023.

Invited talks

ETH-Zürich, Zurich, Switzerland, 23 Feb. 2011: *AMS of ^{36}Cl with the VERA 3-MV-tandem accelerator*.

Conference contributions

Joint Annual ÖPG-SPG-ÖGAA Meeting, 6–10 Sept. 2009, Innsbruck, Austria:
 ^{36}Cl exposure dating with a 3-MV AMS facility, presented as talk.
An optimized ion-optical setup for AMS of ^{10}Be with a degrader foil, presented as poster.

DPG Spring Meeting, 8–12 March 2010, Hannover, Germany:
Recent advances in AMS of ^{36}Cl with a 3-MV-tandem, presented as talk.
An optimized ion-optical setup for AMS of ^{10}Be with a degrader foil, presented as poster.

Annual ÖPG Meeting, 6–9 Sept. 2010, Salzburg, Austria:
Recent advances in AMS of ^{36}Cl with a 3-MV-tandem, presented as talk.

10th European Conference on Accelerators in Applied Research and Technology (ECAART 10), 13–17 Sept. 2010, Athens, Greece:
Recent advances in AMS of ^{36}Cl with a 3-MV-tandem, presented as poster.

12th International Conference on Accelerator Mass Spectrometry (AMS-12), 20–25 March 2011, Wellington, New Zealand:
AMS of ^{36}Cl with the VERA 3-MV-tandem accelerator, presented as talk.

DPG Spring Meeting, 12–16 March 2012, Stuttgart, Germany:
Investigations of the sputtering process in Middleton-type ion sources, presented as talk.